UC Santa Barbara
UC Santa Barbara Electronic Theses and Dissertations

Title

An improved particle-based method with applications to multiscale biophysical problems

Permalink

Author

Pereira Jacob, Bruno Tadeu

Publication Date

2021

Peer reviewed|Thesis/dissertation

University of California
Santa Barbara

An improved particle-based method with applications to multiscale biophysical problems

A dissertation submitted in partial satisfaction
of the requirements for the degree

Doctor of Philosophy
in
Mechanical Engineering

by

Bruno Tadeu Pereira Jacob

Committee in charge:

Professor Linda Petzold, Chair
Professor John Gilbert
Professor Jeff Moehlis
Professor Ted Bennett

September 2021

The Dissertation of Bruno Tadeu Pereira Jacob is approved.

_____

Professor John Gilbert

_____

Professor Jeff Moehlis

_____

Professor Ted Bennett

_____

Professor Linda Petzold, Committee Chair

August 2021

An improved particle-based method with applications to multiscale biophysical
problems

Copyright © 2021

by

Bruno Tadeu Pereira Jacob

To my mom, Adriana Dias Pereira Jacob, and my wife, Adra Bowman, for all the love
and support, and to my advisor, Prof. Linda Petzold, for the mentorship, help and
inspiration.

Acknowledgements

I would like to thank my mother, Adriana Dias Pereira Jacob, my wife Adra Bowman, and my family (Doug, Kara, Tory and Janna Bowman and Lupita Montero) for all the love and support during these past years. I'm also incredibly grateful for my good friend, Raphael Egan, for all the coffees, talks and scientific debates. Finally, I would like to thank my advisor, Prof. Linda Petzold, for all the support, intellectual freedom and for giving me a chance.

Curriculum Vitæ
Bruno Tadeu Pereira Jacob

Education

2021	Ph.D. in Mechanical Engineering, Emphasis in Computational Science and Engineering (Expected), University of California, Santa Barbara.
2015	M.Sc. in Mechanical Engineering, Federal University of Uberlandia, Brazil
2014	B.Sc. in Mechanical Engineering, Federal University of Uberlandia, Brazil

Publications

Jacob, B., Drawert, B., Li, Z., Yi, T.M. and Petzold, L., 2019. *A hybrid smoothed dissipative particle dynamics (SDPD) spatial stochastic simulation algorithm (sSSA) for advection–diffusion–reaction problems*. Journal of Computational Physics, 378, pp.1-17.

Jacob, B., Drawert, B., Li, Z., Yi, T.M. and Petzold, L., 2019. *Validation data for a hybrid smoothed dissipative particle dynamics (SDPD) spatial stochastic simulation algorithm (sSSA) method*. Data In Brief, 22, pp.11-15.

Jacob, B., Duarte, L.E.R., Andrade, J.R. and Duarte, C.A.R., 2020. *Effects of random disturbances on the stability of a temporally evolving incompressible plane wake*. Mechanics Research Communications, 103, p.103475.

Jacob, B., Jiang, R., Geiger, M., Matthew, S., Rumsey, B., Singh, P., Wrede, F., Yi, T.M., Drawert, B., Hellander, A. and Petzold, L., 2021. *Epidemiological modeling in StochSS Live!*. Bioinformatics.

Jacob, B., Drawert, B., Yi, T. M. and Petzold, L., 2021. *An arbitrary Lagrangian Eulerian smoothed particle hydrodynamics (ALE-SPH) method with a boundary volume fraction formulation for fluid-structure interaction*. Engineering Analysis with Boundary Elements, 128, pp.274-289

Abstract

An improved particle-based method with applications to multiscale biophysical problems

by

Bruno Tadeu Pereira Jacob

An improved particle-based method for continuum mechanics with both stochastic and deterministic reaction-diffusion of chemical species in moving boundaries is presented. The method enables the simulation of a class of biophysical problems that could not be resolved by using classical mesh-based approaches.

This dissertation is divided in three parts: in Chapter 1, we present an introduction of particle-based methods, with an overview of its advantages and limitations, along with recent improvements and applications. In Chapters 2 and 3, we propose solutions to two crucial factors that limit the applicability of particle-based methods to biophysical problems, respectively: (a) the lack of a discrete spatial stochastic formulation for reaction-diffusion systems, and (b) the onset of numerical instabilities that cause particles to penetrate moving wall boundaries. In Chapter 4, we summarize our results and conclude that the usage of our method provide a robust particle-based multiphysics framework that extends the reach of particle-based methods to new types of problems including those of biological relevance.

Contents

Chapter 1

Introduction

1.1 Particle-based methods

There are two broad types of widely used numerical methods used in the simulation of continuum mechanics problems: *mesh-based* and *particle-based* methods. Traditional mesh-based methods, such as finite element (FEM), finite difference (FDM), and finite volume (FVM), typically implement a mesh to cover the volume domain representing the cell. However, in problems involving moving boundaries and large domain deformations, these mesh methods can become inaccurate [1] and often computationally expensive. Particle-based methods have become popular as an alternative to overcome these problems. In these methods, instead of mesh nodes, the system is represented by arbitrarily distributed particles that represent its state. Depending on the method formulation, these particles are often allowed to move in space, hence offering a natural alternative to track moving boundaries and other dynamic-shaped problems.

1.1.1   Smoothed Particle Hydrodynamics (SPH)

Considered the first particle-based method developed, Smoothed Particle Hydrodynamics (SPH) was proposed independently by [2] and [3] as a method to simulate astrophysical problems. Since its development, SPH has been used in a wide range of applications, including colloidal suspensions [4, 5], nanofluidics [6], blood flow [7, 8], multiphase flows [9] and polymer chains [10]. Given that the method does not have a mesh or node connectivity, SPH uses a kernel estimation at Lagrangian points (particles) to approximate the partial differential equations (PDEs) that govern the system of interest. As a consequence of its Lagrangian description, advection is treated exactly, allowing the simulation of arbitrary free-shear flow in systems with complex geometries without the need to use an adaptive mesh or interface tracking [11, 12]. Another important feature of the method is its inherent adaptivity, as particle attributes evolve according to their material time derivative [13]. More recently, the development of multi-resolution SPH brings the method closer to industrial applications by adaptively increasing the resolution by means of splitting particles in regions of interest, and coalescing particles in regions where lower resolution suffices [14, 15, 16, 17, 18].

As an example of the SPH formulation, consider the conservation laws for mass and momentum in a Lagrangian reference

$$\frac{\partial \rho}{\partial t} = -\rho \boldsymbol{\nabla} \cdot \boldsymbol{v}, \tag{1.1}$$

$$\frac{\partial \boldsymbol{v}}{\partial t} = -\frac{1}{\rho} \boldsymbol{\nabla} \cdot \boldsymbol{\sigma}, \tag{1.2}$$

where $\rho, \boldsymbol{v}, t, \boldsymbol{\sigma}$ refer to density, velocity, time and stress tensor, respectively. In the equations above, temporal derivatives shall be understood as material derivatives. For

fluids, the stress tensor $\boldsymbol{\sigma}$ can be written as

$$\boldsymbol{\sigma} = -P\boldsymbol{I} + 2\eta\boldsymbol{\epsilon}, \tag{1.3}$$

where $P, \boldsymbol{I}, \eta, \boldsymbol{\epsilon}$ denote the hydrostatic pressure, the second order identity tensor, dynamic viscosity and strain tensor, respectively.

The first approximation performed in SPH consists of a kernel interpolation: consider a continuous function f defined at coordinates $\boldsymbol{x}$ in $\Omega \subseteq \mathbb{R}^3$. Thus, the following identity holds for any f

$$f(\boldsymbol{x}) = \int_\Omega f(\boldsymbol{x}')\delta(\boldsymbol{x} - \boldsymbol{x}')dx', \tag{1.4}$$

where $\delta(\boldsymbol{x} - \boldsymbol{x}')$ is the Dirac delta function. In SPH, the Dirac function is approximated by a smoothing kernel function W with finite (compact) support h

$$f(\boldsymbol{x}) \approx \int_\Omega f(\boldsymbol{x}')W(\boldsymbol{x} - \boldsymbol{x}', h)dx'. \tag{1.5}$$

The accuracy of the approximation given by Eq. (1.5) depends on the choice of W. In order to find a good candidate for the interpolation process, the kernel function is often chosen based on three conditions: a) the normalization of the smoothing function, which requires its integral to be identically one in the volume Ω; b) the Dirac delta condition, which requires that $W(\boldsymbol{x} - \boldsymbol{x}', h) \to \delta(\boldsymbol{x} - \boldsymbol{x}')$ as the support h approaches zero; c) kernel compactness, which guarantees that $W = 0$ outside of its support.

After choosing W, the next step consists of rewriting the integral approximation given by Eq. (3.9) as a discrete sum. The domain Ω is then discretized using N particles, each located at coordinates $\boldsymbol{x}_i$. Each particle carries mass, volume, momentum, energy, concentration of species, and/or any other quantity of interest. We denote these quantities

here as the arbitrary function f,

$$f_i \approx \sum_{j=1}^{N} \frac{m_j}{\rho_j} f_j W_{ij}, \tag{1.6}$$

where m_j, ρ_j denote the mass and density and the kernel approximation of the field $f(\boldsymbol{x})$ at position $\boldsymbol{x}_j$, respectively. Since f_j is fixed, the gradient of f can be evaluated as

$$(\boldsymbol{\nabla} f)_i = \sum_{j=1}^{N} \frac{m_j}{\rho_j} f_j \boldsymbol{\nabla} W_{ij}, \tag{1.7}$$

where the resulting directional gradient operator is evaluated as

$$\boldsymbol{\nabla} W_{ij} = \frac{\boldsymbol{x}_{ij}}{x_{ij}} \frac{dW_{ij}}{dx_{ij}}, \tag{1.8}$$

and $\boldsymbol{x}_{ij} = \boldsymbol{x}_i - \boldsymbol{x}_j$, $x_{ij} = ||\boldsymbol{x}_{ij}||_2$ denote the relative position and distance between points i and j, respectively. The most common approximation of a second derivative (used in the viscous term in the momentum equation) is given by a combination of finite differences and SPH approximation

$$\left(\boldsymbol{\nabla}^2 f\right)_i = \sum_{j=1}^{N} \frac{m_j}{\rho_j} (f_j - f_i) \boldsymbol{x}_{ij} \cdot \boldsymbol{x}_{ij} \frac{1}{x_{ij}^2 + \varepsilon^2} \frac{dW_{ij}}{dx_{ij}}, \tag{1.9}$$

where ε is a small number $\mathcal{O}(10^{-5})$ to prevent a zero denominator and avoid singularities when $x_{ij} \approx 0$. Finally, we can now use the kernel interpolation and the discretization process to approximate Eqs. (1.1)-(1.2), for each particle i. The resulting discrete governing equations read

$$\frac{d\rho_i}{dt} = \rho_i \sum_{j=1}^{N} \frac{m_j}{\rho_j} \frac{\partial W_{ij}}{\partial x_{ij}} \frac{1}{x_{ij}} \boldsymbol{x}_{ij} \cdot \boldsymbol{v}_{ij}, \tag{1.10}$$

$$\frac{d\boldsymbol{v}_i}{dt} = \sum_{j=1}^{N} m_j \left(\frac{P_i}{\rho_i^2} + \frac{P_j}{\rho_j^2} \right) \frac{\boldsymbol{x}_{ij}}{x_{ij}} \frac{\partial W_{ij}}{\partial x_{ij}} + \sum_{j=1}^{N} m_j \frac{\eta_{ij} \boldsymbol{v}_{ij} \cdot \boldsymbol{x}_{ij}}{\rho_i \rho_j x_{ij}} \frac{\partial W_{ij}}{\partial x_{ij}}. \tag{1.11}$$

In order to close the model described by Eqs. (1.10)-(1.11), a relationship between density and pressure field must be established. In the Lagrangian fluid dynamics literature, two different approaches are widely used: 1) treat the flow as incompressible, either by solving a pressure-Poisson equation to obtain a divergence-free velocity field, or by requiring as a kinematic constraint that the volume of the fluid particles is constant; or 2) treat it as weakly compressible, and impose an equation of state. Most authors use the weakly compressible assumption. In this case, a common choice of equation of state is the so-called Tait's equation:

$$p = p_0 \left[\left(\frac{\rho}{\rho_0} \right)^{\gamma} - 1 \right], \tag{1.12}$$

where p_0, ρ_0 denote reference pressure and density, respectively (these are problem-dependent), and γ is the polytropic constant (usually $\gamma = 1$ or $\gamma = 7$ in most papers). It is a common practice to select $p_0 = \rho_0 c_0^2 / \gamma$, where c_0 is the artificial speed of sound. In order to limit density variations to 1%, c_0 is chosen such that it is at least 10 times higher than the characteristic velocity of the problem.

1.1.2   Dissipative Particle Hydrodynamics (DPD)

Notice that SPH works as a discretization method for PDEs: given a discrete set of particles, they interact with each other constrained by the PDE. This PDE-to-particle model is often referred as a *top-bottom* approach. In contrast, the dissipative particle hydrodynamics (DPD) method performs a *bottom-top* approach: given the particles and *ad-hoc* interaction forces, we can evolve the system using Newton's second law. Due to

its flexibility, the method originally developed by [19] and later modified by [20], was rapidly adopted for simulating dynamic and rheological properties of complex materials and non-Newtonian fluids. The method has been applied to a wide range of problems in physics and chemistry [21] including heat transfer [22, 23, 24], flow through porous media [25, 26] and shock-capturing [27, 28].

For a system of N particles, the evolution of a DPD particle i with unit mass follows the conservation of momentum

$$\frac{d\boldsymbol{v}}{dt} = \boldsymbol{F}_i = \sum_{j=1}^{N} \boldsymbol{F}_{ij}^C + \boldsymbol{F}_{ij}^D + \boldsymbol{F}_{ij}^R, \tag{1.13}$$

where t, $\boldsymbol{v}_i$ denote time and velocity of particle i. The pairwise terms $\boldsymbol{F}_{ij}^C$, $\boldsymbol{F}_{ij}^D$, $\boldsymbol{F}_{ij}^R$ denote conservative, dissipative and random forces acting on particle i due to j, given by

$$\boldsymbol{F}_{ij}^C = a_{ij}\omega_C(x_{ij})\boldsymbol{e}_{ij}, \tag{1.14}$$

$$\boldsymbol{F}_{ij}^D = -\gamma_{ij}\omega_D(x_{ij})(\boldsymbol{e}_{ij} \cdot \boldsymbol{v}_{ij})\boldsymbol{e}_{ij}, \tag{1.15}$$

$$\boldsymbol{F}_{ij}^R = \sigma_{ij}\omega_R(x_{ij})\epsilon_{ij}(\Delta t)^{-1/2}\boldsymbol{e}_{ij}, \tag{1.16}$$

where $\boldsymbol{x}_{ij}$ is the coordinates of particle i, $x_{ij} = |\boldsymbol{x}_{ij}|$, $\boldsymbol{e}_{ij} = \boldsymbol{x}_{ij}/x_{ij}$ is the unit vector from particle j to i and $\boldsymbol{v}_{ij} = \boldsymbol{v}_j - \boldsymbol{v}_i$ is the velocity difference. Terms $\omega_C, \omega_D, \omega_R$ denote weight (radial basis) functions, that limit the effect of neighbor particles j on particle i to only a subset of N particles. Finally, $a_{ij}, \gamma_{ij}, \sigma_{ij}$ denote conservative, dissipative and random parameters, respectively, to be calibrated depending on the problem.

Despite the success of DPD as a simple, robust and intuitive method, a number of conceptual shortcomings have been reported [29, 30, 31]. Perhaps the major one is the lack of direct mapping between the model parameters and the physical parameters of

the system. This problem is still an open area of research, and as a consequence, DPD parameters must be calibrated on a case-by-case basis using empirical equations, often in a non-unique way [31, 32, 33]. Other shortcomings of the DPD method include the impossibility of imposing an equation of state directly in the model [31] and the risk of particle overlap due to the use of soft potentials [29].

1.1.3   Smoothed Dissipative Particle Hydrodynamics (SDPD)

The shortcomings of the DPD formulation were addressed by [34], who proposed the combination of the SPH method to model the hydrodynamics, with an additional stochastic term to model the thermal fluctuations in the mesoscale. The resulting method, named Smoothed Dissipative Particle Hydrodynamics (SDPD), inherits the benefits of second-order discretization of the Navier-Stokes equations in the Lagrangian form from SPH [29, 35], along with the thermodynamic consistency of DPD [34]. For this method, transport coefficients and equations of state can be imposed as inputs directly in the model. Moreover, physical scales are consistent with the Navier-Stokes equations, and therefore hydrodynamic behavior is obtained.

SDPD shares many similarities with SPH, including the use of arbitrarily distributed particles to represent the state of the system, their Lagrangian nature, and the easiness of extending it to multiphysics applications. It has been sucessfully applied to a large variety of problems such as colloidal suspensions [4, 5], nanofluids [6], blood flow [7, 8], multiphase flows [9] and polymer chains [10].

A canonical formulation for SDPD consists of the same kernel interpolation and the discretization process used in SPH, Eqs. (1.10)-(1.11), along with the stochastic term $d\tilde{\boldsymbol{v}}/dt$ in the momentum equation. The resulting discrete governing equations are given

by

$$\frac{d\rho_i}{dt} = \rho_i \sum_{j=1}^{N} \frac{m_j}{\rho_j} \frac{\partial W_{ij}}{\partial x_{ij}} \frac{1}{x_{ij}} \boldsymbol{x}_{ij} \cdot \boldsymbol{v}_{ij}, \tag{1.17}$$

$$\frac{d\boldsymbol{v}_i}{dt} = \sum_{j=1}^{N} m_j \left(\frac{P_i}{\rho_i^2} + \frac{P_j}{\rho_j^2} \right) \frac{\boldsymbol{x}_{ij}}{x_{ij}} \frac{\partial W_{ij}}{\partial x_{ij}} + \sum_{j=1}^{N} m_j \frac{\eta_{ij} \boldsymbol{v}_{ij} \cdot \boldsymbol{x}_{ij}}{\rho_i \rho_j x_{ij}} \frac{\partial W_{ij}}{\partial x_{ij}} + \frac{d\tilde{\boldsymbol{v}}}{dt}. \tag{1.18}$$

A complete description of the form of the stochastic term $d\tilde{\boldsymbol{v}}/dt$ is provided in detail in Chapter 2.

1.2   Modeling of multiscale problems

With the advances in computational power, the complexity of the models used to simulate systems in science and engineering has dramatically increased. These models span microscopic to macroscopic scales and multiple types of physics simulations, including fluid dynamics, solid mechanics, chemical reactions and transport, and thermodynamics. For systems in which the scales of time and space are sufficiently small (microscale), simulations are performed using molecular dynamics (MD) [36] with potential energy functions derived from classical mechanics. For macroscale systems involving a well-mixed system, continuum approaches (e.g., Navier-Stokes equations) are typically employed. At the intermediate mesoscale, recent work by [37] has integrated reaction-diffusion of chemical species within a particle-based fluid dynamic framework. In the field of cell biology, it has been found that models with discrete stochastic dynamics are often required to recapitulate biologically relevant phenotypes [38]. Recent work has shown the importance of cellular level models with dynamic domain shapes and external flows coupled to discrete stochastic biochemical simulations [39, 40].

Typically in fluid dynamics simulations, macroscale approaches based on continuum

methods rely on the continuum hypothesis and local equilibrium assumptions. By considering volumes of particles as local thermodynamic systems, one can reduce the number of degrees of freedom by several orders of magnitude, because not all the scales of the system are resolved. This truncation of scales allows the simulation of larger systems for longer physical times. In this sense, continuum theories can be seen as coarse-grained versions of the atomic system [36].

The Knudsen number (Kn), defined as the ratio of the mean free path of the molecules being transported over a characteristic length scale [41], helps to determine whether it is meaningful to use a macroscopic approach. According to [42], molecular effects become the dominant transport mechanism in fluid motion when $Kn \geq 10$. However, at the so-called transitional regime, $10^{-1} \leq Kn \leq 10^1$, several important phenomena involving molecular effects take place in complex systems [36] such as biological flows, and the behavior of polymers and colloids. In this regime, scales are considered mesoscopic, with spatio-temporal ranges in the interval $\mathcal{O}(10^{-9})$ - $\mathcal{O}(10^{-5})$ meters and $\mathcal{O}(10^{-9})$ - $\mathcal{O}(10^{-3})$ seconds [36], making the number of degrees of freedom required in a MD simulation currently impractical [29, 35, 30, 36]. The most recent MD simulations are constrained to $\mathcal{O}(10^9)$ atoms and up to $\mathcal{O}(10^{-9})$ seconds [30].

To capture the effect of a wide range of scales, one possible approach consists in developing *hybrid methods*. The idea of these methods is to solve microscopic scales only where is needed. For example, consider the simulation of a biological system where advection and reaction–diffusion occur at different scales, ranging from the microscopic (e.g. stochastic molecular binding interactions) to the macroscopic (e.g. fluid flow): a neutrophil in the blood can track down a single bacterium by sensing individual bacterial peptides that diffuse to and bind neutrophil receptors, triggering a biochemical response while experiencing the hydrodynamic forces from blood flow (Fig. 1). Physical forces, chemical reactions, diffusion, active transport, stochastic dynamics, and advection must
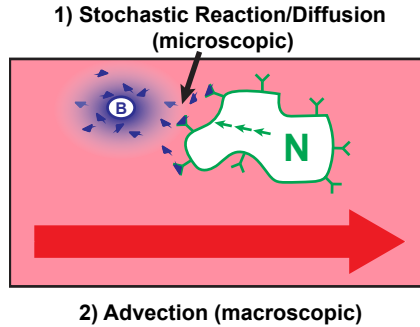
Figure 1.1: Example of biological system possessing reaction, diffusion, advection, and stochastic dynamics. In an artery, a neutrophil (N) chemotaxes against the blood flow toward a bacterium (B) by sensing the gradient of individual bacterial peptides (blue triangles) that bind receptors (green Y-shapes) on the neutrophil cell surface.

all be modeled, which presents a formidable challenging for any computational framework. Even commercial software solutions such as Comsol Multiphysics can capture the deterministic spatial dynamics but not the stochastic dynamics. The spatial stochastic simulation algorithm (sSSA) simulates stochastic reaction–diffusion dynamics, but is ill-suited for representing fluid flow by itself.

Then, why not using particle-based methods, such as SDPD, to solve these problems? Currently, there are two crucial factors that limit their applicability biophysical problems: (a) the lack of a discrete spatial stochastic formulation for reaction-diffusion systems, and (b) the onset of numerical instabilities that cause particles to penetrate moving wall boundaries and generates excessive diffusion, leading to a fast decay of energy and unrealistic results. In this dissertation, we propose solutions for both of these problems. In Chapter 2, we present a solution to (a), by proposing a new algorithm that merges a spatial stochastic simulation algorithm (sSSA) with the smoothed dissipative particle dynamics (SDPD) method. This hybrid method enables discrete stochastic simulation of spatially resolved chemically reacting systems on a mesh-free dynamic domain with a Lagrangian frame of reference. The spatial stochastic fluid dynamics is resolved using SDPD, a method that combines two popular mesoscopic techniques: smoothed par-

ticle hydrodynamics and dissipative particle dynamics (DPD), linking the macroscopic and mesoscopic hydrodynamics effects of these two methods. The spatial stochastic reaction-diffusion is then resolved using a discrete stochastic simulation algorithm using the reaction-diffusion master equations (RDME) formalism. We validate the new method by comparing our results to four canonical models, and demonstrate the versatility of our method by simulating a flow containing a chemical gradient past a yeast cell in a microfluidics chamber.

In Chapter 3, we propose a new approach that explicitly prevents particle penetrations in boundaries, and develop a systematic approach to prevent numerical instabilities. These algorithms are combined into a new weakly-compressible smoothed particle hydrodynamics (SPH) method capable of modeling non-slip fixed and moving wall boundary conditions. The formulation combines a boundary volume fraction (BVF) wall approach with an arbitrary Lagrangian-Eulerian (ALE)-SPH method. The resulting method, named SPH-BVF, offers detection of arbitrarily shaped solid walls on-the-fly, with small computational overhead due to its local formulation. This framework is capable of solving problems that are difficult or infeasible for standard particle-based methods, namely flows subject to large shear stresses or at moderate Reynolds numbers, and mass transfer in deformable boundaries, which is common in biological systems. We validate the method on canonical fluid flow, convective transport, and fluid-structure interaction problems, and demonstrate its versatility by simulating a complex biomechanical process: the formation of a yeast mating projection.

Finally, in Chapter 4 we summarize our results. The accuracy of the method presented in Chapters 2 and 3, along with the qualitative agreement with yeast experiments, confirms that the usage of sSSA with the SPH-BVF method provides a robust particle-based multiphysics framework that extends the reach of particle-based methods to new types of problems including those of biological relevance.

Chapter 2

Resolving multiple scales: a new SDPD-sSSA method for advection-diffusion-reactions problems

2.1 Motivation

In this chapter we introduce a novel formulation of advection-diffusion-reaction in SDPD. For systems where the molecular discreteness is relevant, we propose to simulate the reaction-diffusion of species by use of the spatial stochastic simulation algorithm (sSSA) to resolve the reaction-diffusion master equation (RDME) [43, 44, 45]. An immediate advantage of the spatial stochastic approach is that transport of species is computed exactly, instead of approximately by adding a fluctuation term to the deterministic reaction-diffusion equations. On the other hand, in regions where small scales are negligible, we solve a deterministic form of the SDPD reaction-diffusion equation, thereby

avoiding over-resolving of scales, resulting in increased computational efficiency.

Compared to mesh-based standard approaches, such as finite elements (FEM), finite differences (FDM) and finite volume (FVM) methods, the new hybrid sSSA-SDPD method introduced by this work presents important advantages. First, as a consequence of its Lagrangian description, the method allows the simulation of advection-diffusion-reaction systems with complex geometries without the need of using adaptive meshes or interface tracking. Additionally, the method is capable of simulating a broader range of problems, when compared with standard approaches. In particular, the method is well-suited for fluid flow problems where stochastic reactive-diffusive mass transport is relevant.

One class of problems in which the hybrid method is expected to excel compared to alternative approaches is the simulation of biological systems where advection and reaction-diffusion occur at different scales, ranging from the microscopic (e.g. stochastic molecular binding interactions) to the macroscopic (e.g. fluid flow). For example, a neutrophil in the blood can track down a single bacterium by sensing individual bacterial peptides that diffuse to and bind neutrophil receptors, triggering a biochemical response while experiencing the hydrodynamic forces from blood flow (Fig. 1.1). Physical forces, chemical reactions, diffusion, active transport, stochastic dynamics, and advection must all be modeled, which presents a formidable challenge for any computational framework. Commercial software solutions such as Comsol Multiphysics can capture the deterministic spatial dynamics but not the stochastic dynamics. The spatial stochastic simulation algorithm (sSSA) [46] simulates stochastic reaction-diffusion dynamics, but is ill-suited for representing fluid flow.

This chapter is organized as follows: Section 2.2 briefly describes the SDPD and sSSA formulations. Section 2.3 focuses on the algorithmic description of the method proposed, with a discussion addressing its appropriate use in multiscale systems. Sec-

tion 2.4 presents validations, applications and discussion of relevant results. Conclusions and future perspectives are discussed in Chapter 4.

2.2 Background

The hybrid method proposed in this chapter is based on the combination of two formulations: SDPD and SSA. In this section, we provide a brief theoretical overview of these two key elements in the proposed hybrid method. In SDPD [34], the domain is discretized as a finite number of particles, each representing a small volume of material that carries properties such as momentum, mass and energy. The position of the particles evolves in time according to some mechanistic model, such as the fluctuating Navier-Stokes equations for fluid flow [47]. In contrast, the sSSA algorithm [46] consists of a stochastic model for mesoscopic-scale stochastic reaction-diffusion kinetics, where the domain is discretized in voxels and the system is modeled as a Markov process. For each voxel, the number of molecules of diluted species characterize the state of the system that evolves in time according to the Kolmogorov equation.

The hybrid method proposed uses either the sSSA algorithm or the SDPD formulation to compute mass reaction-diffusion processes, and SDPD to compute advection and other body force dynamics. This is achieved by treating each particle in the system as a voxel for the sSSA. The immediate consequence of using the hybrid sSSA-SDPD method is the ability to correctly predict the dynamics of multiscale systems in a unified framework, resolving hydrodynamics and low-concentration reaction-diffusion systems at the same time.

An overview of the mathematical models of an arbitrary system from a deterministic, SDPD and hybrid method perspective is depicted in Fig. 2.1. For detailed formulations of SSA and SDPD, we refer the reader to the work of [46] and [34], respectively.
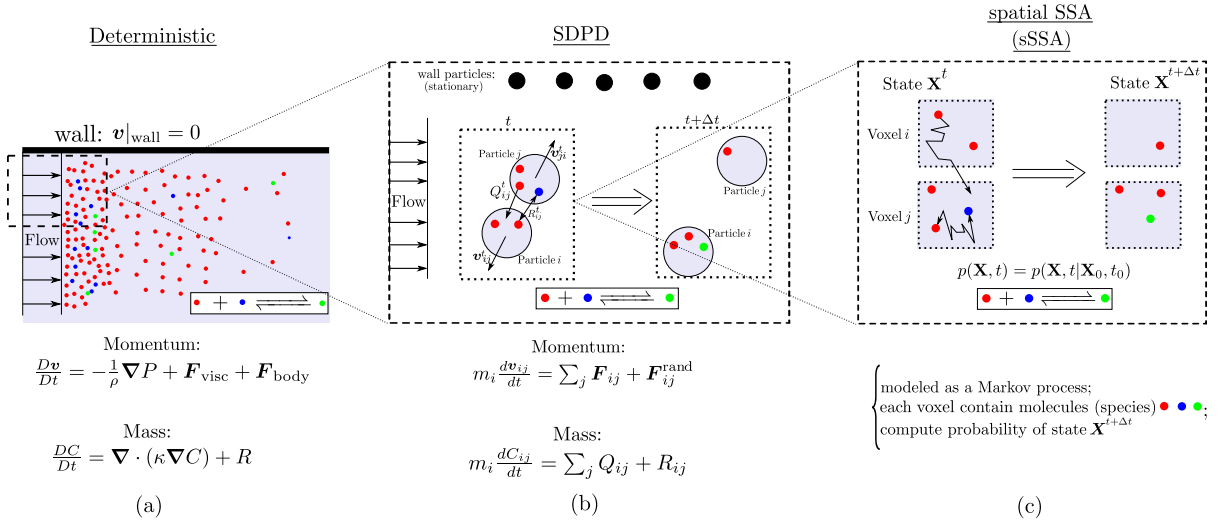
14

Figure 2.1:   Comparison between mathematical and physical models of (a) a typical deterministic approach, (b) SDPD, (c) sSSA, for the idealized case of a channel flow with diluted species. In the hybrid method, advection is modeled via SDPD, while mass transport can be modeled via either a spatial stochastic algorithm or SDPD, depending on whether stochastic effects are relevant. In Figs. (a) and (b), the dotted parts denote magnified regions, illustrating the differences between the methods. In Fig (b), v_{ij}, Q_{ij} and R_{ij} denote the pairwise velocity, flux of mass and reaction term, respectively. In Fig. (c), p in the Kolmogorov equation denotes the probability that the system can be found in state $\mathbf{X}$ at time t.

2.2.1   SDPD

Theoretical aspects

Consider a domain $\Omega \subset \Re^3$, composed of a collection of particles representing fluid volumes that evolve in time according to the isothermal Navier-Stokes equations and the reaction-diffusion equation:

$$\frac{d\rho}{dt} = -\rho\boldsymbol{\nabla}\cdot\boldsymbol{v}, \tag{2.1}$$

$$\frac{d\boldsymbol{v}}{dt} = -\frac{1}{\rho}\boldsymbol{\nabla}P + \boldsymbol{F}_{\text{visc}} + \boldsymbol{F}_{\text{body}}, \tag{2.2}$$

$$\frac{dC}{dt} = \boldsymbol{\nabla}\cdot(\kappa\boldsymbol{\nabla}C) + R, \tag{2.3}$$

where ρ, $\boldsymbol{v}$, P, $\boldsymbol{F}_{\text{visc}}$, $\boldsymbol{F}_{\text{body}}$, C, κ and R denote the fluid density, velocity, pressure, viscous force, body force, concentration, mass diffusivity and reaction term, respectively. The $d(\cdot)/dt$ operator denotes the material derivative [48], defined as

$$\frac{d(\cdot)}{dt} = \frac{\partial(\cdot)}{\partial t} + \boldsymbol{v}\cdot\boldsymbol{\nabla}(\cdot), \tag{2.4}$$

thus the characteristic curves of this operator are the particle trajectories [49]. Adopting a Lagrangian description, we consider each particle as a non-inertial frame of reference. Therefore, the advective acceleration term in Eq (3.4), $\boldsymbol{v}\cdot\boldsymbol{\nabla}(\cdot)$, vanishes identically, by virtue of having a zero relative velocity. Consequently, Eqs. (2.1)-(2.3) can be rewritten as

$$\frac{\partial\rho}{\partial t} = -\rho\boldsymbol{\nabla}\cdot\boldsymbol{v}, \tag{2.5}$$

$$\frac{\partial\boldsymbol{v}}{\partial t} = -\frac{1}{\rho}\boldsymbol{\nabla}P + \boldsymbol{F}_{\text{visc}} + \boldsymbol{F}_{\text{body}}, \tag{2.6}$$

$$\frac{\partial C}{\partial t} = \boldsymbol{\nabla}\cdot(\kappa\boldsymbol{\nabla}C) + R. \tag{2.7}$$

Equations (3.1)-(3.3) show that the temporal variation of the variables of interest depends on the evaluation of spatial derivatives of these physical quantities. The solution of these equations numerically, therefore, raises the question of how to approximate the

16

derivatives and transform these expressions into a set of algebraic equations involving the unknowns of the problem [49, 50].

In Eulerian-based methods, at each time step, points of space are arbitrarily selected as inertial frames of reference and therefore the spatial grid spacing is, in general, fixed. Thus, derivatives are typically piecewise-approximated using linear functions, polynomials, etc. In contrast, in a Lagrangian-based method, since particles are moving along with the flow, the evaluation of derivatives involves interpolation processes, usually based on radial smoothing kernel functions [49].

In order to find a good candidate for the interpolation process, consider a continuous function $f(\boldsymbol{x})$, defined at coordinates $\boldsymbol{x}$. Note the following identity [50]

$$f(\boldsymbol{x}) = \int_{\Omega} f(\boldsymbol{x}')\delta(\boldsymbol{x} - \boldsymbol{x}')dx', \tag{2.8}$$

where $\delta(\boldsymbol{x} - \boldsymbol{x}')$ is the Dirac delta function. Due to the infinitesimal support of the Dirac function and the finite decimal precision of computers, it is not possible to write a discrete numerical method using this integral representation of a function. In order to overcome this limitation, SPH theory approximates Eq. (2.8) by replacing the Dirac function with a smoothing kernel function W with finite support h

$$f(\boldsymbol{x}) \approx \int_{\Omega} f(\boldsymbol{x}')W(\boldsymbol{x} - \boldsymbol{x}', h)dx'. \tag{2.9}$$

Note that Eq. (2.9) is an approximation. The accuracy of the approximation depends on the choice of W. In the SPH literature, the smoothing kernel function is often chosen based on three conditions [25, 12]: a) the normalization of the smoothing function, which requires its integral to be identically one in the volume Ω; b) the Dirac delta condition, which requires that $W(\boldsymbol{x} - \boldsymbol{x}', h) \to \delta(\boldsymbol{x} - \boldsymbol{x}')$ as the support h approaches zero; c) kernel compactness, which guarantees that $W = 0$ outside of its support.

17

After judiciously choosing a function W, the next step consists of rewriting the integral approximation given by Eq. (2.9) as a discrete sum. The domain Ω is then discretized using N particles, each located at coordinates $\boldsymbol{x}_i$

$$\langle f(x_i) \rangle = \sum_{j=1}^{N} m_j \frac{f_j}{\rho_j} W(\boldsymbol{x}_i - \boldsymbol{x}_j), \tag{2.10}$$

where m_j and $\langle f_j \rangle$ denote the mass of particle j and the kernel approximation of the field $f(\boldsymbol{x})$ at position $\boldsymbol{x}_j$, respectively. As a consequence of the SPH formulation, since m_j and f_j are defined locally (i.e., they are particle properties), linear operators (such as the gradient) will affect only the weight function. Therefore, the gradient of f is given by

$$\langle \boldsymbol{\nabla} f(x_i) \rangle = \sum_{j=1}^{N} m_j \frac{f_j}{\rho_j} \boldsymbol{\nabla} W(\boldsymbol{x}_i - \boldsymbol{x}_j), \tag{2.11}$$

where the resulting directional gradient operator is evaluated as

$$\boldsymbol{\nabla} W(\boldsymbol{x}_i - \boldsymbol{x}_j) = \frac{\boldsymbol{x}_{ij}}{x_{ij}} \frac{dW(\xi)}{d\xi}, \tag{2.12}$$

with $\boldsymbol{x}_{ij} = \boldsymbol{x}_i - \boldsymbol{x}_j$, $x_{ij} = ||\boldsymbol{x}_{ij}||_2$ and ξ denoting a generalized coordinate. In this work, we have adopted the Lucy kernel, proposed by [3], with $\xi = x_{ij}/h$

$$W(\xi) = \begin{cases} \alpha_D \left(1 + 3\xi\right) \left(1 - \xi\right)^3, & \text{if } 0 \leq \xi \leq 1, \\ 0, & \text{otherwise.} \end{cases} \tag{2.13}$$

where the normalization parameter α_D depends on the number of dimensions of the problem

$$
\alpha_D = \begin{cases} 5/4h, & \text{if 1D,} \\ 5/\pi h^2, & \text{if 2D,} \\ 105/16\pi h^3, & \text{if 3D.} \end{cases} \tag{2.14}
$$

We proceed now by applying this methodology to Eqs. (3.1)-(3.3). The derivation of the deterministic part of the mathematical model, i.e., the SPH formulation, can be found in [49]. For a complete derivation of the SDPD method, the reader may refer to [34]. The resulting equations, disregarding body forces, are given by

$$
\frac{d\rho}{dt} = -\sum_{j=1}^{N} m_j \left(\boldsymbol{v}_{ij} \cdot \boldsymbol{x}_{ij} \right) \frac{1}{x_{ij}} \frac{dW}{d\xi}, + \xi h c_0 \sum_{j=1}^{N} \boldsymbol{\psi}_{ij} \cdot \boldsymbol{x}_{ij} \frac{1}{x_{ij}} \frac{dW}{d\xi} \tag{2.15}
$$

$$
\frac{d\boldsymbol{v}}{dt} = \left[-\sum_{j=1}^{N} m_j \left(\frac{P_i}{\rho_i^2} + \frac{P_j}{\rho_j^2} \right) \frac{1}{x_{ij}} \frac{dW}{d\xi} \right] + \left[\frac{5\eta}{3} \sum_{j=1}^{N} \frac{1}{x_{ij}^3} \frac{dW}{d\xi} \frac{\boldsymbol{v}_{ij} + (\boldsymbol{v}_{ij} \cdot \boldsymbol{x}_{ij}) \boldsymbol{x}_{ij}}{\rho_i \rho_j} \right] + \frac{d\tilde{\boldsymbol{v}}}{dt},
$$

$$
\tag{2.16}
$$

$$
\frac{dC}{dt} = \left[-\sum_{j=1}^{N} m_j \frac{(\kappa_i + \kappa_j)(C_i - C_j)}{\rho_i \rho_j x_{ij}} \frac{dW}{d\xi} \right] + \frac{d\tilde{C}}{dt}. \tag{2.17}
$$

In Eq. (2.15), $\boldsymbol{\psi}_{ij}$ and ξ denote the artificial density diffusion and its amplitude, respectively. This correction was proposed by [51] as a way to reduce the numerical noise in the pressure evaluation for weakly-compressible SPH, and has the form

$$
\boldsymbol{\psi}_{ij} = 2 \left(\frac{m_i \rho_j}{m_j \rho_i} - 1 \right) \frac{\boldsymbol{x}_{ij}}{x_{ij}^2 + \varepsilon_h h^2}, \tag{2.18}
$$

where $\varepsilon_h \sim 0.01$ is a small scalar set to prevent numerical singularities [49, 52]. Considering the significant improvements presented by [51] in terms of stability, we have taken

19

the amplitude of the artificial density diffusion to be $\xi = 0.1$.

The random terms $d\tilde{\boldsymbol{v}}/dt$ are introduced in the equations as a tensorial generalization of a stochastic Wiener process [31],

$$\frac{d\tilde{\boldsymbol{v}}}{dt} = \sum_{j=1}^{N} \left[\left(\frac{40}{3} \frac{\eta \kappa_B T_0}{\rho_i \rho_j} \frac{dW}{d\xi} \right)^{1/2} \frac{d\widehat{\mathbf{W}}_{ij}}{dt} \cdot \frac{\boldsymbol{x}_{ij}}{x_{ij}} \right], \tag{2.19}$$

$$\tag{2.20}$$

where

$$d\tilde{\mathbf{W}}_{ij} = \frac{\tilde{\mathbf{W}}_{ij} + \tilde{\mathbf{W}}_{ij}^{T}}{2}, \tag{2.21}$$

is the symmetric part of a matrix of independent increments in the Wiener process [31], κ_B is the Boltzmann constant and T_0 is a characteristic temperature of the system. For the random term in the reaction-diffusion equation, we follow the assumptions described by [37], that disregard the influence of the random term in diffusive processes, based on the fact that the mass of a single solute molecule $m_{s,i}$ is small compared to the mass of the SDPD particle m_i. Therefore, we assume that $d\tilde{C} \ll dC$.

To close the model described by Eqs. (2.15)-(2.17), a relationship between density and pressure field must be established. In the Lagrangian fluid dynamics literature, two different approaches are widely used: 1) treat the flow as incompressible, either by solving a pressure-Poisson equation to obtain a divergence-free velocity field [52, 53], or by requiring as a kinematic constraint that the volume of the fluid particles is constant [54]; or 2) treat it as weakly compressible, and impose an equation of state [3, 55, 31, 56, 12].

In the present work, we have followed the classical weakly-compressible SPH approaches, where the pressure of a fluid particle is obtained from the density field using

an equation of state [11]. A common choice is the so-called Tait's equation of state [57, 56, 12]:

$$p = p_0 \left[\left(\frac{\rho}{\rho_0} \right)^{\gamma} - 1 \right], \tag{2.22}$$

where p_0, ρ_0 denote reference pressure and density, respectively, and γ is the polytropic constant. It is a common practice [56, 12] to select $p_0 = \rho_0 c_0^2 / \gamma$, where c_0 is the artificial speed of sound. In order to limit density variations to 1%, we choose $\gamma = 7$. Here, c_0 is chosen such that it is at least two orders of magnitude higher than the characteristic velocity of the problem.

Numerical aspects

Following several authors [58, 51, 11], the integration of Eqs. (2.15)-(2.17) was performed using a two-step predictor-corrector scheme. Specifically, considering $\boldsymbol{Y} = [\boldsymbol{v}_i, \rho_i, C_i]$ the vector of unknowns of the system

$$\frac{\partial \boldsymbol{Y}}{\partial t} = f(\boldsymbol{Y}, t), \tag{2.23}$$

the explicit trapezoidal method is given by

$$\tilde{\boldsymbol{Y}} = \boldsymbol{Y}^{n-1} + \Delta t f(t^{n-1}, \boldsymbol{Y}^{n-1}), \tag{2.24}$$

$$\boldsymbol{Y}^n = \boldsymbol{Y}^{n-1} + \frac{\Delta t}{2} \left(f(t^{n-1}, v^{n-1}) + f(t^n, \tilde{\boldsymbol{Y}}) \right),$$

which requires the evaluation of f only once per time step. A necessary condition for stability, given by the Courant-Friedrichs-Lewy condition based on the artificial speed of sound c_0, was used to estimate a suitable time step Δt for each simulation [12].

2.2.2   SSA and RDME

It has been observed that mean-field or deterministic models are often insufficient to capture the relevant dynamics of many biological systems [59, 60, 61]. At this cellular level, biochemical systems in which the copy number of any relevant chemical species is sufficiently small can be more accurately modeled with discrete stochastic simulation, of which the most popular method is the Stochastic Simulation Algorithm (SSA) or Gillespie algorithm [62]. The SSA assumes that the system is spatially homogeneous, or well-mixed. To model spatially inhomogeneous stochastic biochemical systems at the mesoscopic scale, reaction-diffusion master equation (RDME)[46]-based methods, which discretize space into spatially homogeneous voxels [43, 44, 45], are often used. In our spatial SSA (sSSA), we integrate the RDME-based methods with a particle-based fluid dynamics simulation framework by using each SDPD particle as a RDME voxel: for each particle in the system, the stochastic chemical reactions take place *inside* the particles, and the stochastic diffusion occur *in between* neighbor particles.

The spatial SSA algorithm is based on the Reaction-Diffusion Master Equation (RDME) formalism [46]. The RDME is a mathematical model for spatially-resolved mesoscopic-scale stochastic chemical reaction-diffusion kinetics. It gives the time evolution of the probability distribution for the state of the system. First, the physical domain is partitioned into K non-overlapping subvolumes or voxels, similar to numerical methods for PDEs. Molecules are taken to be point particles and the state of the system is the discrete number of molecules of each species for each of the voxels in the domain. Modeling the reaction-diffusion dynamics as a Markov process gives the following forward Kolmogorov equation for the time evolution of $p(\mathbf{X}, t) = p(\mathbf{X}, t|\mathbf{X}_0, t_0)$ (the probability that the system can be found in state $\mathbf{X}$ at time t, conditioned on the initial condition $\mathbf{X}_0$ at time t_0):

$$\frac{\partial p(\mathbf{X}, t)}{\partial t} = \mathcal{R}p(\mathbf{X}, t) + \mathcal{D}p(\mathbf{X}, t), \tag{2.25}$$

$$\mathcal{R}p(\mathbf{X}, t) = \sum_{i=1}^{K}\sum_{r=1}^{M} a_{ir}(\mathbf{X} - \nu_{ir})p(\mathbf{X} - \nu_{ir}, t) - a_{ir}(\mathbf{X})p(\mathbf{X}, t), \tag{2.26}$$

$$\mathcal{D}p(\mathbf{X}, t) = \sum_{s=1}^{S}\sum_{i=1}^{K}\sum_{j=1}^{K} d_{sij}(\mathbf{X} - \mu_{sij})p(\mathbf{X} - \mu_{sij}, t) - d_{sij}(\mathbf{X})p(\mathbf{X}, t), \tag{2.27}$$

where $\mathbf{X}$ is a $K \times S$ state matrix, and S is the number of chemical species. The functions $a_{ir}(\mathbf{X}_i)$ define the propensity functions of the M chemical reactions, and ν_{ir} are stoichiometry vectors associated with the reactions. The propensity functions are defined such that $a_{ir}(\mathbf{X})\Delta t$ gives the probability that reaction r occurs in a small time interval of length Δt. The stoichiometry vector ν_{ir} defines the rules for how the state changes when reaction r is executed. $d_{ijs}(\mathbf{X}_i)$ are propensities for the diffusion jump events, and μ_{ijs} are stoichiometry vectors for diffusion events. μ_{ijs} has only two non-zero entries, corresponding to the removal of one molecule of species X_s in voxel i and the addition of a molecule in voxel j. The propensity functions for the diffusion jumps, d_{ijs}, are selected to provide a consistent and local discretization of the diffusion equation.

We do not solve the RDME directly. Instead, we generate sample paths of the underlying stochastic process. The SSA does this by generating two random numbers on each time step r_1 and r_2. These determine which reaction event r will fire next and at what time τ it will fire. These are based on the probabilistic reaction rates (called *propensities*). Next, the system state is updated by applying the stoichiometry vector ν_{*r} for reaction r to the state vector $\mathbf{X}$. The propensity functions are updated, the time is incremented by τ, and the procedure continues until the final time. This procedure is outlined in Algorithm 4.

23

Algorithm 1 SSA Reactions

Input: Current population of species in each particle: $\mathbf{X}_{is}$, Set of SSA reactions $r \in R$
  and propensity functions $a_r(\mathbf{X}_{i*})$, Integration timestep τ_{step}

Output: Population of each SSA species in each particle at time $t + \tau_{step}$.

 1: Calculate $a_{ir} = a_r(\mathbf{X}_{i*})$; $\quad a_0 = \sum_i \sum_r a_{ir}$
 2: $t' = 0$; $\quad r_1, r_2 \in URN(0,1)$; $\quad t' \mathrel{+}= -\log(r1)/d_0$
 3: **while** $t' < t_{split}$ **do**
 4: $\quad$ Find: $\max_{\mu_i \mu_r} \left[a_0 r_1 > \sum_i^{\mu_i} \sum_r^{\mu_r} a_{ir} \right]$
 5: $\quad$ $\mathbf{X}_{\mu_i \mu_s} \mathrel{+}= \nu_{\mu_i \mu_r}$
 6: $\quad$ Update: a_{ir}, a_0
 7: $\quad$ $r_1, r_2 \in URN(0,1)$
 8: $\quad$ $t' \mathrel{+}= -\log(r1)/a_0$
 9: **end while**

For SSA diffusion, we use a $K \times K$ matrix, the diffusion matrix $\mathcal{D}$, where $\mathcal{D}_{ij}$ is the diffusion propensity for molecules to jump from particle i to particle j. Following the formulation of [63], it is defined as:

$$
\mathcal{D}_{ij} = \begin{cases} -2 \frac{m_i m_j}{m_i + m_j} \frac{\rho_i + \rho_j}{\rho_i \rho_j} \frac{x_{ij}^2}{x_{ij}^2 + \varepsilon_h h^2} \frac{dW}{d\xi}, & \text{if } i \neq j, \\[2ex] -\sum_{n, n \neq j} \mathcal{D}_{nj}. & \text{if } i = j. \end{cases} \tag{2.28}
$$

This procedure to solve the SSA diffusion over a time interval $[t, t + \tau_{step}]$ is shown in Algorithm 2.

Algorithm 2 SSA Diffusion

Input: Current particle positions: $\boldsymbol{x}_i$, Current population of species in each particle:
$\mathbf{X}_{is}$, Set of SSA species diffusion coefficients: κ_{ijs}, Integration timestep τ_{step}

Output: Population of each SSA species in each particle at time $t + \tau_{step}$.

1: Create flux $K \times S$ matrix $\mathcal{Q} = 0$
2: Calculate diffusion matrix $\mathcal{D}$ [Eq.(2.28)]
3: Calculate $d_{ijs} = \kappa_{ijs}\mathcal{D}_{ij}\mathbf{X}_{is}$; $d_0 = \sum_i \sum_j \sum_s d_{ijs}$
4: $t' = 0$; $r_1, r_2 \in URN(0,1)$; $t' \mathrel{+}= -\log(r1)/d_0$
5: **while** $t' < t_{split}$ **do**
6:     Find: $\max_{\mu_i\mu_j\mu_s}\left[d_0 r_1 > \sum_i^{\mu_i} \sum_j^{\mu_j} \sum_s^{\mu_s} d_{ijs}\right]$
7:     $\mathbf{X}_{\mu_i\mu_s} --$; $\mathcal{Q}_{\mu_i\mu_s} --$; $\mathcal{Q}_{\mu_j\mu_s} ++$
8:     Update: d_{ijs}, d_0
9:     $r_1, r_2 \in URN(0,1)$
10:     $t' \mathrel{+}= -\log(r1)/d_0$
11: **end while**
12: $\mathbf{X}_{is} \mathrel{+}= \mathcal{Q}_{is} \forall i, s$

2.3   Proposed method

2.3.1   Overview

The goal of the proposed hybrid method is to provide an alternative framework for the simulation of multiscale systems that potentially involve a broad spectra of Knudsen numbers, involving micro-, meso- and macro-scopic scales. Thus, advection-diffusion-reaction problems could be resolved by the same method and numerical solver, without the burden of over-resolving small scales when not needed, nor truncating fluctuations in meso/microscale regimes.

The algorithm treats advection via the Navier-Stokes equations using the SDPD formulation, and reaction-diffusion by either SSA, SDPD or both. Coupling between advection and diffusion with body forces, e.g., in natural convection phenomena, takes place via SSA or SDPD diffusion, depending on the nature of the problem.

As described in Eq. (2.15), the SDPD formulation includes a random force term, and

the momentum equation is then treated as a stochastic differential equation (SDE). Depending on the Knudsen number, random effects might be relevant or not. For instance, consider a flow of red blood cells: in a macroscale regime, the effects of the random force do not change significantly the bulk motion that is transporting the cells; therefore, the force term might be disregarded and the SDPD equations are reduced to the standard SPH formulation. For the transport inside one of the cells, however, diffusion occurs in a meso/microscale regime, thus SSA could be used to resolve interactions.

2.3.2 Algorithm

Our algorithm utilizes a first order operator splitting method to decouple and simultaneously solve the SDPD fluid dynamics, the SDPD deterministic reaction-diffusion, and the SSA stochastic reaction-diffusion equations over the same time interval $[t, t + \tau_{step}]$. First, we time integrate equations (2.15), (2.16), and (2.17) over the interval using an explicit trapezoidal method. Then, we execute the SSA chemical reaction simulation [Algorithm 4] within each voxel/SDPD particle. Finally, we execute the SSA diffusion simulation [Algorithm 2] between all voxel/SDPD particles. The procedure to solve the full system is shown in Algorithm 3.

Algorithm 3 Hybrid SDPD-SSA method

Input:
 1: Domain region and boundary conditions,
 2: Initial Particle Positions/masses/velocities,
 3: Particle pair interactions,
 4: Set of SDPD species: diffusion coefficients & initial concentrations,
 5: Set of SDPD reactions,
 6: Set of SSA species: diffusion coefficients & initial populations,
 7: Set of SSA reactions,
 8: Integration timestep τ_{step}, h, ρ, e, t_{final}
Output: At each sample time, for each particle: position, velocity, concentration of each
    SDPD species, population of each SSA species.
 9:    $t = 0$
10: **while** t $< t_{final}$ **do**
11:     Solve for new position of SDPD particles [Eq.(2.15)]
12:     Solve for new velocity of SDPD particles [Eq.(2.16)]
13:     Solve deterministic reaction-diffusion [Eq.(2.17)]
14:     Solve SSA reactions [Algorithm 4]
15:     Solve SSA diffusion [Algorithm 2]
16:     $t = t + \tau_{step}$
17: **end while**

2.4   Results

In this section we provide experimental validations of the proposed hybrid method.
Section A discusses a one-dimensional, stationary reaction-diffusion problem, and Section B compares results of a classical advection-diffusion problem with the literature.
Validations for 1D and 2D diffusion are provided in the Supplementary Information.

2.4.1   Validation for one-dimensional diffusion

The first validation case to be considered is the one-dimensional transient, isotropic
diffusion problem. Dirichlet boundary conditions are imposed on both sides of the domain, and the initial concentration of the domain is kept as zero. The physical model of

the problem is depicted in Fig. 2.2a. All of the physical parameters are expressed in SI units.

The concentration of an arbitrary species $C(x,t) : [0,1] \times [0,\infty) \to \Re$ evolves along time in a domain $\Omega = [0,1]$. The mathematical model is given by:

$$\frac{\partial C}{\partial t} = \kappa \frac{\partial^2 C}{\partial x^2}, \tag{2.29}$$

with Dirichlet boundary conditions $C(0,t) = C_0$, $C(1,t) = 0$ and initial condition $C(x,0) = 0$. The initial-boundary value problem can be solved analytically, using separation of variables. The solution has the form:

$$C(x,t) = C_0(-x+1) - \sum_{n=1}^{\infty} \left(\frac{2C_0}{n\pi}\right) \sin(n\pi x)e^{-n^2\pi^2\kappa t}. \tag{2.30}$$

The problem is solved using both SSA and SDPD diffusion formulations. Boundary conditions are modeled as layers of particles with fixed imposed concentrations. The mass diffusivity $\kappa = 0.1[m^2/s]$ is kept constant, and a total of three levels of refinement were used, with the distance between particles $\Delta x = 1/16$, $1/32$ and $1/64$. A time step $\Delta t = 10^{-4}[s]$ was used to ensure stability.

Due the stochastic nature of the SSA algorithm, results were rendered as averages of multiple realizations in order to be compared with the SDPD and exact solutions. For all of the three cases considered, $N_r = 100$ realizations were performed. Hence, the SSA results should be interpreted as first-order statistical moments, i.e., average and standard deviation.

Temporal profiles comparing SSA and SDPD with the exact solution are shown in Fig. 2.2b. A quick analysis of the curves show that the SSA solution is in good agreement with the exact solution, with larger deviations in the central region of the domain. Such difference can be explained due to the increase of the number of possible resulting states

Table 2.1: Results: validation of 1D transient diffusion.

Δx	N	$\epsilon^{\mathrm{SDPD1}}$	ϵ^{SSA2}	C_0
1/16	17	6.617×10^{-4}	8.514×10^{-4}	1.6×10^5
1/32	33	4.669×10^{-4}	5.278×10^{-4}	3.2×10^5
1/64	65	3.764×10^{-4}	8.070×10^{-4}	6.4×10^5

of the system. Similarly, time also has an influence in the deviation: as time passes, the distance from the deterministic region (initial condition) increases.

Table 2.1 shows the quantitative results obtained. Errors ϵ^{SDPD} and ϵ^{SSA} were computed using the L^2 norm of the difference between the present method and reference solutions, normalized by the number of particles in the domain, i.e.,

$$\epsilon = \frac{\sqrt{\sum_{n=1}^{N}(C_i - C_i^{\mathrm{ref}})^2}}{C_0 N}, \tag{2.31}$$

where C_i^{ref} is a reference concentration, e.g., the exact solution, when available, C_0 is a normalization factor and N is the number of particles considered. A quick analysis of Table 2.1 shows that the errors using the traditional SDPD formulation have the same order of magnitude as those of the SSA-based transport. However, it is important to highlight that Lagrangian methods typically have optimal accuracy at equally-spaced, stationary lattices, as in the present validation case. Heterogeneous particle distributions caused by the irregular displacement of particles is a primary source of errors in Lagrangian methods based on kernel interpolation, such as SPH[57].
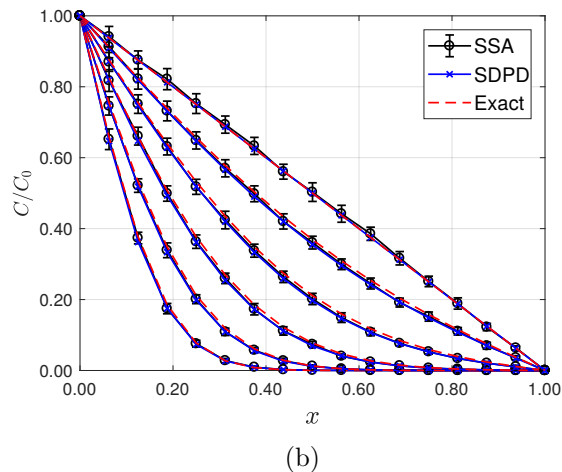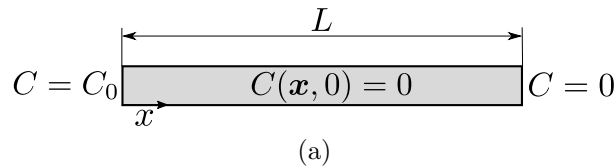
(a)

(b)

Figure 2.2: (a) Schematic of diffusion in a slab, with initial and boundary conditions. (b) Comparison of profiles of the normalized concentration for selected times (bottom to top: $t = 0.01, 0.02, 0.04, 0.08, 0.16$ and $1.0[s]$).

2.4.2 Validation for two-dimensional diffusion

The next validation case consists of a two-dimensional, steady-state, isotropic diffusion problem in a square region $\Omega = [0, 1] \times [0, 1]$, with a non-homogeneous Dirichlet boundary condition C_0 in the upper wall, and homogeneous conditions on the remaining boundaries, as shown in Fig. 2.3a. The initial condition is homogeneous, i.e., $C(\boldsymbol{x}, t = 0) = 0, \, \forall \, \boldsymbol{x} \in \Omega \mid \boldsymbol{x} \neq \partial\Omega$. We seek to find the steady-state by evolving the problem in time until it reaches the steady-state. The mathematical model is given by

$$\frac{\partial C}{\partial t} = \kappa \nabla^2 C, \tag{2.32}$$

30

where the steady-state exact solution is known to have the form

$$C(x, y) = \sum_{n=1}^{\infty} \frac{2C_0(1 - (-1)^n)}{n\pi} \frac{\sin(n\pi x)\sinh(n\pi y)}{\sinh(n\pi)}. \tag{2.33}$$

Simulations were performed using $17^2, 33^2$ and 65^2 equally-spaced particles distributed in a square domain of length $L = 1$. Dirichlet boundary conditions are modeled as layers of particles with fixed imposed concentrations, avoiding the truncation of the kernel in near-boundary regions. The mass diffusivity $\kappa = 10^{-2}[m^2/s]$ is kept constant, and a time step $\Delta t = 10^{-2}[s]$ was used.

A qualitative plot of the level set curves of the normalized concentration is described by Fig. 2.3b. Clearly, the SSA diffusion captured the physics of the problem, as the temporal average profiles described mostly overlap the exact solution.
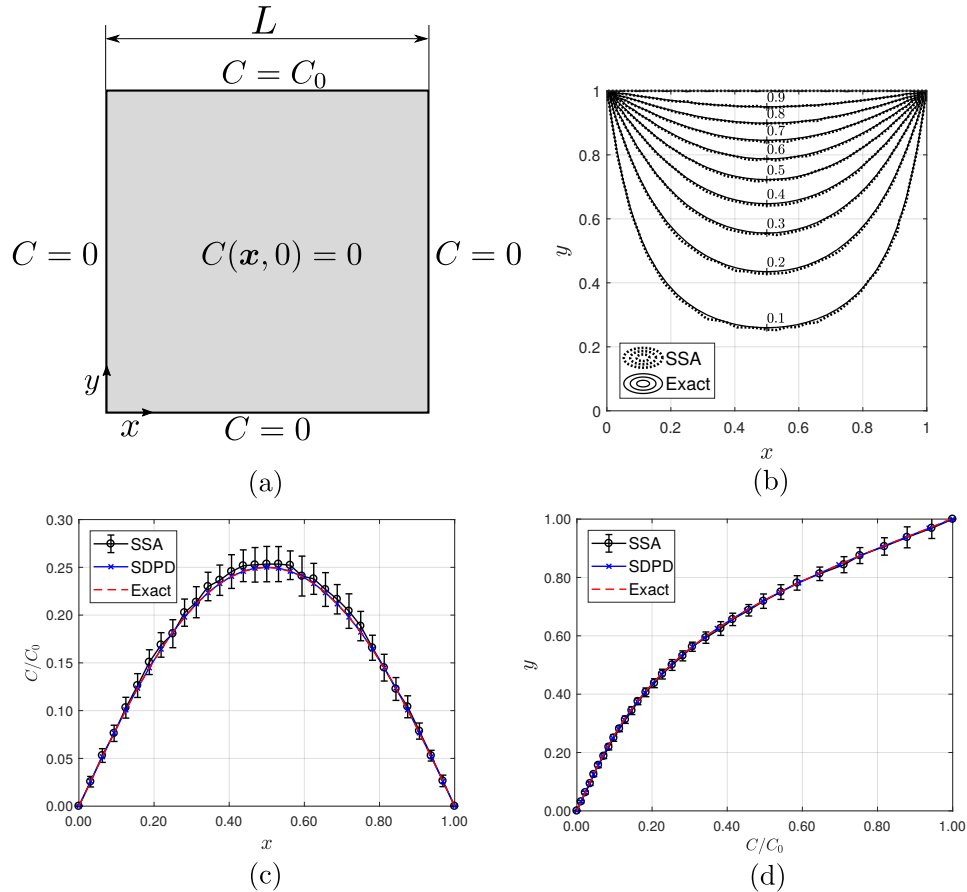
Figure 2.3: (a) Schematic of diffusion in a flat plate, with initial and boundary conditions. (b) Level set curves of the normalized concentration C/C_0 at steady-state, for 33^2 particles. (c) Horizontal and (d) vertical centerline profiles of the normalized concentration at steady-state, for the case with for $N = 33^2$ particles. SSA results were averaged over $N_r = 50$ realizations.

Figures 2.3c-2.3d show the horizontal and vertical centerline profiles of the normalized concentration C/C_0 at steady-state. Profiles of SSA-resolved concentrations, along with the standard deviation bars, were obtained as averages over $N_r = 50$ realizations. The analysis of these results show that standard deviations are smaller in the y-direction (Fig. 2.3d) than in the x-direction (Fig. 2.3c). As depicted in 2.3b, these errors are larger for smaller values of C/C_0. Since the horizontal centerline is located in the region $0 \lesssim C/C_0 \lesssim 0.3$ (i.e., smaller values of C/C_0), the occurrence of larger standard deviations is naturally expected.

32

Table 2.2: Results: diffusion in a flat plate.

Δx	N	ϵ^{SDPD3}	ϵ^{SSA4}	C_0
1/16	17^2	2.337×10^{-4}	2.902×10^{-4}	2.890×10^5
1/32	33^2	5.818×10^{-5}	1.294×10^{-4}	1.089×10^6
1/64	65^2	1.438×10^{-5}	2.043×10^{-4}	4.225×10^6

A list of the estimated L^2-norm errors is summarized in Table 3.4. Results of SSA and SDPD-based diffusion are comparable, with SSA errors about one order of magnitude larger than SDPD.

2.4.3 Validation for one-dimensional reaction-diffusion

The diffusion cases presented so far validated the diffusion treatment with sSSA and SDPD for Dirichlet boundary conditions. We now proceed by allowing reactions of different species to take place. The following test case was also used in the validation of the software Stochastic Simulation Service (StochSS [64]), for the case of a three-dimensional cylinder. For this case, all of the physical parameters are expressed in SI units.

Consider a domain $\Omega = [0, 1]$, with non-homogeneous Dirichlet boundary conditions imposed in the left and right walls. The walls are constrained with imposed concentrations arbitrary species C_A and C_B, as depicted in Fig. 2.4a. The initial conditions are homogeneous, $C_A(\boldsymbol{x}, t = 0) = C_B(\boldsymbol{x}, t = 0) = 0, \forall \boldsymbol{x} \in \Omega \mid \boldsymbol{x} \neq \partial\Omega$.

Species C_A and C_B interact with each other via mass action at a constant kinetic rate k_{AB}, leading to annihilation, i.e., $C_A + C_B \xrightarrow{k_{AB}} \emptyset$. The mathematical model that describes the system is given by

$$\frac{\partial}{\partial t} \begin{bmatrix} C_A \\ C_B \end{bmatrix} = \begin{bmatrix} \kappa_A & 0 \\ 0 & \kappa_B \end{bmatrix} \frac{\partial^2}{\partial x^2} \begin{bmatrix} C_A \\ C_B \end{bmatrix} + \begin{bmatrix} R_A \\ R_B \end{bmatrix}, \tag{2.34}$$

where κ_A, κ_B are the mass diffusivities, and R_A, R_B denote the reaction source terms. Based on the law of mass action, the reaction terms are given by

$$\begin{bmatrix} R_A \\ R_B \end{bmatrix} = \begin{bmatrix} -k_{AB}C_AC_B \\ -k_{AB}C_AC_B \end{bmatrix}. \tag{2.35}$$

The resulting system is a set of non-linear, coupled, second-order partial differential equations. Since there is no systematic way of obtaining the exact solution of this initial-boundary value problem, we propose its validation using high-fidelity numerical data as a reference. Thus, we performed the validation using an in-house code that solves the aforementioned problem using a 6th order tridiagonal compact finite-difference scheme [65], with grid spacing equivalent to the distance between particles used in the spatial SSA and SDPD simulations. The source code for our implementation of this solver is included as a file in the Supplementary Material.

Numerical simulations were performed using mass diffusivities $\kappa_A = \kappa_B = 0.1[m^2/s]$ and reaction kinetic rate $k_{AB} = 0.1[s^{-1}\text{molecules}^{-1}]$. Three levels of spatial refinement were used: 17, 33 and 65 equally-spaced particles, spaced $\Delta x = 1/16, 1/32, 1/64\,[m]$ of each other, respectively. A comparison of the concentration profiles solved using SSA and SDPD and contrasted with the compact finite difference solution is shown in Fig. 2.4b. SSA solutions were obtained as an average of $N_r = 100$ realizations.

Results show good agreement with the high-order reference solution. As expected,
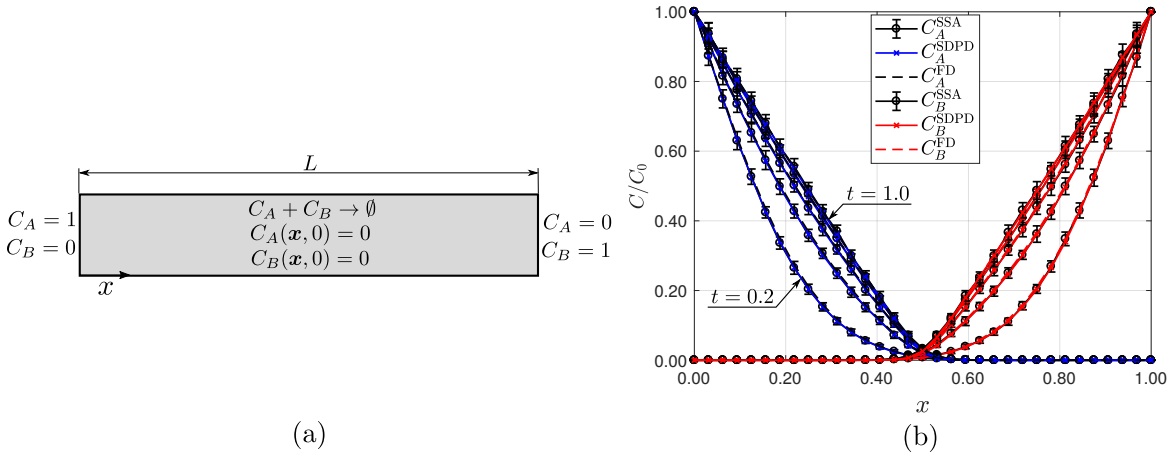
34

Figure 2.4: (a) Schematic of degradation reaction of two arbitrary species, with initial and boundary conditions. (b) Plot of the concentration of the chemical species along the length of the cylindrical domain, at $t = 0.2, 0.4, 0.6, 0.8$ and $1.0[s]$ for $N = 33$ particles.

Table 2.3: Estimated errors of reaction-diffusion in a cylinder.

Δx	N	ϵ^{SDPDa}	ϵ^{SSAb}	C_0
$1/16$	17	1.856×10^{-4}	7.285×10^{-4}	1.6×10^5
$1/32$	33	1.698×10^{-4}	5.334×10^{-4}	3.2×10^5
$1/64$	65	2.325×10^{-4}	6.644×10^{-4}	6.4×10^5

[a] Error computed at steady-state, $t = 100$.
[b] Error computed based at the mean profile of $N_r = 100$ at steady-state.

the concentration curves monotonically decrease towards the half-length of the domain, due to the symmetric nature of the problem.

Table 3.5 summarizes the errors for each simulation. Errors with SSA and SDPD showed the same order of magnitude, which indicates that SSA-based reaction-diffusion is able to accurately predict the physics of the problem. This result, along with the diffusion validations, indicate that there is no penalty in using SSA except for the burden of over-resolving scales, which increases the computational effort. However, notice that the opposite is not true, i.e., the usage of a deterministic approach does not necessarily reproduce the physics of the problem, as stochastic effects are relevant for $Kn \geq 10^{-1}$.

Thus, our method allows the simulation of cases even when it is not clear whether the stochastic effects are relevant or not, covering the whole spectrum of Knudsen numbers.

2.4.4 Boundary condition

For the hybrid SSA-SDPD and SDPD simulations, we adopted two different types of boundary conditions: in the y-direction, walls were modeled assuming perfectly elastic collisions, whereas in the x-direction we assumed periodic boundary conditions. The reason for the latter is to avoid the extra computational effort of destroying particles as they leave the domain and creating new ones at the inlets. Since particles that leave the domain in the x-direction are re-injected back into the chamber, these particles require a special type of boundary treatment: their concentrations and velocities are enforced according to the boundary conditions described in Fig. 6a using an approximation of non-reflexive boundary condition, known as sponge layer [66]. In this approach, we enforce the desired velocity and concentration fields of particles within the sponge zone using a smoothing function

$$\phi(x) = B \left(\frac{x - x_s}{x_e - x_s} \right)^n , (0 \leq x \leq x_e), \tag{2.36}$$

where x_s and x_e denote the start and end x-coordinate of the sponge zone, respectively. Parameters B and n are adjustment constants that affect the propagation speed for the absorbing boundary condition, taken here as $B = 1$ and $n = 3$. Thus, in the interval $0 \leq x \leq x_e$, the velocity and concentration of particle i crossing the upper inlet region change smoothly to target values $\boldsymbol{v}_{\text{target}} = \boldsymbol{v}_{in}$ and $C_{\text{target}} = C_L$

$$\boldsymbol{v}_i \leftarrow \boldsymbol{v}_i - (\boldsymbol{v}_i - \boldsymbol{v}_{\text{target}})\phi(x_i), \tag{2.37}$$

$$C_i \leftarrow \boldsymbol{C}_i - (\boldsymbol{C}_i - \boldsymbol{C}_{\text{target}})\phi(x_i), \tag{2.38}$$

thus approximating the flow inlet condition depicted in Fig. 6a in the main text.

2.4.5 Application: micro-channel reactive flow past a cell

We apply our methodology to perform a challenging simulation of biological significance representing a reactive micro-channel flow past a yeast cell that combines advection, diffusion, and reaction. The typical experiment, depicted schematically in Fig. 2.6a, consists of a microfluidics chamber with cells immersed in a liquid working media. The system, initially at rest, starts to experience mixing when at $t > 0$ two different fluids start to flow along the channel from different inlets. A solution containing working fluid and a diluted species (the mating pheromone alpha-factor, denoted by L) is released through one of the inlets, while through the other inlet, working fluid alone is injected into the system. Figure 2.5 shows a diagram of the microfludic Y-chamber that our simulation recapitulates.
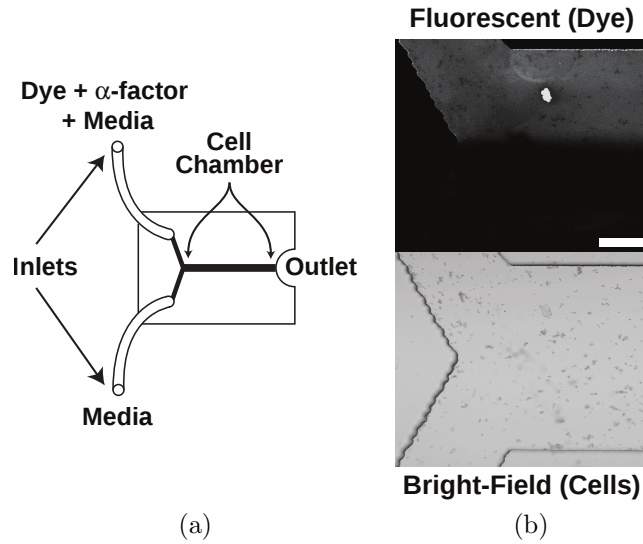
Figure 2.5: (a) Schematic diagram of microfluidics Y-chamber. (b) Images of device at inlet junction with cell chamber. Image of the fluorescent dye Dextran3000-TRITC, a tracer for the pheromone α-factor, as it flows from left to right and diffuses from top to bottom (top right). Bright-field image of cells attached to floor of the cell chamber subjected to the flow and pheromone gradient (bottom right). Scale bar = 20 μm.

As the flow develops, L reacts with the alpha-factor receptor R located at the cell surface, producing a third species, RL (receptor bound to ligand). We assume that the association reaction, $R + L \rightarrow RL$ occurs at a rate $k_{RL}[R][L]$. Similarly, the dissociation reaction $RL \rightarrow R + L$ also takes place in the system, and occurs at a rate $k_{RLm}[RL]$.

A general deterministic mathematical model that describes the system is given by Eqs. (3.1)-(3.3) which can be conveniently written in a non-dimensional form. The reference parameters, evaluated using the dimensional parameters described in Table 2.4, are given by:

Table 2.4: Dimensional parameters used in the micro-channel numerical experiment.

Parameter	Description	Value
κ_L	α-factor (L) diffusivity	$347\,[\mu m^2/s]$
ν	kinematic viscosity	$10^{-6}\,[m^2/s]$
$C_L|_{x=0}$	L concentration at inlet	$1.0[mol/m^3]$
$C_R|_{\text{cell}}$	R concentration at cell wall	$1.0[mol/m^3]$
k_{RL}	kinetic association rate	$1.0[m^3/(mol \cdot s)]$
k_{RLm}	kinetic dissociation rate	$1.0\,[s^{-1}]$
D	diameter of the cell	$5.0\,[\mu m]$
H	channel height	$100.0\,[\mu m]$
L_{channel}	channel length	$200.0\,[\mu m]$
L_{cell}	streamwise cell position	$25.0\,[\mu m]$
l_{cell}	thickness of cell membrane	$1.0\,[\mu m]$
v_o	reference velocity	$2.5 \times 10^{-4}\,[m/s]$
x_o	reference length	$H\,[m/s]$

mol/m^3 is the molar concentration.

$$x_o = H, \tag{2.39}$$

$$v_o = x_o/t_o, \tag{2.40}$$

$$C_o = C_L|_{x=0}, \tag{2.41}$$

$$P_o = \rho_o v_o^2, \tag{2.42}$$

where $H, C_L|_{x=0}$ and ρ_o are respectively the channel height, the concentration of alpha-factor at the inlet, and a reference density, considered here as unity. Using these dimensionless groups, Eqs. (3.1)-(3.3) are written as

$$\frac{\partial \rho^*}{\partial t^*} = -\rho^* \boldsymbol{\nabla}^* \cdot \boldsymbol{v}^*, \tag{2.43}$$

$$\frac{\partial \boldsymbol{v}^*}{\partial t^*} = -\frac{1}{\rho^*} \boldsymbol{\nabla}^* p^* + \frac{1}{Re} \nabla^2 \boldsymbol{v}^*, \tag{2.44}$$

$$\frac{\partial}{\partial t} \begin{bmatrix} C_R^* \\ C_L^* \\ C_{RL}^* \end{bmatrix} = \frac{1}{Pe} \nabla^{*2} \begin{bmatrix} C_R^* \\ C_L^* \\ C_{RL}^* \end{bmatrix} + \begin{bmatrix} R_R^* \\ R_L^* \\ R_{RL}^* \end{bmatrix}, \tag{2.45}$$

where R_A^*, R_B^* and R_C^* are given by the law of mass action as

$$\begin{bmatrix} R_R^* \\ R_L^* \\ R_{RL}^* \end{bmatrix} = \begin{bmatrix} -1 & 1 \\ -1 & 1 \\ 1 & -1 \end{bmatrix} \begin{bmatrix} C_R^* C_L^* & 0 \\ 0 & C_{RL}^* \end{bmatrix} \begin{bmatrix} Da_{\mathrm{I}}/Pe \\ Da_{\mathrm{II}}/Pe \end{bmatrix}. \tag{2.46}$$

The system now depends only on four dimensionless groups: $Da_{\mathrm{I}}, Da_{\mathrm{II}}, Pe$ and Re. In the present work, we define these quantities as

$$Da_{\mathrm{I}} = \frac{\tau_{\mathrm{diff}}}{\tau_{\mathrm{reactI}}} = \frac{x_o^2 k_{RL} C_o}{\kappa_L}, \tag{2.47}$$

$$Da_{\mathrm{II}} = \frac{\tau_{\mathrm{diff}}}{\tau_{\mathrm{reactII}}} = \frac{x_o^2 k_{RLm}}{\kappa_L}, \tag{2.48}$$

$$Pe = \frac{x_o v_o}{\kappa_L}, \tag{2.49}$$

$$Re = \frac{x_o v_o}{\nu}. \tag{2.50}$$

The first and second Damköhler numbers, denoted by $Da_{\mathrm{I}}, Da_{\mathrm{II}}$, are defined as the ratio between an arbitrary mixing time scale τ_{mix} and the chemical time scale of a n-

40

th order reaction τ_{react}. It is important to highlight that the mixing scale is problem-dependent; for combustion-dominated flows, the mixing scale is related to the turbulent time scale [67, 68], whereas in diffusion-dominant problems, the mixing scale is related to the molecular diffusion time scale [69, 70, 71, 72].

Table 2.5: Dimensionless groups used in the numerical experiment.

Group	Description	Value
Da_{I}	first Damköhler number	28.82
Da_{II}	second Damköhler number	28.82
Pe	mass Péclet number	72.06
Re	Reynolds number	2.5×10^{-2}

The mass Péclet number, denoted by Pe, describes the ratio of advection and molecular diffusion transport [71, 73]. Similarly, the Reynolds number Re describes the ratio of inertial to viscous transport in the flow[73].

The problem was solved using three different approaches: the present method, i.e., hybrid sSSA-SDPD, SDPD, and the finite element method (FEM). All of the cases were computed using the parameters described in Tables 2.4-2.5. Both hybrid sSSA-SDPD and SDPD simulations were performed using $N = 1250$ particles. The number of molecules per particle was taken as $N_m = 1600$. Note that because of the low level of parallelism of the SSA algorithm, simulations of the hybrid method must run in serial, which restricts the maximum number of particles involved in the simulation, as well as the number of realizations. As an example, we show only one SSA realization. The finite element problem was modeled using the software Comsol Multiphysics (v5.2a), using second-order shape functions in a mesh of approximately 17000 elements. Equations (2.44)-(2.45) were solved assuming incompressibility.

A qualitative comparison between the concentration of alpha-factor, C_L, is depicted in Fig. 2.6b. At time $t^* = 2$, the results show qualitative agreement. A mixing layer
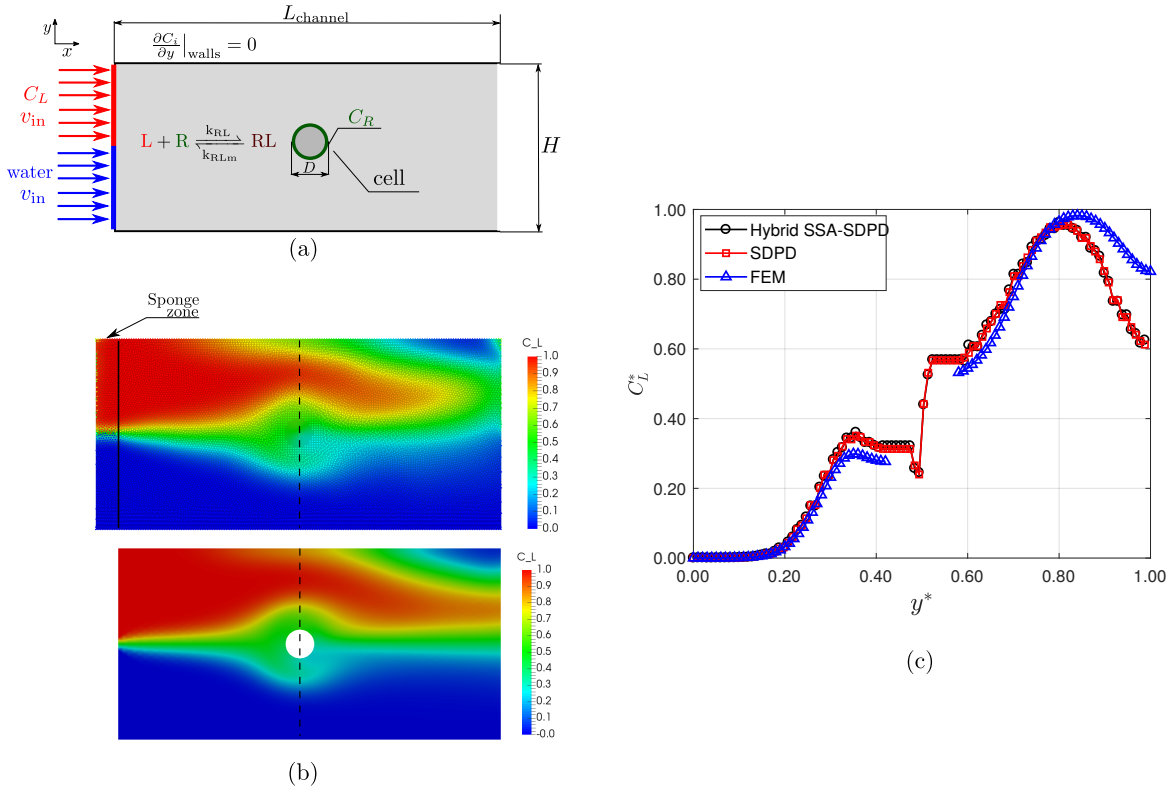
Figure 2.6: (a) Upper: schematic of our model of a yeast cell in a microfluidics channel flow containing a pheromone gradient. The working fluid is initially at rest, and at time $t > 0$, two inlets start to inject fluid into the chamber; the upper inlet consists of a diluted mixture of working fluid and alpha-factor L, and the lower inlet injects working fluid into the system. (a) Lower: magnified region around the cell, illustrating the particles and their initial velocities. (b) Contour plots of the dimensionless velocity magnitude field, $|\boldsymbol{v}^*|$, at $t^* = 2$, obtained using the proposed hybrid method (upper) and FEM (lower). (c) Comparison of the dimensionless concentration profiles of alpha-factor, C_L^*, between hybrid sSSA-SDPD, SDPD and finite element method (FEM), measured across the y^* centerline, at time $t^* = 2$. Results shown in (b) were interpolated using a Gaussian kernel, for clarity purposes.

is formed in the first half of the channel, with the hybrid method showing a delay in the frontal concentration when compared with FEM solution, indicating differences in the velocity field. As the flow contours around the cell, the mixing layer is interrupted, causing a separation of the concentration field into two fronts.

Figure 2.6c provides a quantitative comparison between the algorithms. The y^*-centerline profiles of C^*_{RL} shown in Fig. 2.6c demonstrate that despite its low resolution, the hybrid method still captured the physics of the problem. Note that the curves are in phase with each other. Still in Fig. 2.6c, it is noticeable that the results are in far better agreement with the FEM in the regions that are away from the boundaries. A possible cause of this discrepancy originates from the way non-slip boundary conditions are imposed. For simplicity, in this example, the cell was modeled using stationary particles, which may introduce errors due to the boundary curvature [74]. In particular, the usage of more sophisticated boundary treatments has shown to be effective in improving stability and accuracy of simulations [74, 75].

Finally, a comparison of the formation of species RL in the cell wall region for all three methods is shown in Fig. 2.7. This figure illustrates that SSA results can significantly differ from those of SDPD and FEM, depending on the species concentrations involved and the number of realizations performed. The explanation of the differences between the hybrid sSSA-SDPD method and the FEM results depend on how significant the stochastic effects are, and how well the PDEs used in FEM and the SDEs of SDPD can describe the reaction-diffusion process.

The discrepancies observed in Fig. 2.7 illustrate a case where the stochastic effects are relevant enough that deterministic methods can no longer predict the physics of the problem. Furthermore, this typical biological problem shows that it is not always obvious when stochastic effects will be significant, as the continuum hypothesis might hold true for momentum transport but not for reactive mass transfer. The proposed

hybrid method, however, allows for the correct representation of the physics of this class of problems. In particular, the method bridges the gap between stochastic and deterministic advection-diffusion-reaction systems in cell biology. In summary, the hybrid sSSA-SDPD method enables the simulation of systems spanning a large range of Knudsen numbers, without any *ad hoc* assumption about the Knudsen number or the relevance of stochastic transport.
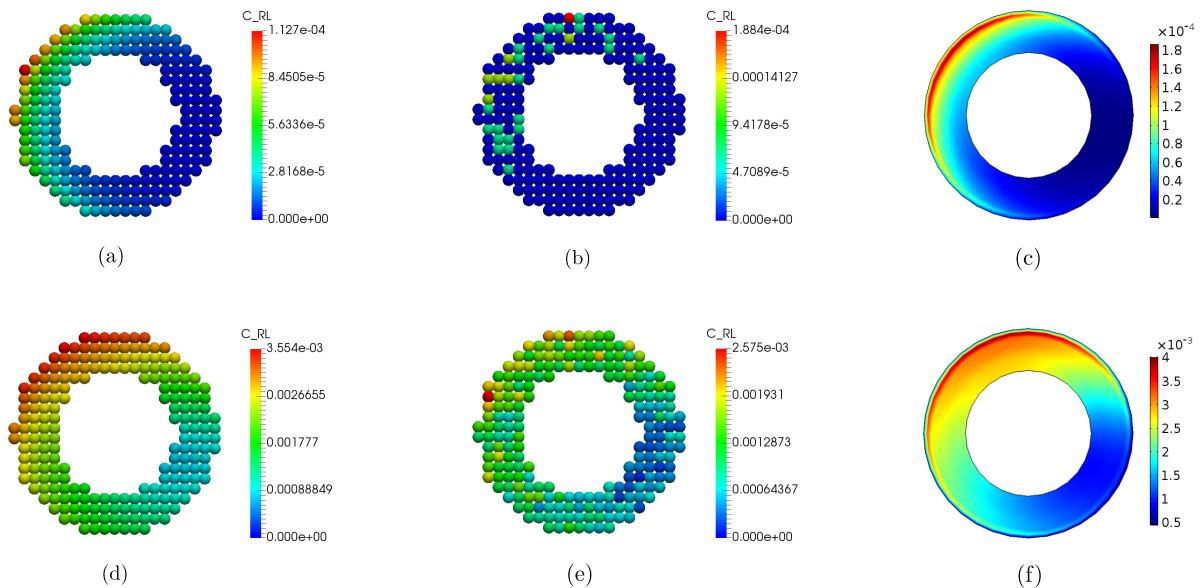

Figure 2.7: Top: dimensionless concentration of species RL at the cell wall, C^*_{RL}, at $t^* = 1$ (equivalent to physical time $t = 0.4[s]$), obtained by: (a) SDPD, (b) hybrid sSSA-SDPD method and (c) finite element method. Bottom: dimensionless concentration of species RL at the cell wall, C^*_{RL}, at $t^* = 2$ (equivalent to physical time $t = 0.8[s]$), obtained by: (d) SDPD, (e) sSSA-SDPD method and (f) finite element method. Note that the deterministic SDPD simulations in (a) and (d) match closely the finite element results in (c) and (f). However, the sSSA-SDPD simulations in (b) and (e) are able to capture the discrete stochastic dynamics of this subcellular biological process.

Chapter 3

Resolving moving boundaries: an ALE-SPH method for fluid-structure interaction

3.1 Background

Smoothed particle hydrodynamics (SPH) is a meshless particle method based on a Lagrangian formulation [50], proposed independently by [2] and [3] as a method to simulate astrophysical problems. Since its development, SPH has been used in a wide range of applications, including colloidal suspensions [4, 5], nanofluidics [6], blood flow [7, 8], multiphase flows [9], polymer chains [10] and red blood cell deformations [76].

In contrast to grid-based methods, SPH uses a kernel estimation at Lagrangian points (particles) to approximate the partial differential equations (PDEs) that govern the system of interest. When compared with standard mesh-based methods such as finite element (FEM), finite difference (FDM) and finite volume (FVM), SPH offers attractive advantages. As a consequence of its Lagrangian description, advection is treated exactly,

allowing the simulation of arbitrary free-shear flow in systems with complex geometries without the need to use an adaptive mesh or interface tracking [11, 12]. Another important feature of the method is its inherent adaptivity, as particle attributes evolve according to their material time derivative [13]. More recently, the development of multi-resolution SPH brings the method closer to industrial applications by adaptively increasing the resolution by means of splitting particles in regions of interest, and coalescing particles in regions where lower resolutions suffices [14, 15, 16, 17, 18].

Despite all of these advantages, the treatment of solid wall boundaries in SPH remains a challenge. Recent studies [77, 78, 75, 56, 79, 80, 81, 82, 83, 84, 85] have demonstrated that despite several improvements, the development of a robust, efficient and accurate method capable of preventing particle penetration under no-slip and partial-slip conditions remains an open problem. In fact, some consider it to be one of the grand challenges for the advancement of SPH [86].

The work of [87] provides a comprehensive review of the available solid wall models, comparing the performance of the most widely-used strategies and highlighting their capabilities and drawbacks. They classify the different models of solid boundaries into three main groups: (i) semi-analytical, (ii) ghost particles and (iii) boundary force methods. In the semi-analytical approach [80], surface integrals must be approximated using the SPH formalism. A limitation of this class of methods is the complexity of the algorithm, as many modifications are necessary to help prevent particle penetration on the solid boundary. In the ghost particles approach [88], a set of fictitious particles are created in the wall in order to guarantee non-slip and prevent penetration. Despite being conceptually attractive, the treatment of complex geometries is not straightforward. Similarly challenging, the computational algorithm typically requires the creation/destruction of particles at specific wall positions at each time step, resulting in memory access overheads and additional communication in otherwise parallel tasks.

These limitations make the class of boundary force methods a simple and attractive alternative. As a common feature, these methods use pre-determined layers of particles to model boundaries. The variants in this class differ in the way velocity and density are communicated between wall and fluid particles. For example, in the method developed by [56], a Lennard-Jones boundary force is added to the momentum equation for particles in the neighborhood of the walls, in a similar manner as the forces used in the immersed boundary method [89]. This approach, despite its simplicity, is effective for a wide range of problems, provided that all the parameters of the boundary force are calibrated correctly.

In the work of [75], the pressure and velocity of boundary particles are computed using interpolation of the fluid field, thus implicitly enforcing the impermeability condition of rigid walls. Unlike the method of [56], this method does not require parameter calibration. In fact, the detailed study of [87] concluded that the method of [75] is overall the best method available. More recently, [90] obtained good results for an enhanced incompressible SPH method and a pressure-based, physically-derived boundary condition. Similarly, [91] obtained excellent results and nearly quadratic convergence by using stabilization techniques to achieve higher accuracy. However, both frameworks used the boundary condition proposed by [75] in which there is no mathematical guarantee that particle penetration is prevented.

Recently a new method, designed primarily for dissipative particle dynamics (DPD) systems, was proposed by [92]. This method introduces an indicator variable, which measures the boundary volume fraction (BVF) of particles near solid walls, and employs a predictor-corrector integration to prevent particle penetration. As a result, the fluid particles become autonomous to find wall surfaces in arbitrarily shaped objects, based solely on the coordinates of their neighboring particles. This method prevents particle penetration with minimal computational overhead by using a local formulation.

In this context we propose a new SPH formulation combining the BVF wall treatment with the transport-velocity discretization. The resulting method, named SPH-BVF, is versatile, accurate and allows the modeling of fixed and moving boundaries. In contrast to the method proposed in [75], the impermeability is explicitly enforced during the time integration, and no further correction of the pressure field is required. Furthermore, we improve the BVF method for the case of moving boundaries by using weighted interpolations of the solid particles to determine the wall velocity and accelerations, resulting in an algorithm capable of dealing with deforming boundaries. Finally, we introduce the reaction-diffusion equation in our formulation, extending the usage of the method to conjugate mass transport problems with moving boundaries, enabling simulations where boundary deformations are caused by reaction-diffusion events. This step is crucial in enabling SPH to simulate certain biological systems in which enzymatic reactions trigger processes that modify the boundary properties.

The main features of the SPH-BVF method include (a) algorithmic simplicity; (b) retaining the locality and intrinsic parallelism of the SPH method at the cost of a small overhead; (c) preventing the three major problems in standard SPH methods: particle penetration at the boundaries, tension instabilities and anisotropic structures. We demonstrate these capabilities and validate the proposed method using canonical examples and compare the results with the literature. Finally, we test the new method on a biomechanical cell wall polarization problem that incorporates multiple physics (species transport, solid and fluid mechanics), and thus could not be solved by existing SPH methods and remains challenging for advanced commercial multiphysics FEM tools.

This chapter is organized as follows: Section 3.2 briefly describes the transport-velocity SPH formulation. Section 3.3 provides the additional equations required for the SPH-BVF method and its algorithm. Sections 3.4 and 3.5 present validations, applications, and discussion of relevant results. Finally, conclusions and future perspectives

are discussed in Chapter 4.

3.2 SPH formulation

In this section we provide a brief overview of the governing equations, the SPH discretizations and the temporal integration method proposed.

3.2.1 Governing equations and transport-velocity formulation

The continuum mechanics equations for the conservation of mass, linear momentum and concentration of species in a Lagrangian reference frame are given by

$$\frac{d\rho}{dt} = -\rho \boldsymbol{\nabla} \cdot \boldsymbol{v}, \tag{3.1}$$

$$\frac{d\boldsymbol{v}}{dt} = \frac{1}{\rho} \boldsymbol{\nabla} \cdot \boldsymbol{\sigma} + \boldsymbol{F}_{\mathrm{B}}, \tag{3.2}$$

$$\frac{dC}{dt} = \boldsymbol{\nabla} \cdot (\alpha \boldsymbol{\nabla} C) + R, \tag{3.3}$$

where ρ, $\boldsymbol{v}$, $\boldsymbol{\sigma}$, $\boldsymbol{F}_{\mathrm{B}}$, C, α and R denote the fluid density, velocity, Cauchy stress tensor, body force, concentration, mass diffusivity and reaction term, respectively. The $d(\cdot)/dt$ operator denotes the material derivative [48].

One of the most relevant problems of standard, purely Lagrangian SPH discretizations of Eqs. (3.1)-(3.3) is the onset of anisotropic particle structures formed as the particles follow the Lagrangian trajectories. This problem was first addressed in [93] by introducing the concept of particle shifting, where a small perturbation is applied to the particle trajectories, reducing the formation of anisotropic structures. Later, the work of [94] applied particle shifting to a weakly compressible SPH formulation, obtaining improved

results in fluid flow problems. More recent improvements include the usage of particle shifting in free surface flows for incompressible SPH formulations [53], and stabilized particle shifting techniques [95]. [96] clarified that this issue is particularly relevant in fluid flows in which there is a natural tendency of particle alignment, such as flows subject to stretching and shear stresses. A similarly relevant problem is the so-called tensile instability, a phenomenon that causes particles to clump when subject to a tension stress state [58], being particularly relevant in fluid-structure interactions, solids under large deformations and flows under high Reynolds numbers. Incidentally, both of these limiting issues are alleviated by using the transport-velocity formulation, proposed by [75] for fluids and later extended to solid mechanics by [97]. The transport-velocity formulation consists of a particular type of Arbitrary Lagrangian Eulerian (ALE) formalism [96], where particles are advected by an arbitrary transport velocity, specifically tuned so that the pressure field is kept positive, thus avoiding the tensile instability, while at the same time it causes a small shift in the particle trajectories, avoiding the formation of coherent structures of particles. For a detailed numerical analysis of the transport-velocity SPH formulation, we refer the reader to [98].

The transport-velocity equations are obtained by rewriting the material derivative operator for a particle moving with a modified advection velocity $\tilde{\boldsymbol{v}}$ as

$$\frac{\tilde{d}(\bullet)}{dt} = \frac{\partial(\bullet)}{\partial t} + \tilde{\boldsymbol{v}} \cdot \boldsymbol{\nabla}(\bullet). \tag{3.4}$$

The presence of the modified transport velocity, $\tilde{\boldsymbol{v}}$, modifies the material derivative operator with two relative velocity terms, leading to the following identity

$$\frac{d(\bullet)}{dt} = \frac{\tilde{d}(\bullet)}{dt} + \boldsymbol{\nabla} \cdot [(\bullet)(\boldsymbol{v} - \tilde{\boldsymbol{v}})] - (\bullet)\boldsymbol{\nabla} \cdot (\boldsymbol{v} - \tilde{\boldsymbol{v}}), \tag{3.5}$$

where, due to the weakly compressible approximation [11, 97], it is safe to assume that

50

$\boldsymbol{\nabla} \cdot (\boldsymbol{v} - \tilde{\boldsymbol{v}}) \approx 0$. Thus, the transport-velocity formulation of the conservation laws, Eqs. (3.1)-(3.3), yields

$$\frac{\tilde{d}\rho}{dt} = -\rho \boldsymbol{\nabla} \cdot \boldsymbol{v} - \boldsymbol{\nabla} \cdot [\rho(\boldsymbol{v} - \tilde{\boldsymbol{v}})] , \tag{3.6}$$

$$\frac{\tilde{d}\boldsymbol{v}}{dt} = \frac{1}{\rho} \boldsymbol{\nabla}\boldsymbol{\sigma} + \boldsymbol{F}_{\mathrm{B}} - \boldsymbol{\nabla} \cdot [\boldsymbol{v}(\boldsymbol{v} - \tilde{\boldsymbol{v}})] , \tag{3.7}$$

$$\frac{\tilde{d}C}{dt} = \boldsymbol{\nabla} \cdot (\alpha \boldsymbol{\nabla} C) + R - \boldsymbol{\nabla} \cdot [C(\boldsymbol{v} - \tilde{\boldsymbol{v}})] . \tag{3.8}$$

Equations (3.6)-(3.8) form the set of governing equations of the SPH-BVF formulation. Additional conservation laws can be added as needed, using the identity provided by Eq. (3.5). Notice that this formulation can be seen as a generic version of SPH schemes for an arbitrary reference frame [96], where $\tilde{\boldsymbol{v}}$ is the referential velocity. For instance, if $\tilde{\boldsymbol{v}} = \boldsymbol{v}$, Eqs. (3.6)-(3.8) reduce to the classical, purely Lagrangian formulation. In contrast, setting $\tilde{\boldsymbol{v}} = 0$ results in a formulation for an inertial (Eulerian) reference frame. In the following sections, we discuss the usage of $\tilde{\boldsymbol{v}}$ and how this term is discretized.

3.2.2   SPH discretization

In SPH, the mapping between the primitive variables (mass, momentum and concentrations) and the discrete particle system is done using two different approximations: a radial basis function kernel interpolation and a quadrature approximation. The radial basis function kernel interpolation consists of approximating a continuous function $f : \mathbb{R}^3 \mapsto \mathbb{R}$, defined at coordinates $\boldsymbol{x}$ in $\Omega \subseteq \mathbb{R}^3$, by the integral equation with a smoothing kernel function W with compact support h

$$f(\boldsymbol{x}) \approx \int_{\Omega} f(\boldsymbol{x}')W(\boldsymbol{x} - \boldsymbol{x}', h)d\boldsymbol{x}'. \tag{3.9}$$

The accuracy of the approximation in Eq. (3.9) depends on the choice of W. For the sake of simplicity, we have adopted in this work the Lucy kernel, proposed by Lucy [3], with $\boldsymbol{x}_{ij} = \boldsymbol{x} - \boldsymbol{x}'$ and $\xi = ||\boldsymbol{x}_{ij}||_2/h$ denoting a generalized coordinate

$$W(\xi) = \begin{cases} \alpha_D \left(1 + 3\xi\right)\left(1 - \xi\right)^3, & \text{if } 0 \leq \xi \leq 1, \\ 0, & \text{otherwise,} \end{cases} \tag{3.10}$$

and the spatial derivative

$$\boldsymbol{\nabla} W = \frac{\boldsymbol{x}}{x}\frac{dW}{d\xi}, \tag{3.11}$$

where the normalization parameter α_D depends on the dimensionality of the problem:

$$\alpha_D = \begin{cases} 5/4h, & \text{if 1D,} \\ 5/\pi h^2, & \text{if 2D,} \\ 105/16\pi h^3, & \text{if 3D.} \end{cases} \tag{3.12}$$

For details on choosing W, the reader may refer to the work of [12]. The second approximation consists of rewriting the integral given by Eq. (3.9) as a discrete sum. The domain Ω is then discretized using N particles, each located at coordinates $\boldsymbol{x}_i$. The kernel approximations of f and $\boldsymbol{\nabla} f$ are given by

$$f_i \approx \sum_{j=1}^{N} \frac{m_j}{\rho_j} f_j W_{ij}, \tag{3.13}$$

$$\boldsymbol{\nabla} f_i \approx \sum_{j=1}^{N} \frac{m_j}{\rho_j}(f_j \pm f_i)\boldsymbol{\nabla} W_{ij}, \tag{3.14}$$

where m_j/ρ_j, $\langle f \rangle_i$ and $\langle \boldsymbol{\nabla} f \rangle_i$ denote the number density (weight) of particle j, the kernel approximations of the field $f(\boldsymbol{x})$ and its gradient at position $\boldsymbol{x}_i$, respectively.

3.2.3 Stress description of solids and fluids

Equations (3.1)-(3.3) allow a common description of fluid and solid dynamics within the same framework [97]. This facilitates the treatment of multiple materials in complex physical problems, such as biological systems and multiphase flows. Different materials can then be modeled using different constitutive relations for the Cauchy stress tensor $\boldsymbol{\sigma}$. For validation purposes, we use two types of materials: linear elastic solids and Newtonian fluids. Thus,

$$\boldsymbol{\sigma} = \begin{cases} -P\boldsymbol{I} + \boldsymbol{S}, & \text{for solids} \\[2mm] -P\boldsymbol{I} + 2\eta\boldsymbol{\epsilon}, & \text{for fluids,} \end{cases} \tag{3.15}$$

where P, η are the pressure and viscosity, and $\boldsymbol{S}, \boldsymbol{\epsilon}, \boldsymbol{I}$ denote the deviatoric stress, strain and second-order identity tensors, respectively. Assuming Hooke's law, the Jaumann rate of the deviatoric stress tensor $\boldsymbol{S}$ is given by [58]

$$\frac{d\boldsymbol{S}}{dt} = 2G\left[\boldsymbol{\epsilon} - \frac{1}{3}\text{Tr}(\boldsymbol{\epsilon})\boldsymbol{I}\right] + \boldsymbol{S} \cdot \boldsymbol{\omega}^T + \boldsymbol{\omega} \cdot \boldsymbol{S}, \tag{3.16}$$

where G is the shear modulus and $\boldsymbol{\omega}$ is the rotation tensor. The kernel approximations are used to discretize the spatial derivatives and primitive variables in the governing equations, Eqs. (3.1)-(3.3). The resulting system of equations is given by

$$\frac{d\rho_i}{dt} = \rho_i \sum_j \frac{m_j}{\rho_j} \boldsymbol{\nabla} W_{ij} \cdot \boldsymbol{v}_{ij} \tag{3.17}$$

$$- \sum_j \frac{m_j}{\rho_j} \boldsymbol{\nabla} W_{ij} \cdot \left[\rho_i(\boldsymbol{v}_i - \tilde{\boldsymbol{v}}_i) + \rho_j(\boldsymbol{v}_j - \tilde{\boldsymbol{v}}_j) \right],$$

$$\frac{d\boldsymbol{v_i}}{dt} = -\sum_j m_j \boldsymbol{\nabla} W_{ij} \cdot \tag{3.18}$$

$$\cdot \left[\left(\frac{\boldsymbol{\sigma}_i}{\rho_i^2} + \frac{\boldsymbol{\sigma}_j}{\rho_j^2} \right) - \left(\frac{\mathbf{A}_i}{\rho_i^2} + \frac{\mathbf{A}_j}{\rho_j^2} \right) \right]$$

$$+ \sum_j m_j \frac{\mu_{ij}}{\rho_i \rho_j (x_{ij}^2 + \epsilon h^2)} \boldsymbol{\nabla} W_{ij} \cdot \boldsymbol{v}_{ij},$$

$$\frac{dC_i}{dt} = \sum_j m_j \frac{\alpha_{ij}(C_j - C_i)}{\rho_i \rho_j (x_{ij}^2 + \epsilon h^2)} \boldsymbol{\nabla} W_{ij} \cdot \boldsymbol{x}_{ij} \tag{3.19}$$

$$- \sum_j \frac{m_j}{\rho_j} \boldsymbol{\nabla} W_{ij} \cdot \left[C_i(\boldsymbol{v}_i - \tilde{\boldsymbol{v}}_i) + C_j(\boldsymbol{v}_j - \tilde{\boldsymbol{v}}_j) \right],$$

$$\frac{dS_i}{dt} = 2G \left[\boldsymbol{\epsilon}_i - \frac{1}{3} Tr(\boldsymbol{\epsilon}_i) \boldsymbol{I} \right] + \boldsymbol{S}_i \cdot \boldsymbol{\omega}_i^T \tag{3.20}$$

$$+ \boldsymbol{\omega}_i \cdot \boldsymbol{S}_i,$$

where the strain and rotation tensors for each particle i in Eq. (3.20) are given by

$$\boldsymbol{\epsilon}_i = \sum_j \frac{m_j}{2\rho_j} \left[\boldsymbol{v}_{ij} \otimes \boldsymbol{\nabla} W_{ij} + (\boldsymbol{v}_{ij} \otimes \boldsymbol{\nabla} W_{ij})^T \right], \tag{3.21}$$

$$\boldsymbol{\omega}_i = \sum_j \frac{m_j}{2\rho_j} \left[\boldsymbol{v}_{ij} \otimes \boldsymbol{\nabla} W_{ij} - (\boldsymbol{v}_{ij} \otimes \boldsymbol{\nabla} W_{ij})^T \right], \tag{3.22}$$

and the summations are performed over all neighboring particles of particle i that are within the compact support of W, and $\boldsymbol{v}_{ij} = \boldsymbol{v}_i - \boldsymbol{v}_j$. The term $\mathbf{A} = \rho \boldsymbol{v}(\boldsymbol{v} - \tilde{\boldsymbol{v}})$ denotes the relative velocity tensor. The shear viscosity and mass diffusion coefficients are averaged as $\mu_{ij} = 2\mu_i \mu_j/(\mu_i + \mu_j)$ and $\alpha_{ij} = 2\alpha_i \alpha_j/(\alpha_i + \alpha_j)$. A small constant $\epsilon = 0.01$ is added

to the denominators of Eqs. (3.18)-(3.19) to prevent singularities.

The second summation in Eq. (3.18), introduced by [74], improves the stability of the numerical method by acting as a diffusive term, while modeling the viscous force $\boldsymbol{F}_\mathrm{V}$, in a similar manner as the Von Neumann & Richtmyer's artificial viscosity term used in most standard SPH formulations [2, 99, 55], and has been used even for elastic solids [58]. In the present work, we have adopted the artificial viscosity formulation, but it is important to emphasize that the artificial viscosity term Eq.(3.18) is still an active area of research, and to a certain extent and despite being widely used in the classic SPH literature, its application makes the method case-dependent. A promising alternative to the artificial term consists in reformulating the SPH convolution integrals by introducing only the sufficient amount of dissipation by means of using a non-linear Riemann problem; this technique, named Godunov SPH (GSPH), is known for achieving very low advection and angular momentum conservation errors and no excessive diffusion, without the need for tuning artificial viscosity terms [100, 101, 102].

The model described by Eqs. (3.17)-(3.19) is closed by a relationship between the density and pressure field. For fluids, two different approaches are widely used in the literature, namely: 1) treat the flow as incompressible, either by solving a pressure-Poisson equation to obtain a divergence-free velocity field [52, 53], or by requiring as a kinematic constraint that the volume of the fluid particles is constant [54]; or 2) treat it as weakly compressible, and impose an equation of state [55, 31, 56, 75, 11, 12, 97]. We follow the weakly compressible formulation, with an equation of state of the form

$$ P = P_0 \left[\left(\frac{\rho}{\rho_0} \right)^{\gamma} - 1 \right], \tag{3.23} $$

where P_0, ρ_0 denote reference pressure and density, respectively, and γ is the polytropic constant. It is a common practice [56, 12] to select $P_0 = K = \rho_0 c_0^2 / \gamma$, where c_0 is

the artificial speed of sound and K is the compressibility modulus of the material. In order to limit density variations and prevent excessive spurious pressure waves [11], we choose $\gamma = 1$. Here, c_0 is chosen based on the desired Mach number, Ma, and the characteristic velocity of the problem U_c. For problems involving liquids, a typical choice is to use $Ma = 0.1$ to reduce compressibility effects, and thus $c_0 = 10\,U_c$. For solids, previous works [58, 103, 97] have used the same formulation ($P_0 = \rho_0 c_0^2/\gamma$), in which the sound speed of the solid is computed using the shear modulus G and Poisson ratio of the material, ν_p, as $c_0 = \sqrt{2G(1 - \nu_p)/\rho_0}$.

In addition, for solid particles, we suggest the addition of an artificial stress term to Eq. (3.18), as described by [58], as we found that the transport-velocity formulation was not capable of removing the tensile instability in solids completely without introducing excessive particle distortion.

3.2.4   Defining the transport velocity

The transport-velocity formulation introduces the velocity of the reference frame, $\tilde{v}$, into Eqs. (3.6)-(3.8). This arbitrary velocity determines the nature of the reference frame, adjusting the conservation laws to an Eulerian, Lagrangian or any arbitrary mode in between these descriptions, therefore providing a arbitrary Lagrangian Eulerian (ALE) formalism to SPH [96].

We adopt the transport velocity correction term [75] as our arbitrary velocity, which has the form of a background pressure gradient

$$\tilde{v}(t + \Delta t) = v(t) + \Delta t \left(\frac{\tilde{d}v}{dt} - \frac{1}{\rho} \boldsymbol{\nabla} P_b \right), \tag{3.24}$$

where the background pressure gradient is discretized as

$$\boldsymbol{f}_{\mathrm{PB}} = \left(\frac{1}{\rho}\boldsymbol{\nabla}P_b\right)_i \approx P_b \sum_j \frac{m_j}{\rho_i^2}\boldsymbol{\nabla}W_{ij} \tag{3.25}$$

and P_b is chosen as the reference pressure, P_0. This choice is justified by the additional benefit that this term acts as a self-relaxation mechanism [98] in the linear momentum equation by balancing the actual hydrodynamic pressure gradient $\boldsymbol{\nabla}P/\rho$ term, therefore reducing the tension instability in the flow and greatly improving the overall accuracy of the method.

3.2.5   Switch correction for pressure and filter

For fluid flows subject to large Reynolds numbers or shear effects, it has been reported that the usage of the continuity equation, Eq. (3.17) may result in errors and spurious pressure waves that deteriorate the accuracy of the numerical solution [104, 97]. In order to overcome this issue, [11] proposed the computation of the density via interpolation, which conserves mass exactly. Although these two formulations are mathematically equivalent [55], it has been shown that the usage of the continuity equation within an ALE framework results in smoother density fields [96]. However, experiments reported by [105] have shown that the pressure can still attain negative values, causing instabilities and numerical cavitation.

We propose the solution of the continuity equation, along with the usage of a pressure switch to address the numerical cavitation problem, which filters negative pressures. Both the filter and the switch are used only for fluid particles, as negative pressures are required for compressive stress in solids. A similar procedure was proposed by [105]. This simple correction is based on the identity

$$\sum_j m_j \boldsymbol{\nabla} W_{ij} \cdot \left(\frac{P_i}{\rho_i^2} + \frac{P_j}{\rho_j^2} \right) \mathbf{I} = \tag{3.26}$$

$$\sum_j m_j \boldsymbol{\nabla} W_{ij} \cdot \left(\frac{P_j}{\rho_j^2} - \frac{P_i}{\rho_i^2} \right) \mathbf{I} + 2 \frac{P_i}{\rho_i^2} \sum_j m_j \boldsymbol{\nabla} W_{ij} \cdot \mathbf{I}$$

and proceeds by dropping the second sum in Eq. (3.26) if the pressure is negative, i.e.,

$$\left(\frac{1}{\rho} \boldsymbol{\nabla} P \right)_i = \begin{cases} \sum_j m_j \boldsymbol{\nabla} W_{ij} \cdot P_{ij}^+ \mathbf{I}, & \text{if } P_{ij}^+ \geq 0 \\ \sum_j m_j \boldsymbol{\nabla} W_{ij} \cdot P_{ij}^- \mathbf{I}, & \text{else,} \end{cases} \tag{3.27}$$

where the pairwise pressures P_{ij}^+ and P_{ij}^- are computed as

$$P_{ij}^+ = \left(\frac{P_j}{\rho_j^2} + \frac{P_i}{\rho_i^2} \right), \tag{3.28}$$

$$P_{ij}^- = \left(\frac{P_j}{\rho_j^2} - \frac{P_i}{\rho_i^2} \right). \tag{3.29}$$

Finally, in order to damp high-frequency pressure waves and improve energy conservation, we use a Shepard filter in the density field every N_f timesteps [106]

$$\rho_i = \frac{\sum_j m_j W_{ij}}{\sum_j \frac{m_j}{\rho_j} W_{ij}}, \tag{3.30}$$

where the optimal frequency for filtering, $N_f = 20$, as reported by [104], was used.

3.2.6   Temporal integration

Following the practice of several authors [58, 51, 11], the integration of Eqs. (3.17)-(3.20) was performed using a modified velocity-Verlet scheme. For the density and con-

centration fields, we have adopted an explicit midpoint method. Specifically, considering $\boldsymbol{v}_i, \boldsymbol{x}_i, \rho_i, C_i, \boldsymbol{S}_i$ the unknowns of the system, and $f_\rho, \boldsymbol{f}_v, f_C, f_{\boldsymbol{S}}$ the right-hand sides of Eqs. (3.17)-(3.20), respectively, the proposed numerical integration is given by

Step 1

    (a) Initial half-steps

$$\rho^{n+1/2} = \rho^n + \frac{\Delta t}{2} f_\rho^{n-1/2}, \tag{3.31}$$

$$\boldsymbol{v}^{n+1/2} = \boldsymbol{v}^n + \frac{\Delta t}{2} \boldsymbol{f}_v^{n-1/2}, \tag{3.32}$$

$$\tilde{\boldsymbol{v}}^{n+1/2} = \boldsymbol{v}^{n+1/2} + \frac{\Delta t}{2} \boldsymbol{f}_{\mathrm{PB}}^{n-1/2}, \tag{3.33}$$

$$C^{n+1/2} = C^n + \frac{\Delta t}{2} f_C^n, \tag{3.34}$$

$$\boldsymbol{S}^{n+1/2} = \boldsymbol{S}^n + \frac{\Delta t}{2} f_{\boldsymbol{S}}^n. \tag{3.35}$$

    (b) Position update

$$\boldsymbol{x}^{n+1} = \boldsymbol{x}^n + \Delta t \, \tilde{\boldsymbol{v}}^{n+1/2}. \tag{3.36}$$

Step 2

    (a) Final half-steps

$$\rho^{n+1} = \rho^n + \Delta t \, f_\rho^{n+1/2}, \tag{3.37}$$

$$\boldsymbol{v}^{n+1} = \boldsymbol{v}^{n+1/2} + \frac{\Delta t}{2} \boldsymbol{f}_v^{n+1/2} \tag{3.38}$$

$$C^{n+1} = C^n + \Delta t \, f_C^{n+1/2}, \tag{3.39}$$

$$\boldsymbol{S}^{n+1} = \boldsymbol{S}^n + \Delta t \, f_{\boldsymbol{S}}^{n+1/2}. \tag{3.40}$$

Although the method has two steps, notice that it requires the evaluation of the particle forces only once per time step. A necessary condition for stability, given by the Courant-Friedrichs-Lewy condition based on the artificial speed of sound c_0, was used to estimate a suitable time step Δt for each simulation [12]

$$\Delta t \leq C \min \left(\frac{h}{c_0 + |U_c|}, \frac{h^2 \rho}{\mu}, \sqrt{\frac{h}{g}} \right), \tag{3.41}$$

where g is the gravity acceleration, and a Courant number $C = 0.25$ was adopted.

3.3   Wall treatment: boundary volume fraction method

We start by considering a particle of fluid i, located at a weighted averaged distance d from the wall. As depicted in Fig. 3.1, the region of influence around particle i, denoted by Ω, has radius h. The shaded region represents the solid wall. We denote the intersection of wall and region Ω by S.
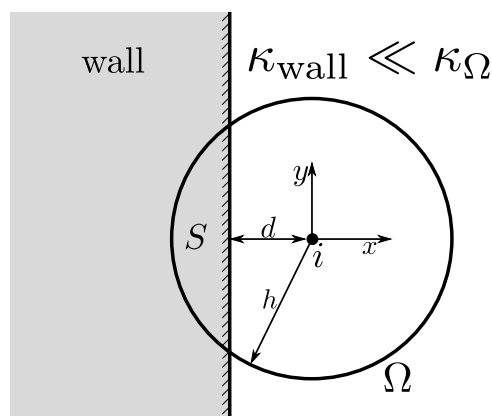
Figure 3.1:   Schematic showing the influence domain Ω around particle i, nearby wall and intersection between Ω and the wall, denoted by S.

We assume that the curvature of the wall, κ_{wall}, is far smaller than the curvature of Ω, κ_Ω. Following [92], we assign to particle i an extra variable, denoted by ϕ. We define

ϕ as the ratio between the volumes of regions S and Ω, i.e., the boundary volume fraction (BVF), given by

$$\phi := \frac{V^S}{V^\Omega}. \tag{3.42}$$

Notice that, for $d = 0$, particle i is located exactly at the wall, thus $\phi = 0.5$. This allows us to use the variable ϕ to act as an indicator function of how close a particle is from the solid wall. It is important to highlight that the boundary volume fraction interface cutoff of 0.5 makes sense only within a predictor-corrector temporal integration scheme, as the theoretical value of $\phi = 0.5$ at the interface is never met due to numerical precision. Thus, the particle will have its trajectory corrected (in the corrector step) only when it reaches the wall (in the predictor step). Nevertheless, pairwise and viscous effects of the wall particles remain in effect within the cutoff of the kernel function adopted, as in other SPH methods.

Assuming that both the wall and the support domain Ω have sufficient particles, we can approximate the volumes of regions S and Ω in Eq. (3.42) using the SPH formalism

$$V_i^S = \sum_{j \in S} \frac{m_j}{\rho_j} V_j W_{ij} = \sum_{j \in S} \left(\frac{m_j}{\rho_j}\right)^2 W_{ij}, \tag{3.43}$$

$$V_i^\Omega = \sum_{j \in \Omega} \frac{m_j}{\rho_j} V_j W_{ij} = \sum_{j \in \Omega} \left(\frac{m_j}{\rho_j}\right)^2 W_{ij}, \tag{3.44}$$

where Ω is the total set of particles, and S is the subset of solid particles. Thus, the BVF of particle i, ϕ_i, written in terms of SPH formalism is given by

$$\phi_i = \frac{\sum_{j \in S} \left(\frac{m_j}{\rho_j}\right)^2 W_{ij}}{\sum_{j \in \Omega} \left(\frac{m_j}{\rho_j}\right)^2 W_{ij}}. \tag{3.45}$$

61

Compared to the standard SPH algorithm, the only major modification regarding the wall treatment in the SPH-BVF method is that the numerical integration of Eqs. (3.1)-(3.3) now includes an additional constraint: the following correction is performed in the velocity field of particle i if $\phi_i \geq 0.5$, i.e., if particle i penetrates the wall, we correct the velocity of particle i by reassigning its velocity to the value calculated using the bounce-back equation proposed by [92]

$$\boldsymbol{v}_i^{\text{corrected}} = 2\boldsymbol{v}_i^{\text{wall}} + \Delta t \boldsymbol{a}_i^{\text{wall}} - \boldsymbol{v}_i + 2\max(0, \boldsymbol{v_i} \cdot \boldsymbol{e}_i^n)\boldsymbol{e}_i^n, \qquad (3.46)$$

where $\boldsymbol{e}^n = \boldsymbol{n}^w / n^w$ denotes the unit normal vector pointing outward from the wall boundary, Δt is the time step and $\boldsymbol{v}^{\text{wall}}$, $\boldsymbol{a}^{\text{wall}}$ are the local velocity and acceleration of the boundary, respectively. This equation results from the collision of two particles of arbitrary masses as described in [107] in the limit case where one particle possesses much greater mass $(m_1 \gg m_2)$ so that the inertial effects on the larger particle are negligible compared to the smaller particle bouncing-back. Because the collision is considered elastic, the conservation of energy is preserved. The normal vector for particle i, $\boldsymbol{n}_i^w$, is given by the gradient of ϕ_i:

$$\boldsymbol{n}_i^w = \frac{\sum_{j \in S} \left(\frac{m_j}{\rho_j}\right)^2 \nabla W_{ij}}{\sum_{j \in \Omega} \left(\frac{m_j}{\rho_j}\right)^2 W_{ij}}. \qquad (3.47)$$

We propose the usage of a kernel-interpolated velocity and acceleration of solid particles, i.e., for a fluid particle i, its solid neighbor moves with

$$\boldsymbol{v}_i^{\text{wall}} = \frac{\sum_{j \in S} \boldsymbol{v}_j \left(\frac{m_j}{\rho_j}\right)^2 W_{ij}}{\sum_{j \in S} \left(\frac{m_j}{\rho_j}\right)^2 W_{ij}}, \tag{3.48}$$

$$\boldsymbol{a}_i^{\text{wall}} = \frac{\sum_{j \in S} \boldsymbol{a}_j \left(\frac{m_j}{\rho_j}\right)^2 W_{ij}}{\sum_{j \in S} \left(\frac{m_j}{\rho_j}\right)^2 W_{ij}}, \tag{3.49}$$

where the summations in Eqs. (3.48)-(3.49) are over the solid wall particles in the support of particle i (S).

Algorithm 4 SPH-BVF method

Input: Given initial positions, velocities and concentrations of species for all particles i
   at time t: $\boldsymbol{x}_i, \boldsymbol{v}_i, C_i$, and integration timestep Δt.
Output: Positions, velocities and concentrations of species for all particles i at time
   $t + \Delta t$.
 1: Find forces, for all i:
 2: **for** all i **do**
 3:    Compute SPH approximations, Eqs. (3.17)-(3.19).
 4:    Compute ϕ_i, Eq. (3.45).
 5: **end for**
 6: Perform temporal integration, for all i:
 7: **for** all i **do**
 8:    **After** the modified velocity-Verlet final integration step (**Step 2**), perform BVF
   correction:
 9:    **if** $\phi_i \geq 0.5$ **then**
10:       $\boldsymbol{v}_i \leftarrow 2\boldsymbol{v}_i^{\text{wall}} + \Delta t \boldsymbol{a}_i^{\text{wall}} - \boldsymbol{v}_i + 2\max(0, \boldsymbol{v_i} \cdot \boldsymbol{e}_i^n)\boldsymbol{e}_i^n$
11:    **end if**
12: **end for**

Notice that the accuracy of the computation of the normal vector and the BVF is strictly dependent on having enough particles to accurately represent the walls. Thus, thin walls, regions of large curvature and large particle spacing among wall particles are some of the limitations of the BVF method. In practice, we have found that three layers of particles are typically enough to obtain accurate results, while slightly increasing

the computational load of the method. However, the overall computational cost for the present method must have the same order of magnitude as standard SPH, since the only algorithmic addition in SPH-BVF is computing the normals and the additional BVF field ϕ_i in Eq. (3.47), which can be performed in parallel with the evaluation of the pairwise forces, with the advantage that fluid particle penetration is explicitly avoided. A summary of the algorithm is provided in Algorithm 1.

3.4   Validation

In this section we validate the SPH-BVF method using several canonical examples. First, a Poiseuille flow simulation is used to validate and verify the convergence of the fluid flow solver and the BVF boundary conditions. In addition, the new method is tested for different kernels. In our second example we validate our method with the Taylor-Green vortex flow problem and compare the results with the standard SPH method, showing that the SPH-BVF method resolves the velocity decay accurately, without excessive diffusion. Next, a lid-driven cavity flow is used to validate the fluid flow solver and the BVF wall boundary conditions, which further validates our method over a wider range of Reynolds numbers and demonstrates that fluid particles do not penetrate through the walls. We validate the strong coupling of fluid flow and mass transport with a natural convection flow, emphasizing the elimination of tensile instabilities and particle alignments, and also demonstrating our method on curved walls. In our fifth example, we validate SPH-BVF for solid mechanics with an oscillating cantilever beam. This problem demonstrates the use of our method on a moving solid under tension, and further shows the elimination of tensile instability. Finally, we compare SPH-BVF with a finite element method using a fluid-structure interaction problem. This example also demonstrates our method in the context of sponge zones and flux boundary conditions.

3.4.1   Wall boundary condition validation: Poiseuille flow

We validate the proposed wall boundary condition method with a laminar, two dimensional Poiseuille flow in a closed channel as performed by [108]. The flow is driven by a constant volume force of magnitude $0.8\,[ms^{-2}]$, and periodic boundary conditions are imposed in the streamwise (x)-direction. The channel width is assumed to be $W = 1\,[m]$, where a fluid with viscosity $\nu = 10^{-1}\,[m^2 s^{-1}]$ flows with a resulting Reynolds number $Re = 10$. We have considered five different particle refinements, with $N_y = 20, 40, 80, 160$ and 320 particles in the cross-stream (y)-direction. In addition to the standard Lucy kernel given by Eq. (3.10), we have performed convergence studies using the cubic spline kernel [58] and the Wendland quintic kernel [109]. In all cases, the kernel cutoff is set to $h = 3\Delta p$, which for a support of diameter $2h$ results in approximately 28 neighbors, and Δp is the particle spacing.

For a fully-developed, steady-state flow, the analytical velocity profile of the flow in the streamwise direction, v_x^{a}, is given by

$$v_x^{\mathrm{a}}(y) = 4\,Re\,\nu\,\frac{y}{W^2}\left(1 - \frac{y}{W}\right),\qquad(3.50)$$

Based on these levels of particle refinement, and using the analytical solution given by Eq. (3.50), we have performed a convergence study, taking as an error metric the L_2 norm of the global error [108, 110]

$$L_2\,\text{error} = \sqrt{\frac{1}{N_f}\sum_{i\in\text{fluid}}\left(v_x^{\mathrm{a}}(y_i) - v_{x,i}^{\mathrm{sph}}\right)^2},\qquad(3.51)$$

where N_f refers to the total number of fluid particles used in the L_2 error summation.

(a)

(b)

(c)
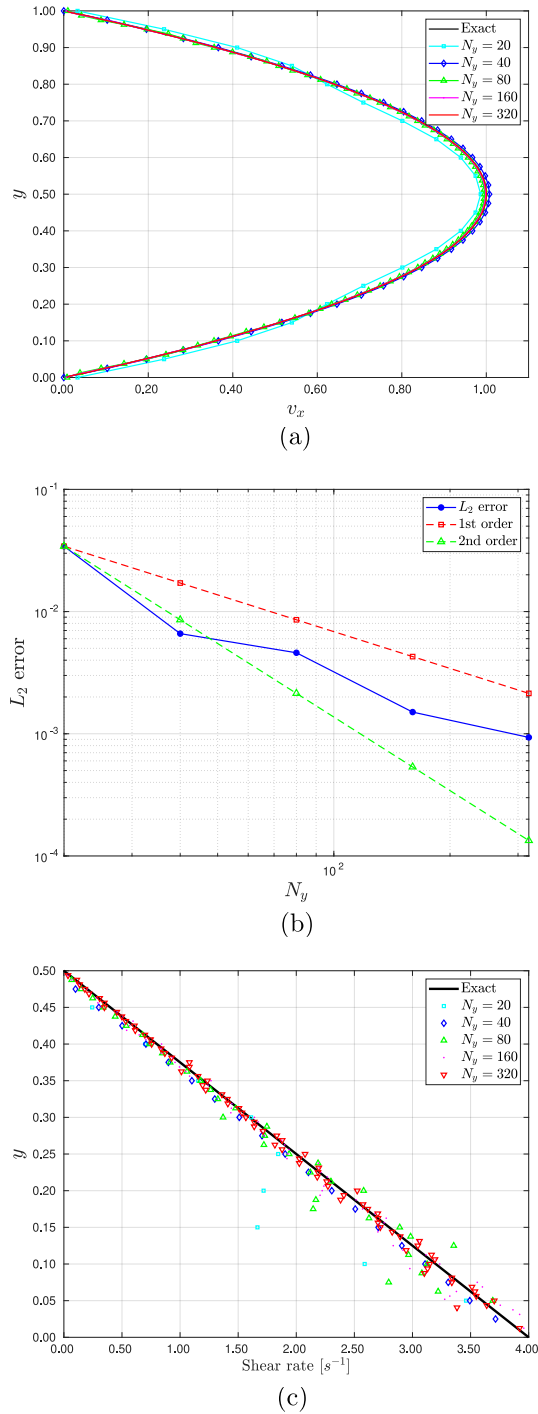
Figure 3.2:   Results from the SPH-BVF method using the Lucy kernel: (a) Streamwise profiles of a fully-developed, steady-state Poiseuille flow in a periodic channel, for $N_y = 20, 40, 80, 160$ and 320 particles in the cross-stream direction. (b) Convergence graph showing the L_2 error versus the refinement. (c) Comparison of shear rate in the lower part $(0 \leq y \leq 0.5)$ of the channel.

Table 3.1:   Estimated errors and convergence rate of
Poiseuille flow for different kernels.

Kernel	N_y	L_2 Error[a]	Converg. rate, p
Lucy	20	3.425×10^{-2}	-
Lucy	40	6.598×10^{-3}	2.376
Lucy	80	4.601×10^{-3}	0.520
Lucy	160	1.505×10^{-3}	1.612
Lucy	320	9.340×10^{-4}	0.688
Cubic spline	20	2.169×10^{-2}	-
Cubic spline	40	1.690×10^{-2}	0.360
Cubic spline	80	9.512×10^{-3}	0.828
Cubic spline	160	5.786×10^{-3}	0.718
Cubic spline	320	6.620×10^{-4}	-0.194
Wendland quintic	20	3.153×10^{-2}	-
Wendland quintic	40	2.864×10^{-2}	0.138
Wendland quintic	80	7.022×10^{-3}	2.028
Wendland quintic	160	1.408×10^{-2}	-1.003
Wendland quintic	320	1.206×10^{-2}	0.223

[a] Error computed at steady-state, $t = 100$.

The errors obtained from the convergence study are provided in Table 3.1. The streamwise velocity profile of the flow is shown in Fig. 3.2-(a) for all of the refinement levels. As reported in [108], we noticed that the error of the proposed BVF boundary condition has a non-constant slope, oscillating between first and second order convergence, as is observed under the Lennard-Jones and fictitious particles boundary conditions. This behavior is depicted in Fig. 3.2-(b). This result is expected because no kernel correction technique was enforced near the boundary, which also justifies the slower convergence behavior of the shear rate near the wall, as depicted in Fig. 3.2-(c). In terms of accuracy, the Lucy kernel performed better than both the cubic spline and Wendland kernels. We found that the Wendland kernel produced more organized particles, but that did not

translate into a higher convergence order. Thus, based on the superior accuracy and simplicity, we have opted to use the Lucy kernel hereafter.

3.4.2   Analytical solution validation: 2D Taylor-Green vortex

The Taylor-Green flow is a closed form solution of the incompressible Navier-Stokes equations, and is widely used to validate fluid flow solvers. It consists of the decaying of a vortex due to viscous effects of the fluid, and is given by the following analytical velocity fields [11]

$$v_x^{\mathrm{a}}(x^*, y^*, t^*) = -U e^{bt^*} \cos(2\pi x^*) \sin(2\pi y^*) \tag{3.52}$$

$$v_y^{\mathrm{a}}(x^*, y^*, t^*) = U e^{bt^*} \sin(2\pi x^*) \cos(2\pi y^*), \tag{3.53}$$

where b is the decay rate of the velocity field and U is the maximum initial velocity. We use Eqs. 3.52-3.53 to estimate the accuracy of the SPH-BVF method. In our simulations, we assume a Reynolds number $Re = UL/\nu = 100$, a maximum velocity $U = 1$, a decay rate $b = -8\pi^2/Re$ and a domain of length $L = 1$. The boundary conditions are periodic in both directions, with $x^*, y^* \in [0, 1] \times [0, 1]$. The initial conditions are obtained by setting the dimensionless time $t^* = tU/L = 0$ in Eqs. 3.52-3.53. The unit length domain is discretized using three levels of equally-spaced particle refinements: $N = 50^2, 100^2$ and 200^2. For each simulation, the relative error of the numerical solution is measured over time using the L_∞ norm, given by

$$L_\infty(t^*) = \left| \frac{\max_i(||\boldsymbol{v_i}(t^*)||) - U e^{bt^*}}{U e^{bt^*}} \right|. \tag{3.54}$$

Figure 3.3 shows snapshots of the particles at dimensionless times $t^* = 0.1, 0.5$ for the

case of $N = 50^2$. The top figures (a,b) show the results for the standard SPH, and the bottom figures (c,d) correspond to results from the present method (SPH-BVF). In (a,b), it is possible to visualize the anisotropic particle alignment caused by tensile instability. This alignment results in excessive diffusion, leading to a fast decay of the velocity field. In contrast, the results obtained by the SPH-BVF method (c,d) dramatically reduce the particle alignments and tensile instabilities, thus preserving the velocity decay. Remarkably, we found that the SPH-BVF method was able to prevent tensile instabilities even in the case of an initial regular lattice particle distribution. No significant differences were observed for other arrangements of particles (data not shown), including randomly shifted arrangements. Conversely, in the work of Adami et al. [11], it was found that the original transport-velocity formulation was sensitive to the initial particle distribution. We believe that our method does not suffer from this sensitivity, thus resulting in a more accurate velocity decay.

The velocity decay is shown in Fig. 3.4. We compare our results with the exact solution Ue^{bt^*} and plot the maximum velocity for all three particle refinements ($N = 50^2, 100^2, 200^2$). Following [11], we also compare our method with standard SPH, showing that the latter fails to predict the exact decay. In contrast, the SPH-BVF method accurately predicts the decay, even for the coarser refinement ($N = 50^2$). Compared to [11], the SPH-BVF method appears to not suffer from the shifted profile obtained by the original transport-velocity formulation.

In addition to the velocity decay, the temporal evolution of the L_∞ norm, Eq. (3.52), is shown in Fig. 3.5. The relative error of the maximum velocity, L_∞, is $\approx 2\%$ for all tested cases. This result is comparable to the best results obtained by [11] (non-regular initial particle distribution, $N = 200^2$). Remarkably, the SPH-BVF method was able to achieve excellent results even at the lowest resolution ($N = 50^2$, equally spaced, regular lattice particle distribution).
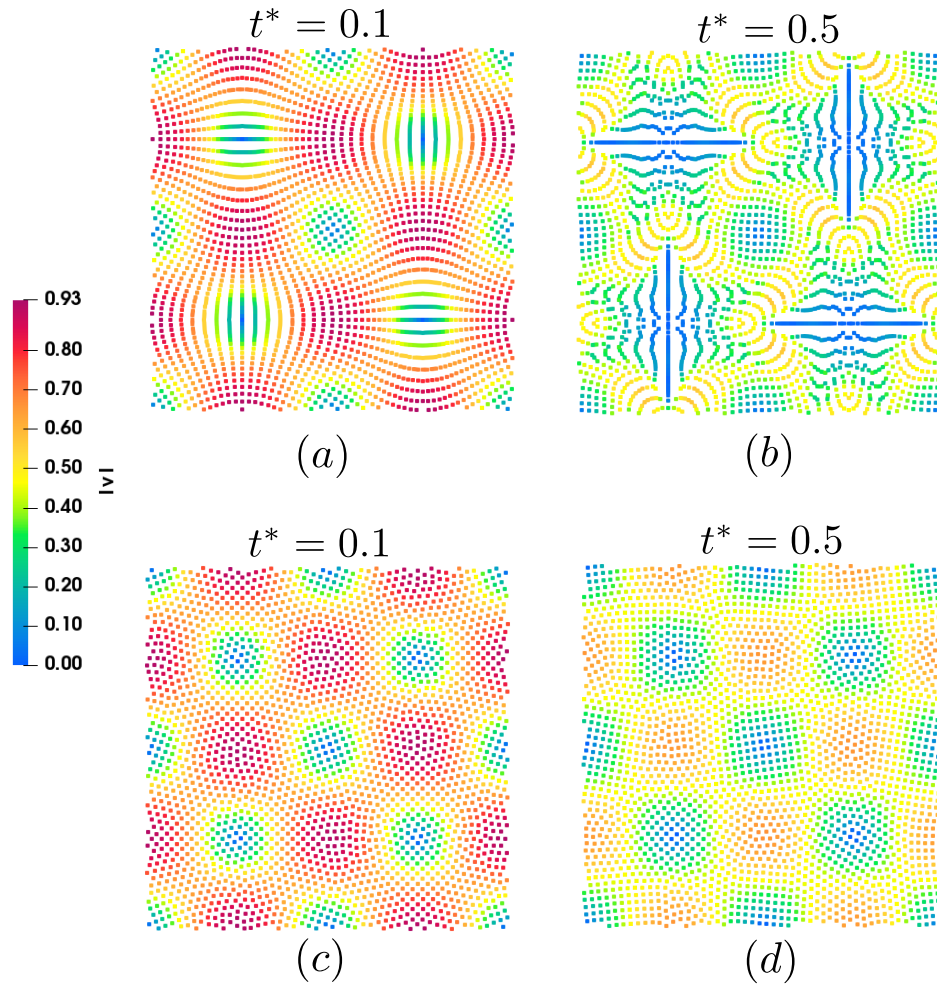
Figure 3.3:   Contour plots of the norm of the velocity vector showing particle arrangements in 2D Taylor-Green vortex simulations at two time points: (a) Standard SPH, $t^* = 0.1$, (b) Standard SPH, $t^* = 0.5$, (c) SPH-BVF (present method), $t^* = 0.1$, (d) SPH-BVF (present method), $t^* = 0.5$.
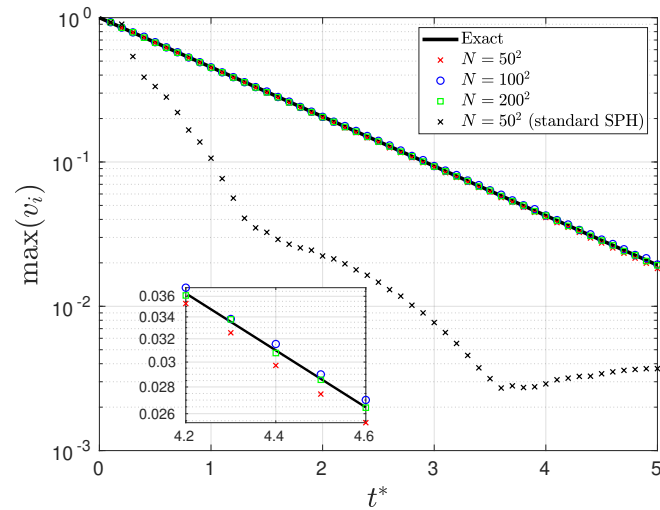
Figure 3.4:   Temporal evolution of the decay of the maximum velocity (semi-log scale) in 2D Taylor-Green vortex simulations for three particle refinements (N) that are compared to the exact analytical solution and standard SPH. Inset shows an expanded view of a section of the graph.
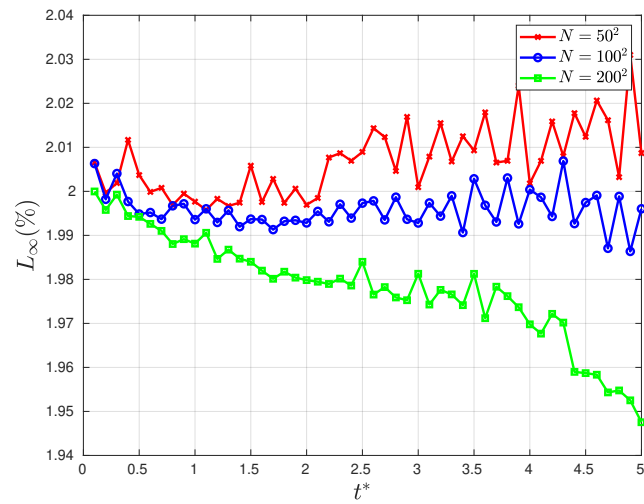
Figure 3.5:   Temporal evolution of the relative error of the maximum velocity (L_∞ norm) in the Taylor-Green simulations for three particle refinements (N).

3.4.3   Fluid mechanics validation: lid-driven cavity flow

The lid-driven cavity flow is a classical model problem, and is considered a challenging problem to be solved using SPH [75]. We validate the proposed method using the high-resolution finite difference numerical experiment carried out by [111]. It consists of a square cavity of side L, filled with a Newtonian fluid of kinematic viscosity $\nu = \mu/\rho$. Gravity effects are considered negligible. In Fig. 3.6(a), the schematic of the lid-driven cavity flow is presented.

The flow, initially at rest, is induced by shear as the lid of the cavity starts moving at uniform velocity v_0. The governing equations are nondimensionalized, in order to validate our results with the reference. The dimensionless groups are given by

$$x_o = L, \tag{3.55}$$

$$t_o = x_o/v_o, \tag{3.56}$$

$$P_o = \rho_o v_o^2, \tag{3.57}$$

where ρ_o is a reference density, considered here as unity. Using these groups, Eqs. (3.1)-(3.2) can be written as

$$\frac{d\rho^*}{dt^*} = -\rho^* \boldsymbol{\nabla}^* \cdot \boldsymbol{v}^*, \tag{3.58}$$

$$\frac{d\boldsymbol{v}^*}{dt^*} = -\boldsymbol{\nabla}^* p^* + \frac{1}{Re} \nabla^{*2} \boldsymbol{v}^*, \tag{3.59}$$

where $Re = v_0 L/\nu$ denotes the Reynolds number with respect to the characteristic length L. The walls of the cavity are modeled using three layers of fixed solid particles, so that near-wall fluid particles are guaranteed to have enough support for accurate ϕ_i

72

computations.

To test the convergence of the method, simulations were performed using three levels of particle refinement ($N = 50^2, 100^2, 200^2$ particles) for each Reynolds regime ($Re = 10^2, 10^3, 10^4$), resulting in a total of nine simulations. In all cases, we have used the Lucy kernel, with cutoff $h = 2.6\Delta p$. We assumed that steady-state was reached once the total kinetic energy of the system was constant over time within a 10^{-3} tolerance.

An overview of the flow dynamics on the lid-driven cavity is provided in Figs 3.9(b)-(c), showing the isocontours of the flow velocity magnitude for each Reynolds flow regime using $N = 200^2$ particles. Figure 3.7 shows the vertical and horizontal velocity profiles for all three levels of particle refinement. For $Re = 10^2$, the method provides results comparable to the reference, even for the smallest particle refinement, $N = 50^2$. For $Re = 10^3$, the SPH-BVF results converge to the reference values. Notice that for $N = 200^2$ particles, the results are very close to those of the reference, even though [111] used a higher resolution (257^2 mesh). For $Re = 10^4$, it is possible to infer the convergence to the reference solution as the refinement level increases. Nevertheless, as observed by [11], a deviation from the reference data is observed, which can be justified by the requirement of a higher refinement level and by the lack of turbulence modeling. For $Re > 10^4$, the flow does not converge to a steady-state [111].
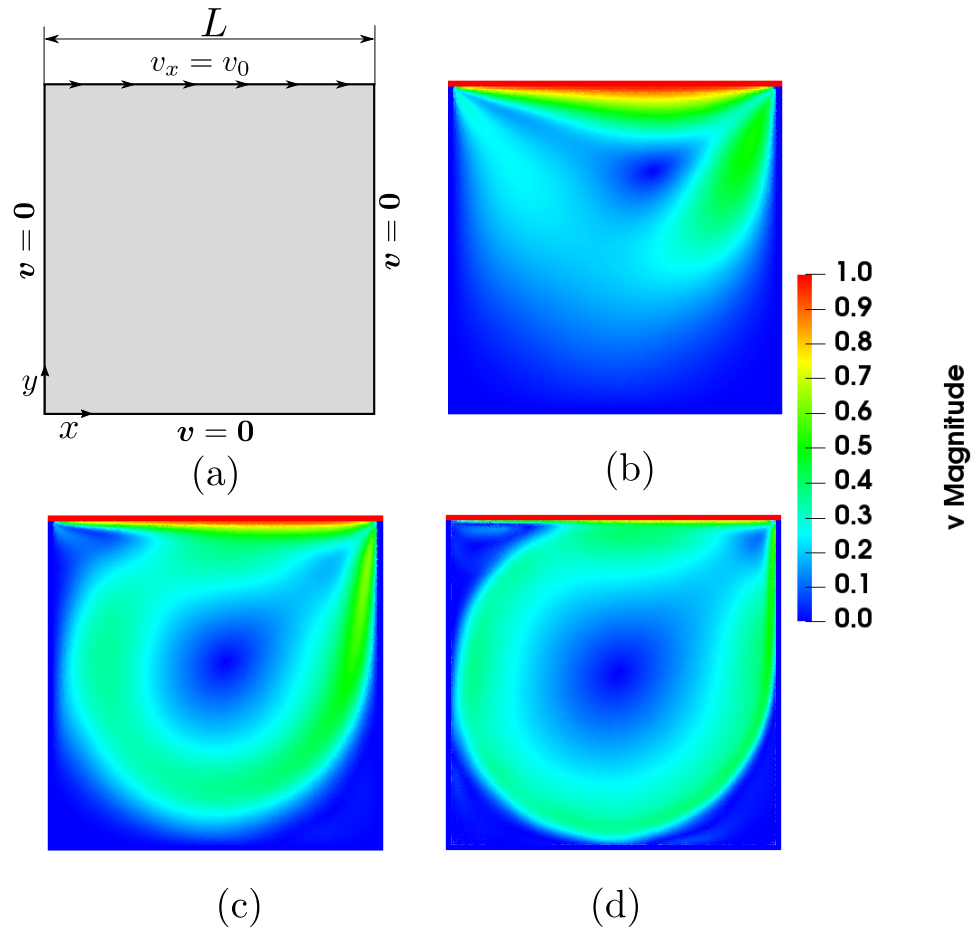
Figure 3.6: (a) Schematic of lid-driven cavity flow. Isocontours of velocity magnitude for (b) $Re = 10^2$, (c) $Re = 10^3$ and (d) $Re = 10^4$ at steady-state.
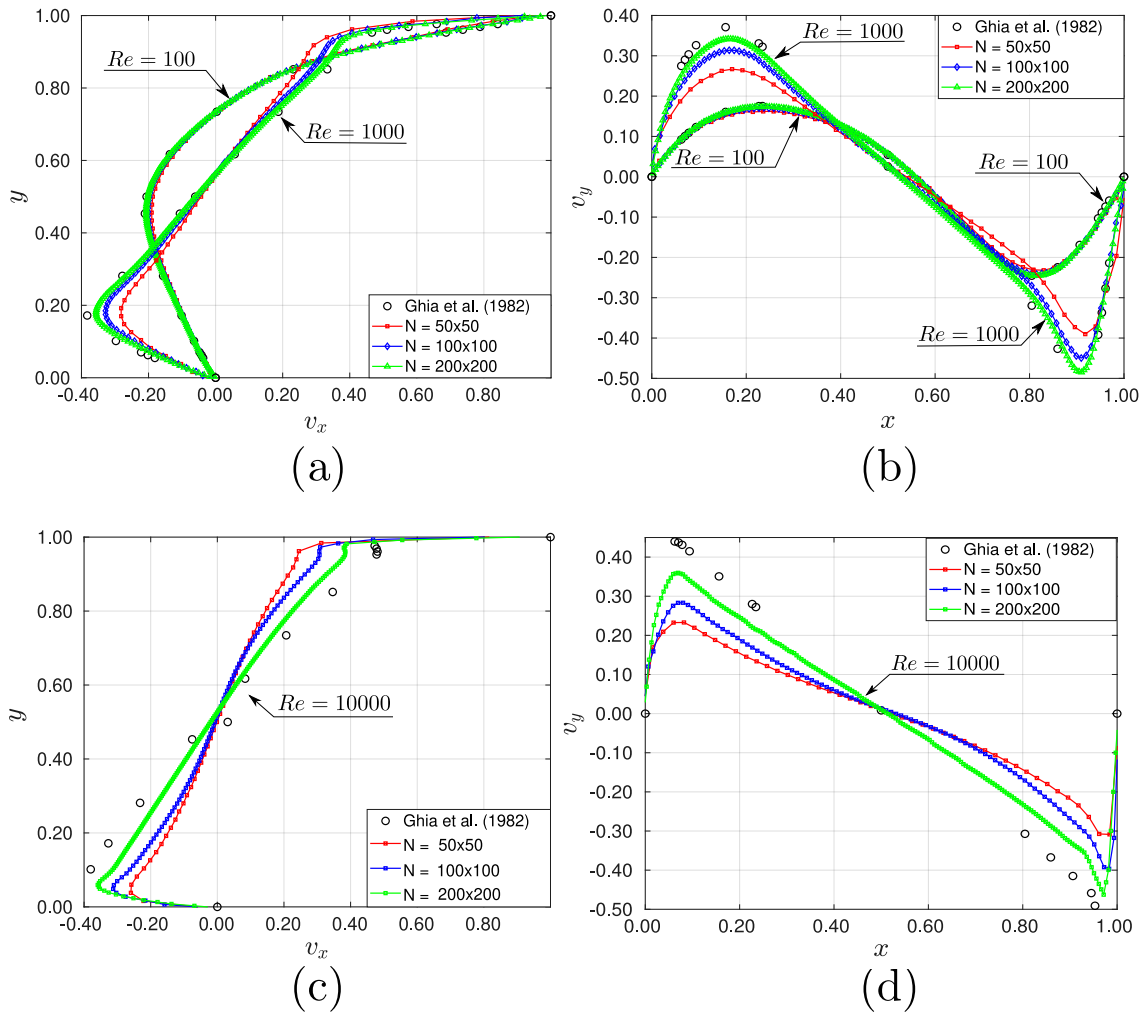
Figure 3.7:   (a), (c) Vertical and (b), (d) horizontal velocity profiles for $Re = 10^2$, $Re = 10^3$ and $Re = 10^4$ compared with the reference results of [111].

Figure 3.8 shows the streamlines in the cavity for $Re = 1000$, revealing the two main structures of the flow: the left and right corner vortices. In his work, [111] reported approximated heights of 0.15 and 0.35 for the left and right corner vortices, respectively (c.f. Fig. 3.8). Similarly, the expected values for the widths are approximately 0.20 (left) and 0.30 (right). The sizes of the vortices obtained by our simulations agree with the reference, showing that the SPH-BVF method was able to accurately predict these

vortices, therefore validating the wall boundary formulation.
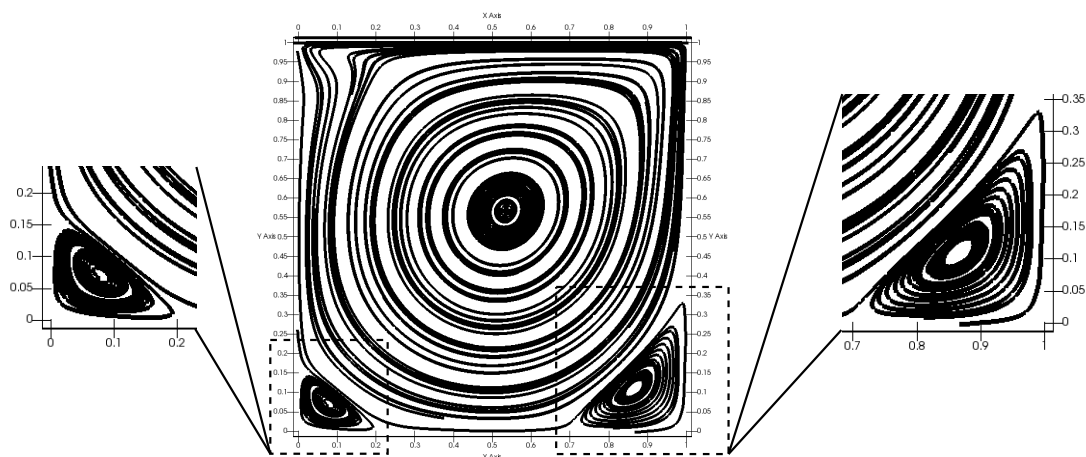
Figure 3.8:   Streamlines and patterns of the corner vortices in the cavity for $Re = 10^3$, obtained with the SPH-BVF method.

3.4.4   Convective transport validation: natural convection

We validate the coupling of advection-diffusion using a coupling force, based on the Oberbeck-Boussinesq approximation [112], in the context of the transport-velocity formulation. To the authors' best knowledge, this is the first time an ALE formulation of SPH has been used to simulate convection. A classical test case widely used in the literature is the natural convection over a cylinder immersed in a square cavity. A complete description of the problem is given in Fig. 3.9. The system consists of a square enclosure, filled with fluid at rest. The wall boundaries of the cavity and in the interface between the cylinder and the fluid are modeled with non-moving SPH particles to enforce the no-slip boundary condition. Initially, the fluid is free of solute, i.e., $C(\boldsymbol{x}, 0) = 0$. At $t > 0$, the wall concentrations of solute in the circular cylinder and at the enclosure walls are set to C_C and C_E, respectively. Since $C_E > C_C$, mass transfer begins to occur, and the system is treated as a binary mixture. The solute diffuses in the fluid over time, leading to mass stratification.
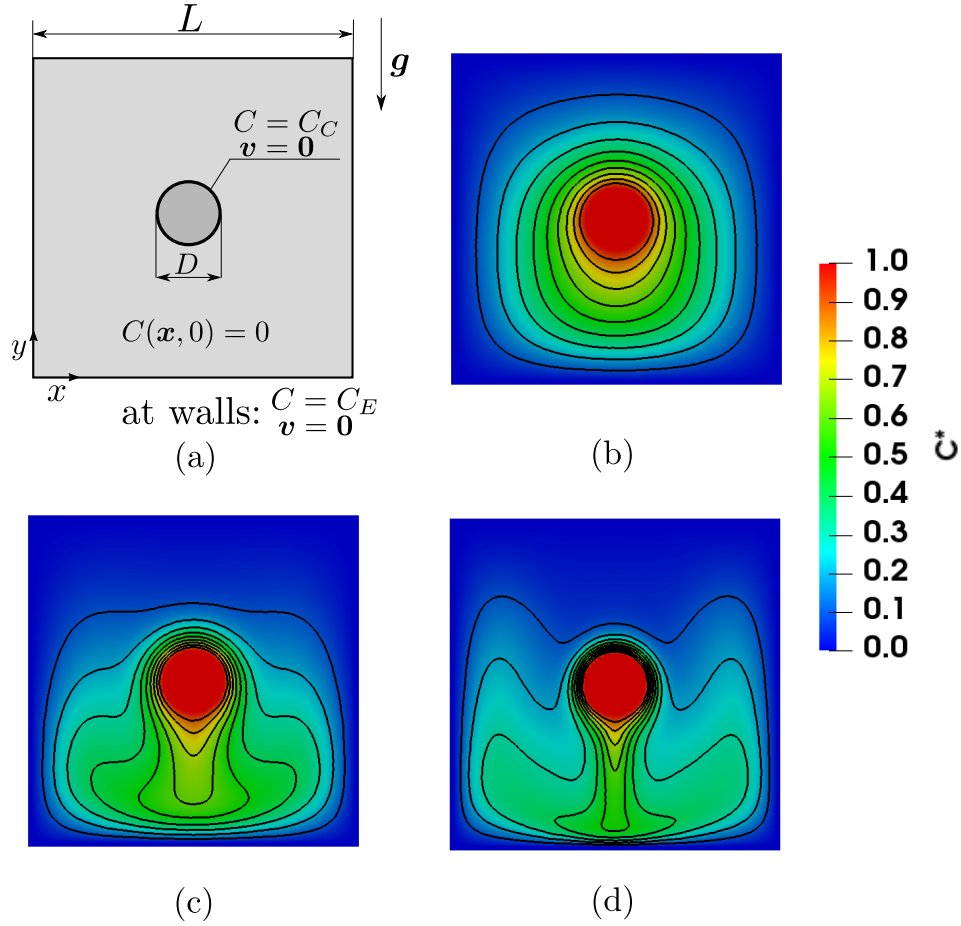
Figure 3.9: (a) Schematic of natural convection in a cylinder inside a square enclosure. (b) Isocontours of the dimensionless concentration field C for $Ra = 10^4$, (c) $Ra = 10^5$ and (d) $Ra = 10^6$ at steady-state.

The Oberbeck-Boussinesq approximation is used to describe the mass transport phenomena, such that a driven body force is proportional to the variation of concentration C, gravity acceleration g and coefficient of mass expansion β. In this case, the body force in Eq. 3.2 takes the form

$$\boldsymbol{F}_{\mathrm{B}} = g\beta\Delta C \,\hat{\boldsymbol{e}}_y, \tag{3.60}$$

where $\Delta C = C - C_{\mathrm{ref}}$, C_{ref} is a reference concentration and $\hat{\boldsymbol{e}}_y$ is the y-direction component

of the standard Cartesian basis, $(\hat{\boldsymbol{e}}_x, \hat{\boldsymbol{e}}_y, \hat{\boldsymbol{e}}_z)$.

The problem was addressed in previous works as natural convection of heat [113, 114, 115, 116], and has been tested in many different geometries [114, 117, 118, 119]. In order to validate results with the work of [113], the equations are rendered dimensionless, using the reference groups proposed by [112]

$$x_o = L, \tag{3.61}$$

$$v_o = \sqrt{g\beta L \Delta C}, \tag{3.62}$$

$$t_o = x_o/v_o, \tag{3.63}$$

$$\Delta C_o = C_C - C_E, \tag{3.64}$$

$$P_o = \rho_o v_o^2, \tag{3.65}$$

where ρ_o is a reference density, considered here as unity. Using these groups, Eqs. (3.1)-(3.3) are rewritten as

$$\frac{d\rho^*}{dt^*} = -\rho^* \boldsymbol{\nabla}^* \cdot \boldsymbol{v}^*, \tag{3.66}$$

$$\frac{d\boldsymbol{v}^*}{dt^*} = -\boldsymbol{\nabla}^* P^* + \sqrt{\frac{Sc}{Ra}} \nabla^{*2} \boldsymbol{v}^* + C^* \hat{\mathbf{e}}_y, \tag{3.67}$$

$$\frac{dC^*}{dt^*} = \frac{1}{\sqrt{RaSc}} \nabla^{*2} C^*, \tag{3.68}$$

where $Sc = \nu/\alpha$ and $Ra = g\beta \Delta C L^3/\nu\kappa$ denote the Schmidt and mass transfer Rayleigh numbers, respectively.

Simulations were performed for $Ra = 10^4, 10^5$ and 10^6. The Schmidt number was taken to be equal to 0.7, and the cylinder diameter as $D = 0.2L$. For all the cases,

the same number of particles N and same initial conditions were provided. The initial setup consists of $N = 200^2$ equally-spaced particles distributed in a squared domain of length $L = 1$. In all cases, we have used the Lucy kernel, with cutoff $h = 2.6\Delta p$. Boundary conditions are imposed using three layers of boundary particles in the walls. The cylinder at the center of the cavity is considered a boundary. Dirichlet boundary conditions are imposed by directly setting the concentration of boundary particles. As in the cavity flow, we assumed that steady-state was reached once the total kinetic energy of the system was constant over time within a 10^{-3} tolerance.
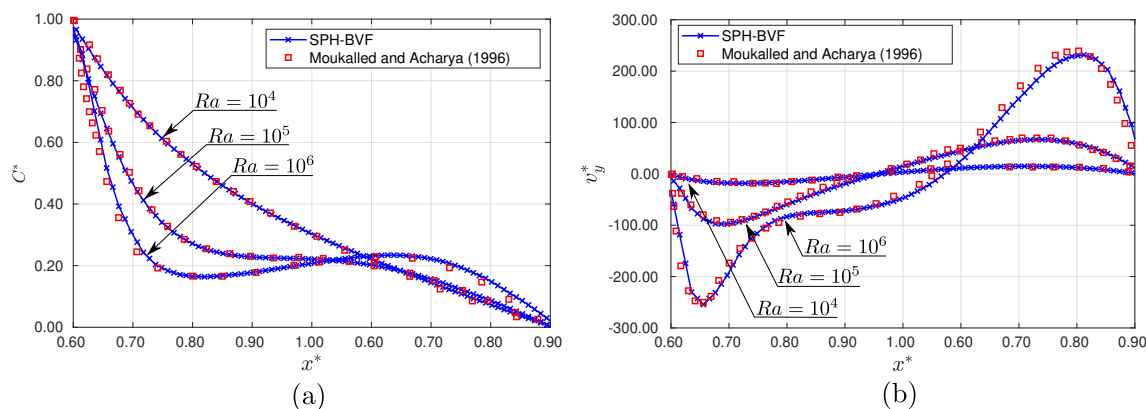
Figure 3.10:   (a) Profiles of dimensionless concentration C^* and (b) y-velocity v_y^* profiles along the horizontal centerline of the cavity, for $Ra = 10^4, 10^5$ and 10^6, at steady-state.

Profiles of the dimensionless concentration, C^*, and y-velocity component, v_y^*, are shown in Figs. 3.10a-3.10b. Results were compared with the numerical simulation of [113]. Since [113] use a different normalization for the velocity, the dimensionless velocity $\boldsymbol{v^*}$ obtained from the solution of Eq. (3.67) must be re-scaled, by multiplying $\boldsymbol{v^*}$ by $\sqrt{Ra/Sc}$.

As depicted in Figs. 3.10a-3.10b, satisfactory results were obtained for all of the Ra regimes. The method was also capable of capturing the stratification of the concentration profiles between the wall and the cylinder surface at $Re = 10^5$ and the concentration inversion that occurs at $Ra = 10^6$, which causes the flow to slow down in the interval
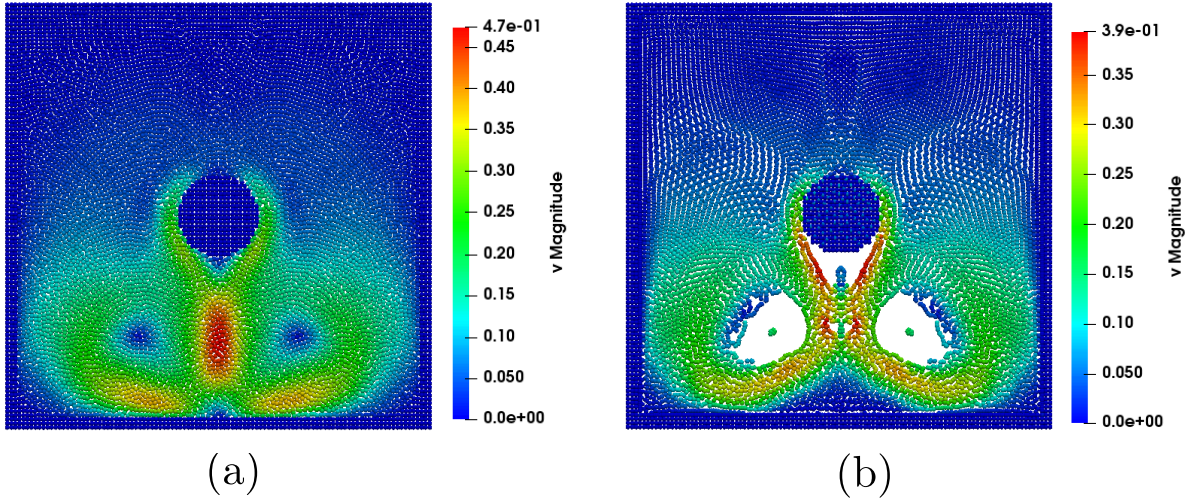
Figure 3.11: Comparison of mean velocity fields at time $t^* = 4$, for the natural convection problem solved using (a) SPH-BVF method and (b) standard SPH [2] method, showing that the proposed method prevents particle penetration and mitigates tensile instability and anisotropic particle alignment.

$0.65 \lesssim x^* \lesssim 0.85$.

A comparison between the mean velocity fields obtained using the present method and standard SPH for $Ra = 10^6$ is shown in Fig. 3.11. While the results obtained by the standard SPH method have serious particle voids, penetration in the walls and in the cylinder, clumping and alignments, the SPH-BVF method mitigated all of these problems, while improving stability. The time step required for a stable simulation with SPH-BVF ($\mathcal{O}(10^{-4})$) was two orders of magnitude larger than the one required in practice using standard SPH, as the soundspeed must be increased to help mitigate the tension instability.

3.4.5   Solid mechanics validation: oscillating cantilever beam

We validate the solid mechanics part of the method with the test case of an oscillating cantilever beam. The problem consists of a thin plate of length L and thickness H, fixed

on one edge and free on the other edges, as shown in Fig. 3.12.
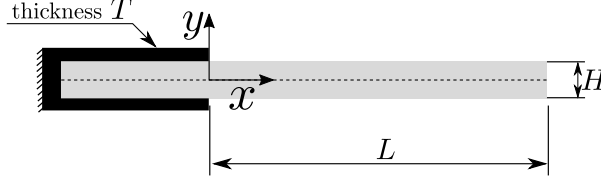

Figure 3.12:   Schematic of the oscillating cantilever beam. The beam, initially at rest, is subject to the initial condition given by Eq. (3.70).

The plate, initially at rest, is set to oscillate at one of its fundamental modes, namely at $kL = 1.875$ [103]. For different modes, other wavenumbers k can be found using the eigensolutions of the Euler-Bernoulli beam equations, given by

$$\cos(kL)\cosh(kL) = -1. \tag{3.69}$$

For the mode $kL = 1.875$, the resulting initial velocity profile is perpendicular to the plate and is given by

$$v_y^0(x) = V_0 c_0 \frac{F(x)}{F(L)}, \tag{3.70}$$

where V_0 is the magnitude of the velocity, c_0 is the soundspeed of the material and F is a force that varies along the length of the plate (x-direction)

$$F(x) = [\cos(kL) + \cosh(kL)][\cosh(kx) - \cos(kx)] \tag{3.71}$$
$$+[\sin(kL) - \sinh(kL)][\sinh(kx) - \sin(kx)].$$

In order to allow a direct comparison with the previous results of [97], we set the plate properties using a Poisson ratio $\nu = 0.3975$, density $\rho = 1 \times 10^3 [kg/m^3]$ and Young's modulus $E = 2.0 \times 10^6 [Pa]$. We have performed simulations for initial velocity amplitudes

$V_0 = 1 \times 10^{-3}, 1 \times 10^{-2}$ and $3 \times 10^{-2}[m/s]$. The artificial stress coefficient [58] is set to 0.2. In all cases, we have used the Lucy kernel, with cutoff $h = 3.0\Delta p$. The fixed support of the plate is constructed with stationary solid particles. For geometrical consistency, thickness of the upper and lower parts of the support were set to $T = H/2$.
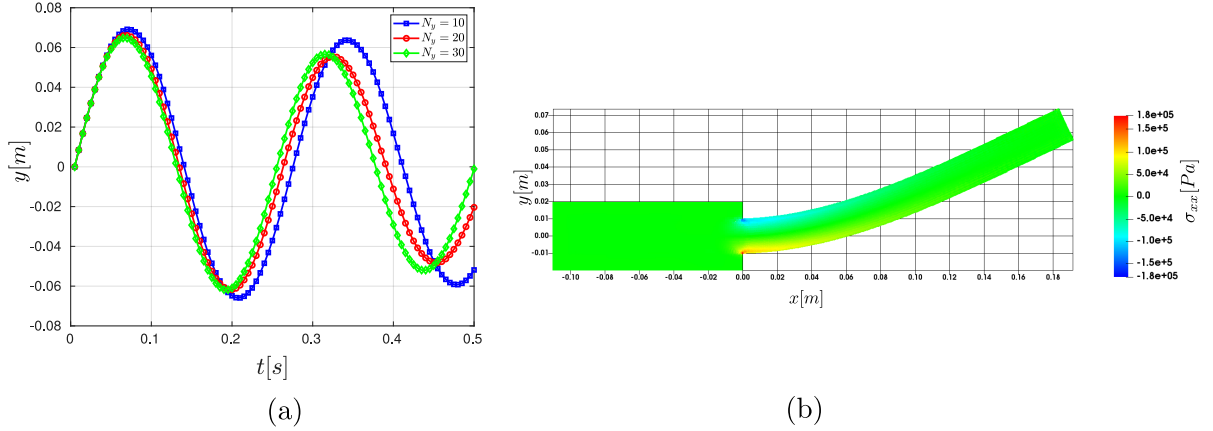

(a)   (b)

Figure 3.13:   (a) Plots of the position of the centerline point at the tip of the beam $(y = 0, x = L)$ for the case of $V_0 = 3 \times 10^{-2}$, illustrating the convergence of the SPH solid mechanics formulation. (b) Contour plots of total stress field σ_{xx} at $t = 0.07[s]$, for the case of $V_0 = 3 \times 10^{-2}$ and $N_y = 30$.

Figure 3.13-(a) shows a convergence study based on the y-position of the centerline point of the beam at the tip $(x = L)$. Results are in good agreement with previous studies [103, 97], and no numerical fracture is observed in the regions of maximum tension, as shown in Figure 3.13-(b), demonstrating that the tension instability was controlled and allowed large deformations of the beam.

A quantitative comparison with the analytical solution of a flat plate [107] for various velocity amplitudes V_0 and a relative error convergence analysis are shown in Table 3.2. The present method achieved relative errors of less than 1% for $N_y = 30$ and all values of V_0 compared to the 13% errors reported by [97].

Table 3.2:   Relative errors for oscillating cantilever beam for various velocity amplitudes V_0 and particle refinements.

V_0	Δp	N_y	First period (present work)	First period (analytical[a])	Relative error (%)
$1 \times 10^{-3}[m/s]$	$0.2/10[m]$	10	$2.747 \times 10^{-1}[s]$	$2.540 \times 10^{-1}[s]$	8.150
$1 \times 10^{-3}[m/s]$	$0.2/20[m]$	20	$2.605 \times 10^{-1}[s]$	$2.540 \times 10^{-1}[s]$	2.559
$1 \times 10^{-3}[m/s]$	$0.2/30[m]$	30	$2.539 \times 10^{-1}[s]$	$2.540 \times 10^{-1}[s]$	-0.039
$1 \times 10^{-2}[m/s]$	$0.2/10[m]$	10	$2.757 \times 10^{-1}[s]$	$2.540 \times 10^{-1}[s]$	8.543
$1 \times 10^{-2}[m/s]$	$0.2/20[m]$	20	$2.618 \times 10^{-1}[s]$	$2.540 \times 10^{-1}[s]$	3.071
$1 \times 10^{-2}[m/s]$	$0.2/30[m]$	30	$2.546 \times 10^{-1}[s]$	$2.540 \times 10^{-1}[s]$	0.236
$3 \times 10^{-2}[m/s]$	$0.2/10[m]$	10	$2.756 \times 10^{-1}[s]$	$2.540 \times 10^{-1}[s]$	8.504
$3 \times 10^{-2}[m/s]$	$0.2/20[m]$	20	$2.635 \times 10^{-1}[s]$	$2.540 \times 10^{-1}[s]$	3.740
$3 \times 10^{-2}[m/s]$	$0.2/30[m]$	30	$2.556 \times 10^{-1}[s]$	$2.540 \times 10^{-1}[s]$	0.623

[a] Based on [97, 107]

3.4.6   Comparison with FEM: fluid-structure interaction

As a final comparison, we demonstrate the ability of the SPH-BVF method to perform simulations of fluid-structure interaction (FSI) problems. The problem, depicted in Fig. 3.14, consists of a horizontal microchannel flow with a narrow vertical rod as an obstacle. A uniform fluid flow is introduced in the channel entry. In the region near the obstacle, the flow is induced into a narrow path in the upper part of the channel, and as a consequence it imposes a force on the structure's walls. The rod, made of a deformable material, bends under the applied load, reaching a steady state.

The wall boundary condition treatment in the SPH-BVF simulations follows the previous validation examples, with wall boundary conditions imposed using three layers of boundary particles in the walls. To model the inlet and outlet boundaries, we adopt the following strategy: as the fluid leaves the channel, it is re-inserted back at the inlet after it passes through a sponge zone, which acts as a non-reflective boundary condition [66] to the flow and re-align the velocity profile. This strategy makes the computation

less intensive as there is no need to destroy particles as they leave the domain, or to create new ones at the inlet, as doing so would require re-creating the particle neighboring list every time step. For details on the implementation of the sponge zone, we refer the reader to [120].

Since the problem has no analytic solution, we compare our numerical simulation with high-resolution FEM using the FSI package in Comsol Multiphysics (v.5.3). The physical parameters for both FEM and SPH-BVF simulations are given in Table 3.3.
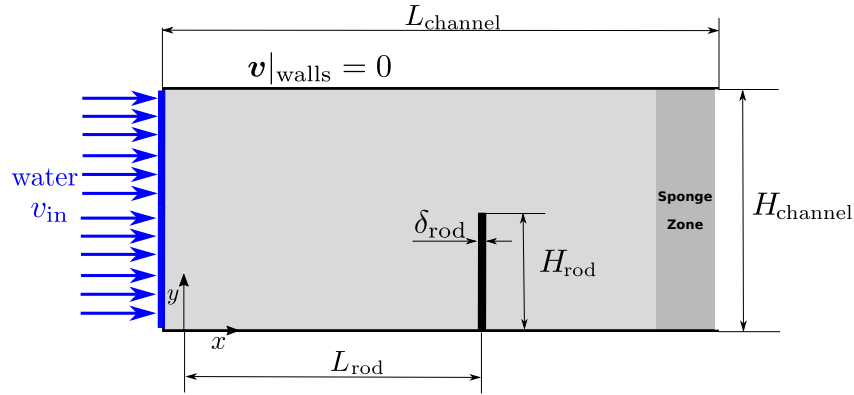
Figure 3.14:   Schematic of the FSI problem. Water enters a 2D microchannel, filled with water at rest, with uniform velocity v_{in}. An elastic rod located at the middle of the channel and fixed at the lower wall, constrains the fluid flow, causing a deformation in the rod.

Table 3.3:   Physical parameters adopted in the FSI simulation.

Parameter	Value	Description
H_{channel}	$100\,[\mu m]$	channel height
L_{channel}	$300\,[\mu m]$	channel width
H_{rod}	$50\,[\mu m]$	rod height
L_{rod}	$100\,[\mu m]$	horizonta position (rod)
δ_{rod}	$5\,[\mu m]$	rod thickness
E	$2 \times 10^5\,[Pa]$	Young modulus (rod)
ν_p	0.33	Poisson ratio (rod)
ρ_f	$1000\,[kg/m^3]$	fluid density
ρ_{rod}	$7850\,[kg/m^3]$	rod density
μ_f	$10^{-3}\,[Pa\,s]$	viscosity of fluid
v_{in}	$3.33 \times 10^{-2}\,[m/s]$	inlet fluid velocity

The SPH-BVF simulation was performed using $30,000$ fluid particles (representing the water) and 500 solid particles (representing the rod). The FEM solution was obtained using second-order shape functions in a mesh of approximately 12,000 elements. We assumed that steady-state was reached once the kinetic energy of the fluid flow was constant over time within a 10^{-3} tolerance.

Contour plots of the streamwise (v_x) and cross-stream (v_y) velocity components at steady-state are shown in Figs. 3.15-(a) and (b). Is possible to see the bending of the beam to the right, as a consequence of the flow, as well as boundary layer in the near-wall regions of the channel. To validate the velocity profiles, a probe was placed along the y-centerline of the channel.

Figures 3.15-(c) and (d) show the velocity profiles of the channel at the probe, and a comparison with the FEM result. It is important to highlight that the comparison of velocity profiles in FEM and SPH-BVF agree in magnitude, demonstrating that the formulation for the non-reflexive boundary condition is satisfactory, as well as in phase, which demonstrates that the point of maximum deflection obtained in both the FEM and SPH-BVF solutions are very close. However, notice that the stream-wise velocity v_x drops at the end of the channel, due to the presence of the sponge zone. Further investigations in non-reflective boundary conditions in SPH are required to improve these results.
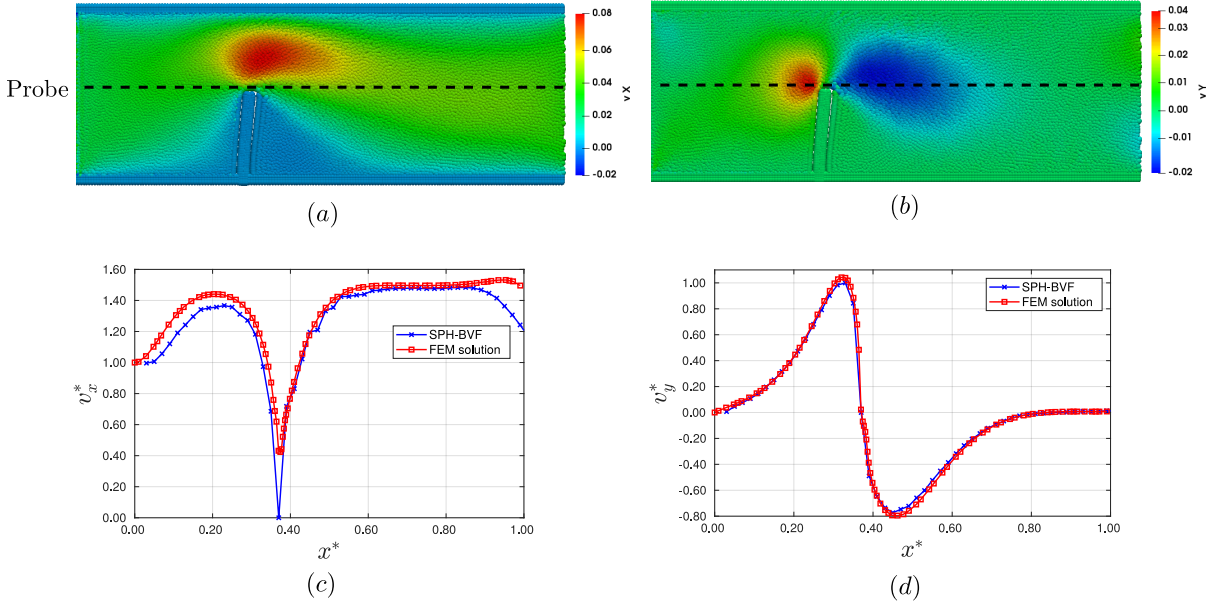
Figure 3.15:   Top: contour plots of the (a) streamwise v_x and (b) cross-stream v_y velocity fields at steady-state. The beam has deformed slightly to the right. Bottom: comparison of dimensionless velocity profiles (c) v_x^* and (d) v_y^* for a probe located at the y-centerline of the channel, as depicted in the velocity profiles. Variables were rendered dimensionless for scaling purposes, as $v_x^* = v_x/v_{\text{in}}$ and $x^* = x/L_{\text{channel}}$.

3.5   Application: polarized yeast cell undergoing mating projection growth

To further demonstrate the capability of the proposed method, we apply SPH-BVF to a biomechanics problem that poses a challenge for classic SPH as well as mesh-based methods because it involves deforming boundaries under pressure, fluid-structure interaction, particle non-penetration and a conjugate transport mechanism (diffusion of chemical species that alters the mechanical properties of the material). The first attempt to simulate the mechanics of biological cells was performed by [121, 122], using an SPH-DEM hybrid method to study the mechanical response of plant cells under compression. The model, however, is purely mechanical, and therefore the reaction-diffusion dynamics

86

of species in the cell wall are not considered.

The motivating problem is the growth of the mating projection in a yeast cell (*S. cerevisiae*) responding to mating pheromone in the extracellular fluid [123]. The key structure is the cell wall, which defines the shape of the cell while providing the mechanical integrity necessary to withstand the large internal turgor pressure [124]. As depicted in Fig. 3.16, under the isotropic turgor pressure, polarized growth occurs via localized softening of the cell wall by the enzymatic digestion of the polymer crosslinks, inducing expansion at the tip. A mechanical feedback pathway delivers new wall material to this growing region by vesicular transport, leading to expansion of the mating projection in the area targeted by the wall-modifying enzyme [125]. This problem demonstrates our method on curved and dynamically changing boundaries representing the cell wall. Importantly, the interior fluid, the cytoplasm, does not penetrate the cell wall even while under sufficient pressure to cause the wall to change shape.
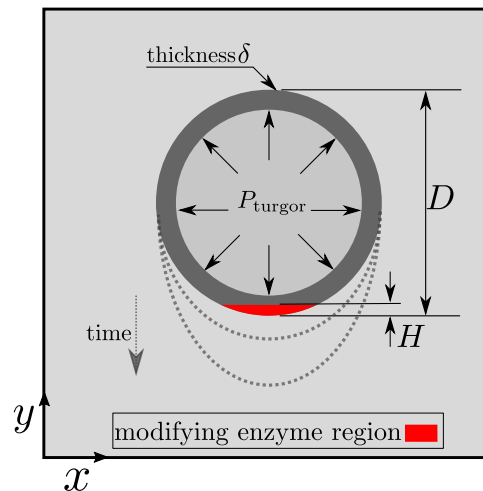

Figure 3.16:   Schematic of yeast cell projection growth model. Cell wall modifying enzymes localized to region in red cause the softening of the cell wall. The internal turgor pressure pushes and deforms the cell wall at this weakened section, creating a mating projection. D is the diameter of the cell, H is the height of the enzyme region, and δ is the thickness of the cell wall.

3.5.1   Simplified model of yeast mating projection

Yeast mating projection growth is a classic example of cell polarization, and has been investigated experimentally [126, 127, 128] and through mathematical modeling [129, 130, 131]. Existing models have focused primarily on the reaction-diffusion dynamics of the signal transduction system. However, more recent work has highlighted the complex interplay between the biochemical dynamics within the mating projection and the mechanical forces acting on the cell wall to determine the shape of the cell [125]. It is important to note that the properties of the biological materials involved are not well-characterized. For example, recent studies [132, 133] showed that cytoplasm can assume different properties, changing from a viscous fluid to an elastic solid, and can be considered compressible or incompressible, depending on the state of tension, biological process involved and external perturbations. Given that the SPH-BVF method is currently limited to linear elastic solids and Newtonian fluids, we assume that the cytoplasm is a compressible fluid, and that the cell wall is a linear elastic material characterized by a shear modulus. Finally, the extracellular fluid around the cell possesses the rheological properties of water.

For simplicity, we employ the following approximation of the coupling between the mechanical and biochemical systems. In the model, cell wall modifying enzymes, whose concentration is denoted by the variable c, decrease the shear modulus of the cell wall according to the following linear equation: $G(c) = G_0(1 - c\,R)$, in which R is a parameter representing wall degrading enzymatic activity, and G_0 is the reference shear modulus of the non-polarized wall region. The modifying enzymes are able to diffuse in the wall with a diffusion constant given by κ_c.

Even under these simplifying assumptions, the model is still complex enough that advanced computer-aided engineering (CAE) tools have difficulty simulating the coupled

problem. For example, COMSOL (v.5.3a) is not capable of simulating dynamic mechanical properties coupled with diffusive transport in a moving mesh, hence no direct comparison could be made.

3.5.2 Results

To demonstrate that SPH-BVF can simulate yeast mating projection growth, we chose to vary the diffusion coefficient κ_c of the wall-modifying enzymes using two different values. The other parameters were kept constant with the enzyme initially distributed in a region of width $H = \delta/2$, where δ is the cell wall thickness. The initial enzyme concentration was set to be $c = 1\,[mol/m^3]$ in this region, and to $c = 0\,[mol/m^3]$ in the rest of the cell wall. The enzyme affects the shear modulus of the cell wall according to the linear relationship described above as it diffuses from its initial site. A list of the physical parameters used in the simplified model is provided in Table 3.4, and a reference table with each case is detailed in Table 3.5.

Table 3.4:   Physical parameters used in the cell polarization simulation.

Parameter	Value	Description
δ	$2.5\,[\mu m]$	cell wall thickness
D	$10\,[\mu m]$	diameter of the cell
H	$1.25\,[\mu m]$	height of enzyme region
E	$10^6\,[Pa]$	Young modulus of cell wall
G_0	$3.58 \times 10^5\,[Pa]$	reference shear modulus of cell wall
ν_p	0.3975	Poisson ratio of cell wall
K_f	$5 \times 10^5\,[Pa]$	bulk modulus of extracellular fluid
K_c	$5 \times 10^5\,[Pa]$	bulk modulus of cytoplasm
ρ_f	$1000\,[kg/m^3]$	density of extracellular fluid
ρ_c	$1500\,[kg/m^3]$	density of cytoplasm
ρ_w	$1100\,[kg/m^3]$	density of cell wall
μ_f	$10^{-3}\,[Pa\,s]$	dynamic viscosity of fluid
μ_c	$10^{-3}\,[Pa\,s]$	dynamic viscosity of cytoplasm
R	$0.99[m^3/mol]$	rate of enzymatic softening

Table 3.5:   Two cases simulated with parameter values and number of particles.

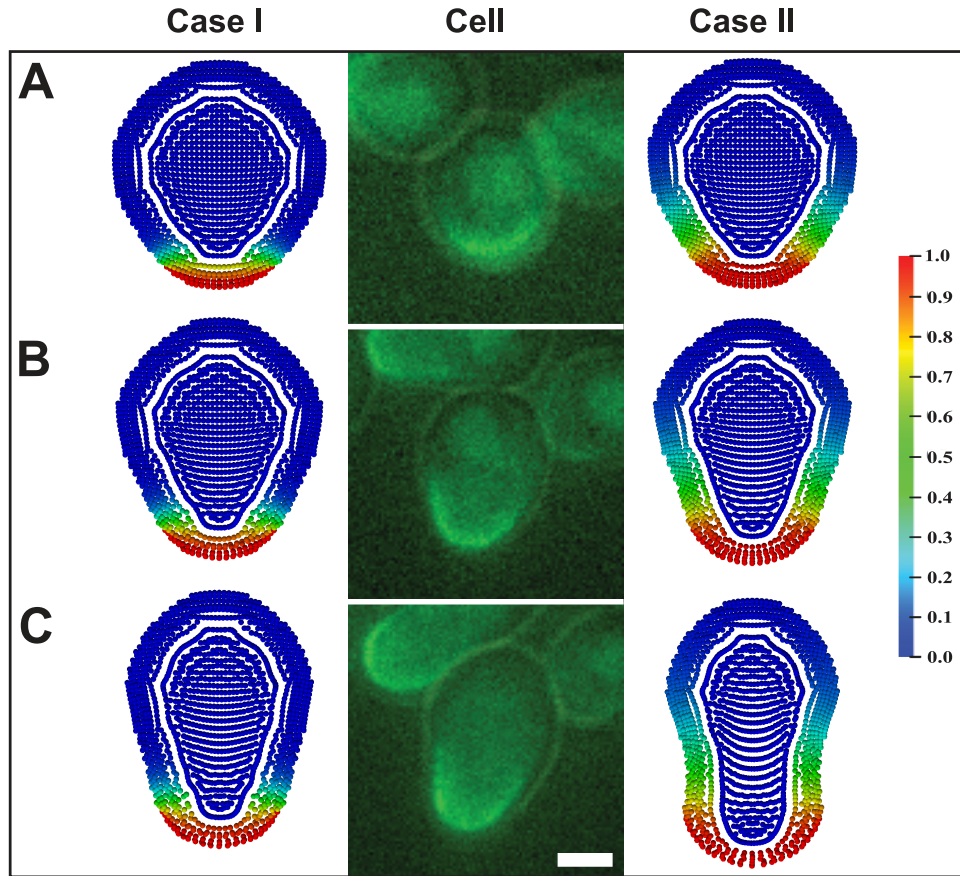| Case number	Mass diffusivity (κ_c)	Number of particles (N)
I	$10^{-13}\,[m^2/s]$	840 (wall), 716 (cytoplasm)
II	$10^{-12}\,[m^2/s]$	840 (wall), 716 (cytoplasm)

Figure 3.17:   Simulations and experiments showing yeast mating projection growth over time. Cases I (left column, $\kappa_c = 10^{-13}\,[m^2/s]$), II (right column, $\kappa_c = 10^{-12}\,[m^2/s]$), and microscopy images of a *spa2*Δ cell responding to 1 μM mating pheromone α-factor (central column). Particles are colored by the concentration c of wall-modifying enzymes. Rows A, B and C indicate times of 2000, 3000 and 4000 seconds, respectively, for the simulations, and 30, 60, and 90 minutes for the experiments. Cells contain the secretion marker protein Fus1-GFP (green) to indicate where wall-modifying enzymes are transported. A broad tip protrudes from both simulations and experiments. Despite high internal turgor pressure and deformation, SPH-BVF is able to model the deforming boundaries without particle penetration or tension instability. Scale bar = 2 μm.

Figure 3.17 shows snapshots of the two simulations (cases I and II) at the two diffusion

values. Interestingly, the larger diffusion constant produced a longer, laterally concave projection, whereas the smaller diffusion constant preserved its laterally convex shape. One can compare the simulations to time-lapse microscopy images obtained by exposing yeast cells to the mating pheromone α-factor. The cells contain the secretion marker Fus1-GFP which indicates the presumptive location where the wall-modifying enzymes are deposited on the cell wall [134]. Qualitatively speaking, the simulations were able to capture the general shape changes during projection growth, even though some level of particle alignment is observed near the boundary of the cells. One promising way of alleviating this effect is to use an optimal particle arrangement [135], which directly ensures the isotropy of the particle distribution, even without parameter tuning. Regardless, this example demonstrates the potential of the SPH-BVF method to simulate complex biological processes including both biochemical and physical spatial dynamics, involving fluid-structure interactions and materials with time-varying mechanical properties without inducing particle penetration or excessive tension instability.

Chapter 4

Conclusions

In the first part of this dissertation, we have developed a method to simulate both discrete stochastic and continuum deterministic chemical reaction-diffusion systems within an unstructured moving fluid domain whose dynamics are simulated via the smoothed dissipative particle dynamics method. This method has many applications where chemically or biochemically reactive systems are coupled to a moving fluid domain. For example, it will be especially useful for modeling biological cells in which discrete stochastic chemical kinetics are required to accurately describe cellular processes.

It is important to emphasize that because of the Lagrangian nature of SDPD, the coupling with advective transport occurs naturally, with particle positions being updated via the equations of motion. This approach has been proven to work in different scales, ranging from relativistic spaces [136] to quantum systems [137]. Thus, our method preserves the natural advantages of a meshfree method while incorporating the flexibility of resolving small scales only when necessary, making it a complete framework for the simulation of biological multiscale systems.

We use operator splitting to couple the SDPD dynamics of fluid position and velocity, the continuum deterministic reaction-diffusion equations, and SSA discrete stochastic

reaction-diffusion system over each timestep. This allows us to solve a complex interdependent system efficiently and simply, with known error bounds [138, 139].

We have implemented our method within the LAMMPS[140] simulation framework. LAMMPS is a software package for simulation of classical molecular dynamics problems. The advantage of the LAMMPS infrastructure is that is extensible, and has been modified to include simulation capabilities of SPH and DPD (including tDPD in a recent release). We have implemented the SDPD, deterministic reaction-diffusion, and the spatial SSA methods as a user module in LAMMPS, which should allow it to be integrated seamlessly into many different configurations of LAMMPS. We have released the source for our enhancements under the GPL v2.0 license, which is the same license as the LAMMPS software package.

Our simulation methodology has many advantages, but there are still technical limitations. The first is that the compressibility of the SDPD method leads to a performance limitation for applications where incompressibility is critical. In addition, there are issues in specifying boundary conditions when using the SSA simulation method, as it is not as straightforward to specify them in the discrete context compared to the continuous context. Finally, the current implementation of the SSA method requires that the simulations be run in serial, rather than utilizing multi-core parallelism. This is due to the fully connected nature of the SSA method. Our plans for future work include adapting the SSA method to the multi-core parallel context to increase performance.

We believe that this method will lead to advances in the understanding of complex systems. Specifically, we envision its application in the modeling of single cell and multicellular systems possessing changing shapes in dynamic environments subjected to various perturbations. Applications such as this require coupling between physical and chemical systems, a simulation our method is designed to address. For example, sSSA-SDPD is able to simulate both the complex fluid dynamics and the stochastic biochemical reac-

tions of cells in a microfluidics chamber. Finally, we can use the algorithm to model the physical forces and blood flow in tissues coupled to inter- and intra-cellular processes.

In the second part of this dissertation, we introduce a unified framework to simulate solid and fluid mechanics with convective reaction-diffusion transport in SPH. The method, named SPH-BVF, provides a new local wall boundary condition treatment for SPH, which allows particles to become autonomous to detect solid neighbors. The boundary volume fraction (BVF) approach introduces only a small computational overhead, while explicitly preventing fluid penetration through solid boundaries. In addition, SPH-BVF provides good accuracy and improved stability, and due to its ALE formulation, prevents tension instabilities and anisotropic particle alignments.

Similarly to the sSSA-SDPD method, we have developed a software package compatible with the LAMMPS framework. The complete code, along with all of the validations, post-processing routines and the application problem are also available in our source, under the GPL v2.0 license.

While addressing some problems encountered by standard SPH, our method also possesses certain limitations. Simulations require approximately three layers of particles to have sufficient support within the kernel integration area to accurately estimate the boundary volume fraction. As a result, systems with very thin walls may require finer discretization and more particles, which can lead to higher computational costs. One promising approach to overcome this issue in the future is the usage of an immersed boundary method to represent slender bodies [141, 142]. We also note that the proposed BVF boundary condition has a non-constant order of convergence (between first and second order), which is similar to the Lennard-Jones boundary condition using ghost particles.

One promising domain for SPH-BVF is in simulating biophysical systems. Specifically, we envision its application in the modeling of cell dynamics, as well as in other

applications, such as intercellular junction formation, cell morphogenesis and blood flow simulations in tissues coupled to inter- and intra-cellular processes, in which conjugate transport, materials with dynamic mechanical properties and boundary deformation are relevant.

Bibliography

[1] G. Pereira, P. Cleary, and V. Lemiale, *SPH method applied to compression of solid materials for a variety of loading conditions*, Applied Mathematical Modelling **44** (2017) 72 – 90.

[2] R. Gingold and J. Monaghan, *Smoothed particle hydrodynamics - Theory and application to non-spherical stars*, mnras **181** (Nov., 1977) 375–389.

[3] L. B. Lucy, *A numerical approach to the testing of the fission hypothesis*, Astronomical Journal **82** (Dec., 1977) 1013–1024.

[4] X. Bian, S. Litvinov, R. Qian, M. Ellero, and N. A. Adams, *Multiscale modeling of particle in suspension with smoothed dissipative particle dynamics*, Physics of Fluids **24** (2012), no. 1 012002, [https://doi.org/10.1063/1.3676244].

[5] A. Vázquez-Quesada, X. Bian, and M. Ellero, *Three-dimensional simulations of dilute and concentrated suspensions using smoothed particle hydrodynamics*, Computational Particle Mechanics **3** (Apr, 2016) 167–178.

[6] H. Lei, C. J. Mundy, G. K. Schenter, and N. K. Voulgarakis, *Modeling nanoscale hydrodynamics by smoothed dissipative particle dynamics*, The Journal of Chemical Physics **142** (2015), no. 19 194504, [https://doi.org/10.1063/1.4921222].

[7] N. Moreno, P. Vignal, J. Li, and V. M. Calo, *Multiscale modeling of blood flow: Coupling finite elements with smoothed dissipative particle dynamics*, Procedia Computer Science **18** (2013) 2565 – 2574. 2013 International Conference on Computational Science.

[8] K. Müller, D. A. Fedosov, and G. Gompper, *Margination of micro- and nano-particles in blood flow and its effect on drug delivery*, Nature Scientific Reports **4** (May, 2014). Article.

[9] H. Lei, N. A. Baker, L. Wu, G. K. Schenter, C. J. Mundy, and A. M. Tartakovsky, *Smoothed dissipative particle dynamics model for mesoscopic multiphase flows in the presence of thermal fluctuations*, Phys. Rev. E **94** (Aug, 2016) 023304.

[10] S. Litvinov, Q. Xie, X. Hu, N. Adams, and M. Ellero, *Simulation of individual polymer chains and polymer solutions with smoothed dissipative particle dynamics*, *Fluids* **1** (2016), no. 1.

[11] S. Adami, X. Hu, and N. Adams, *A transport-velocity formulation for smoothed particle hydrodynamics*, *Journal of Computational Physics* **241** (2013) 292 – 307.

[12] X. Xu and X.-L. Deng, *An improved weakly compressible SPH method for simulating free surface flows of viscous and viscoelastic fluids*, *Computer Physics Communications* **201** (2016) 43 – 62.

[13] S. Hieber and P. Koumoutsakos, *An immersed boundary method for smoothed particle hydrodynamics of self-propelled swimmers*, *Journal of Computational Physics* **227** (2008), no. 19 8636 – 8654.

[14] R. Vacondio, B. Rogers, P. K. Stansby, P. Mignosa, and J. Feldman, *Variable resolution for sph: a dynamic particle coalescing and splitting scheme*, *Computer Methods in Applied Mechanics and Engineering* **256** (2013) 132–148.

[15] D. A. Barcarolo, D. Le Touzé, G. Oger, and F. De Vuyst, *Adaptive particle refinement and derefinement applied to the smoothed particle hydrodynamics method*, *Journal of Computational Physics* **273** (2014) 640–657.

[16] R. Vacondio, B. Rogers, P. K. Stansby, and P. Mignosa, *Variable resolution for sph in three dimensions: Towards optimal splitting and coalescing for dynamic adaptivity*, *Computer Methods in Applied Mechanics and Engineering* **300** (2016) 442–460.

[17] Z. Ji, L. Fu, X. Y. Hu, and N. A. Adams, *A new multi-resolution parallel framework for SPH*, *Computer Methods in Applied Mechanics and Engineering* **346** (2019) 1156–1178.

[18] C. Zhang, M. Rezavand, and X. Hu, *A multi-resolution SPH method for fluid-structure interactions*, *Journal of Computational Physics* (2020) 110028.

[19] P. J. Hoogerbrugge and J. M. V. A. Koelman, *Simulating microscopic hydrodynamic phenomena with dissipative particle dynamics*, *EPL (Europhysics Letters)* **19** (1992), no. 3 155.

[20] P. Español and P. Warren, *Statistical mechanics of dissipative particle dynamics*, *EPL (Europhysics Letters)* **30** (1995), no. 4 191.

[21] J. D. Moore, B. C. Barnes, S. Izvekov, M. Lísal, M. S. Sellers, D. E. Taylor, and J. K. Brennan, *A coarse-grain force field for rdx: Density dependent and energy conserving*, *The Journal of Chemical Physics* **144** (2016), no. 10 104501, [https://doi.org/10.1063/1.4942520].

[22] A. Chaudhri and J. R. Lukes, *Multicomponent energy conserving dissipative particle dynamics: A general framework for mesoscopic heat transfer applications*, Journal of Heat Transfer **131** (Jan, 2009) 033108–033108–9.

[23] E. Abu-Nada, *Dissipative particle dynamics simulation of natural convection using variable thermal properties*, International Communications in Heat and Mass Transfer **69** (2015), no. Supplement C 84 – 93.

[24] E. O. Johansson, T. Yamada, B. Sundén, and J. Yuan, *Modeling mesoscopic solidification using dissipative particle dynamics*, International Journal of Thermal Sciences **101** (2016) 207 – 216.

[25] M. Liu, P. Meakin, and H. Huang, *Dissipative particle dynamics simulation of pore-scale multiphase fluid flow*, Water Resources Research **43** (2007), no. 4. W04411.

[26] Y. Xia, J. Goral, H. Huang, I. Miskovic, P. Meakin, and M. Deo, *Many-body dissipative particle dynamics modeling of fluid flow in fine-grained nanoporous shales*, Physics of Fluids **29** (2017), no. 5 056601, [https://doi.org/10.1063/1.4981136].

[27] G. C. Ganzenmuller, S. Hiermaier, and M. O. Steinhauser, *Shock-wave induced damage in lipid bilayers: a dissipative particle dynamics simulation study*, Soft Matter **7** (2011) 4307–4317.

[28] J. B. Maillet, E. Bourasseau, N. Desbiens, G. Vallverdu, and G. Stoltz, *Mesoscopic simulations of shock-to-detonation transition in reactive liquid high explosive*, EPL (Europhysics Letters) **96** (2011), no. 6 68007.

[29] S. Litvinov, M. Ellero, X. Hu, and N. A. Adams, *Smoothed dissipative particle dynamics model for polymer molecules in suspension*, Phys. Rev. E **77** (Jun, 2008) 066703.

[30] G. Faure, J.-B. Maillet, J. Roussel, and G. Stoltz, *Size consistency in smoothed dissipative particle dynamics*, Phys. Rev. E **94** (Oct, 2016) 043305.

[31] A. Vázquez-Quesada, M. Ellero, and P. Español, *Consistent scaling of thermal fluctuations in smoothed dissipative particle dynamics*, The Journal of Chemical Physics **130** (2009), no. 3 034901, [https://doi.org/10.1063/1.3050100].

[32] J. A. Backer, C. P. Lowe, H. C. J. Hoefsloot, and P. D. Iedema, *Combined length scales in dissipative particle dynamics*, The Journal of Chemical Physics **123** (2005), no. 11 114905, [https://doi.org/10.1063/1.2013208].

[33] R. Qiao and P. He, *Mapping of dissipative particle dynamics in fluctuating hydrodynamics simulations*, The Journal of Chemical Physics **128** (2008), no. 12 126101, [https://doi.org/10.1063/1.2897991].

[34] P. Español and M. Revenga, *Smoothed dissipative particle dynamics*, *Phys. Rev. E* **67** (Feb, 2003) 026705.

[35] S. Litvinov, M. Ellero, X. Hu, and N. A. Adams, *Self-diffusion coefficient in smoothed dissipative particle dynamics*, *The Journal of Chemical Physics* **130** (2009), no. 2 021101, [https://doi.org/10.1063/1.3058437].

[36] P. Español and P. Warren, *Perspective: Dissipative particle dynamics*, *The Journal of Chemical Physics* **146** (2017), no. 15 150901, [http://dx.doi.org/10.1063/1.4979514].

[37] Z. Li, A. Yazdani, A. Tartakovsky, and G. E. Karniadakis, *Transport dissipative particle dynamics model for mesoscopic advection-diffusion-reaction problems*, *The Journal of Chemical Physics* **143** (2015), no. 1 014101, [https://doi.org/10.1063/1.4923254].

[38] M. B. Elowitz, A. J. Levine, E. D. Siggia, and P. S. Swain, *Stochastic gene expression in a single cell*, *Science* **297** (2002), no. 5584 1183–1186.

[39] B. Drawert, S. Hellander, M. Trogdon, T.-M. Yi, and L. Petzold, *A framework for discrete stochastic simulation on 3d moving boundary domains*, *The Journal of chemical physics* **145** (2016), no. 18 184113.

[40] S. P. Banavar, C. Gomez, M. Trogdon, L. R. Petzold, T.-M. Yi, and O. Campàs, *Mechanical feedback coordinates cell wall expansion and assembly in yeast mating morphogenesis*, *PLoS computational biology* **14** (2018), no. 1 e1005940.

[41] T.-R. Teschner, L. Könözsy, and K. W. Jenkins, *Progress in particle-based multiscale and hybrid methods for flow applications*, *Microfluidics and Nanofluidics* **20** (Apr, 2016) 68.

[42] G. Karniadakis, A. Beskok, and N. Aluru, *Microflows and Nanoflows: Fundamentals and Simulation.* Interdisciplinary Applied Mathematics. Springer New York, 2005.

[43] D. Bernstein, *Simulating mesoscopic reaction-diffusion systems using the Gillespie algorithm*, *Phys. Rev. E* **71** (Apr, 2005) 041103.

[44] J. Elf and M. Ehrenberg, *Spontaneous separation of bi-stable biochemical systems into spatial domains of opposite phases*, in *Systems Biology, IEE Proceedings*, vol. 1, pp. 230–236, IET, 2004.

[45] A. B. Stundzia and C. J. Lumsden, *Stochastic simulation of coupled reaction–diffusion processes*, *Journal of computational physics* **127** (1996), no. 1 196–207.

[46] C. W. Gardiner *et. al.*, *Handbook of stochastic methods*, vol. 3. Springer Berlin, 1985.

[47] N. D. Petsev, L. G. Leal, and M. S. Shell, *Hybrid molecular-continuum simulations using smoothed dissipative particle dynamics*, *The Journal of Chemical Physics* **142** (2015), no. 4 044101, [http://dx.doi.org/10.1063/1.4905720].

[48] F. Irgens, *Continuum Mechanics.* Springer Berlin Heidelberg, 2008.

[49] J. J. Monaghan, *Smoothed particle hydrodynamics*, *Reports on Progress in Physics* **68** (2005), no. 8 1703.

[50] M. B. Liu and G. R. Liu, *Smoothed particle hydrodynamics (SPH): an overview and recent developments*, *Archives of Computational Methods in Engineering* **17** (Mar, 2010) 25–76.

[51] D. Molteni and A. Colagrossi, *A simple procedure to improve the pressure evaluation in hydrodynamic context using the SPH*, *Computer Physics Communications* **180** (2009), no. 6 861 – 872.

[52] S. Shao and E. Y. Lo, *Incompressible SPH method for simulating newtonian and non-newtonian flows with a free surface*, *Advances in Water Resources* **26** (2003), no. 7 787 – 800.

[53] S. Lind, R. Xu, P. Stansby, and B. Rogers, *Incompressible smoothed particle hydrodynamics for free-surface flows: A generalised diffusion-based algorithm for stability and validations for impulsive flows and propagating waves*, *Journal of Computational Physics* **231** (2012), no. 4 1499 – 1523.

[54] M. Ellero, M. Serrano, and P. Español, *Incompressible smoothed particle hydrodynamics*, *Journal of Computational Physics* **226** (2007), no. 2 1731 – 1752.

[55] J. J. Monaghan, *Smoothed particle hydrodynamics*, *Annual Review of Astronomy and Astrophysics* **30** (1992), no. 1 543–574, [https://doi.org/10.1146/annurev.aa.30.090192.002551].

[56] J. Monaghan and J. Kajtar, *SPH particle boundary forces for arbitrary boundaries*, *Computer Physics Communications* **180** (2009), no. 10 1811 – 1820.

[57] G. Oger, M. Doring, B. Alessandrini, and P. Ferrant, *An improved SPH method: Towards higher order convergence*, *Journal of Computational Physics* **225** (2007), no. 2 1472 – 1492.

[58] J. Monaghan, *SPH without a tensile instability*, *Journal of Computational Physics* **159** (2000), no. 2 290 – 311.

[59] N. Barkai and S. Leibler, *Biological rhythms: Circadian clocks limited by noise*, Nature **403** (2000), no. 6767 267–268.

[60] J. Paulsson, O. G. Berg, and M. Ehrenberg, *Stochastic focusing: fluctuation-enhanced sensitivity of intracellular regulation*, Proceedings of the National Academy of Sciences **97** (2000), no. 13 7148–7153.

[61] M. Thattai and A. Van Oudenaarden, *Intrinsic noise in gene regulatory networks*, Proceedings of the National Academy of Sciences **98** (2001), no. 15 8614–8619.

[62] D. T. Gillespie, *Exact stochastic simulation of coupled chemical reactions*, J. Phys. Chem. **81** (Dec., 1977) 2340–2361.

[63] A. M. Tartakovsky, P. Meakin, T. D. Scheibe, and R. M. E. West, *Simulations of reactive transport and precipitation with smoothed particle hydrodynamics*, Journal of Computational Physics **222** (2007), no. 2 654–672.

[64] B. Drawert, A. Hellander, B. Bales, D. Banerjee, G. Bellesia, B. J. Daigle, Jr., G. Douglas, M. Gu, A. Gupta, S. Hellander, C. Horuk, D. Nath, A. Takkar, S. Wu, P. Lötstedt, C. Krintz, and L. R. Petzold, *Stochastic simulation service: Bridging the gap between the computational expert and the biologist*, PLOS Computational Biology **12** (12, 2016) 1–15.

[65] S. K. Lele, *Compact finite difference schemes with spectral-like resolution*, Journal of Computational Physics **103** (1992), no. 1 16 – 42.

[66] M. Israeli and S. A. Orszag, *Approximation of radiation boundary conditions*, Journal of Computational Physics **41** (1981), no. 1 115 – 135.

[67] M. Mungal and C. Frieler, *The effects of damköhler number in a turbulent shear layer*, Combustion and Flame **71** (1988), no. 1 23 – 34.

[68] N. E. L. Haugen, J. Kruger, D. Mitra, and T. Lovas, *The effect of turbulence on mass transfer rates of small inertial particles with surface reactions*, Journal of Fluid Mechanics **836** (2018) 932–951.

[69] L. Schmidt, *The Engineering of Chemical Reactions*. Topics in chemical engineering. Oxford University Press, 1998.

[70] J. Plawsky, *Transport Phenomena Fundamentals*. Chemical Industries. Taylor & Francis, 2001.

[71] I. Tosun, *Modelling in Transport Phenomena*. Elsevier Science, 2002.

[72] R. Kee, M. Coltrin, and P. Glarborg, *Chemically Reacting Flow: Theory and Practice*. Wiley, 2005.

[73] T. Bennett, *Transport by Advection and Diffusion.* Wiley Global Education, 2012.

[74] J. P. Morris, P. J. Fox, and Y. Zhu, *Modeling low reynolds number incompressible flows using SPH*, Journal of Computational Physics **136** (1997), no. 1 214 – 226.

[75] S. Adami, X. Hu, and N. Adams, *A generalized wall boundary condition for smoothed particle hydrodynamics*, Journal of Computational Physics **231** (2012), no. 21 7057 – 7075.

[76] T. Ye, N. Phan-Thien, C. T. Lim, L. Peng, and H. Shi, *Hybrid smoothed dissipative particle dynamics and immersed boundary method for simulation of red blood cells in flows*, Phys. Rev. E **95** (Jun, 2017) 063314.

[77] A. Colagrossi and M. Landrini, *Numerical simulation of interfacial flows by smoothed particle hydrodynamics*, Journal of computational physics **191** (2003), no. 2 448–475.

[78] J. Feldman and J. Bonet, *Dynamic refinement and boundary contact forces in SPH with applications in fluid flow problems*, International Journal for Numerical Methods in Engineering **72** (2007), no. 3 295–324.

[79] F. Macia, M. Antuono, L. M. González, and A. Colagrossi, *Theoretical analysis of the no-slip boundary condition enforcement in SPH methods*, Progress of theoretical physics **125** (2011), no. 6 1091–1121.

[80] M. Ferrand, D. R. Laurence, B. D. Rogers, D. Violeau, and C. Kassiotis, *Unified semi-analytical wall boundary conditions for inviscid, laminar or turbulent flows in the meshless SPH method*, International Journal for Numerical Methods in Fluids **71** (2012), no. 4 446–472, [https://onlinelibrary.wiley.com/doi/pdf/10.1002/fld.3666].

[81] A. Colagrossi, B. Bouscasse, M. Antuono, and S. Marrone, *Particle packing algorithm for SPH schemes*, Computer Physics Communications **183** (2012), no. 8 1641–1653.

[82] M. Ferrand, D. Laurence, B. D. Rogers, D. Violeau, and C. Kassiotis, *Unified semi-analytical wall boundary conditions for inviscid, laminar or turbulent flows in the meshless SPH method*, International Journal for Numerical Methods in Fluids **71** (2013), no. 4 446–472.

[83] F. Bierbrauer, P. C. Bollada, and T. N. Phillips, *A consistent reflected image particle approach to the treatment of boundary conditions in smoothed particle hydrodynamics*, Computer Methods in Applied Mechanics and Engineering **198** (2009), no. 41-44 3400–3410.

[84] A. Amicarelli, G. Agate, and R. Guandalini, *A 3d fully lagrangian smoothed particle hydrodynamics model with both volume and surface discrete elements*, International journal for numerical methods in engineering **95** (2013), no. 5 419–450.

[85] A. Colagrossi, M. Antuono, A. Souto-Iglesias, and D. Le Touzé, *Theoretical analysis and numerical verification of the consistency of viscous smoothed-particle-hydrodynamics formulations in simulating free-surface flows*, Physical Review E **84** (2011), no. 2 026705.

[86] *Spheric-SPH grand challenges*, 2020.

[87] A. Valizadeh and J. J. Monaghan, *A study of solid wall models for weakly compressible SPH*, Journal of Computational Physics **300** (2015) 5 – 19.

[88] I. Federico, S. Marrone, A. Colagrossi, F. Aristodemo, and M. Antuono, *Simulating 2d open-channel flows through an SPH model*, European Journal of Mechanics - B/Fluids **34** (2012) 35 – 46.

[89] C. S. Peskin, *The immersed boundary method*, Acta Numerica **11** (2002) 479–517.

[90] A. Khayyer, H. Gotoh, H. Falahaty, and Y. Shimizu, *An enhanced ISPH–SPH coupled method for simulation of incompressible fluid–elastic structure interactions*, Computer Physics Communications **232** (2018) 139 – 164.

[91] L. Zhan, C. Peng, B. Zhang, and W. Wu, *A stabilized TL-WC SPH approach with GPU acceleration for three-dimensional fluid–structure interaction*, Journal of Fluids and Structures **86** (2019) 329 – 353.

[92] Z. Li, X. Bian, Y.-H. Tang, and G. E. Karniadakis, *A dissipative particle dynamics method for arbitrarily complex geometries*, Journal of Computational Physics **355** (2018) 534 – 547.

[93] R. Nestor, M. Basa, and N. Quinlan, *Moving boundary problems in the finite volume particle method*, in *3rd ERCOFTAC SPHERIC workshop on SPH applications, Switzerland, Lausanne*, 2008.

[94] M. S. Shadloo, A. Zainali, M. Yildiz, and A. Suleman, *A robust weakly compressible sph method and its comparison with an incompressible SPH*, International Journal for Numerical Methods in Engineering **89** (2012), no. 8 939–956.

[95] A. Khayyer, H. Gotoh, and Y. Shimizu, *Comparative study on accuracy and conservation properties of two particle regularization schemes and proposal of an optimized particle shifting scheme in ISPH context*, Journal of Computational Physics **332** (2017) 236–256.

[96] G. Oger, S. Marrone, D. L. Touzé, and M. de Leffe, *SPH accuracy improvement through the combination of a quasi-lagrangian shifting transport velocity and consistent ale formalisms*, Journal of Computational Physics **313** (2016) 76 – 98.

[97] C. Zhang, X. Y. Hu, and N. A. Adams, *A generalized transport-velocity formulation for smoothed particle hydrodynamics*, Journal of Computational Physics **337** (2017) 216 – 232.

[98] S. Litvinov, X. Hu, and N. Adams, *Towards consistence and convergence of conservative SPH approximations*, Journal of Computational Physics **301** (2015) 394 – 401.

[99] J. J. Monaghan and J. C. Lattanzio, *A Refined Method for Astrophysical Problems*, Astronomy and Astrophysics **149** (1985) 135–143.

[100] S.-i. Inutsuka, *Reformulation of smoothed particle hydrodynamics with Riemann solver*, Journal of Computational Physics **179** (2002), no. 1 238–267.

[101] G. Murante, S. Borgani, R. Brunino, and S.-H. Cha, *Hydrodynamic simulations with the godunov smoothed particle hydrodynamics*, Monthly Notices of the Royal Astronomical Society **417** (2011), no. 1 136–153.

[102] K. Puri and P. Ramachandran, *Approximate Riemann solvers for the Godunov SPH (GSPH)*, Journal of Computational Physics **270** (2014) 432–458.

[103] J. Gray, J. Monaghan, and R. Swift, *SPH elastic dynamics*, Computer Methods in Applied Mechanics and Engineering **190** (2001), no. 49 6641 – 6662.

[104] A. Colagrossi and M. Landrini, *Numerical simulation of interfacial flows by smoothed particle hydrodynamics*, Journal of Computational Physics **191** (2003), no. 2 448 – 475.

[105] P. Sun, A. Colagrossi, S. Marrone, M. Antuono, and A. Zhang, *Multi-resolution delta-plus-SPH with tensile instability control: Towards high reynolds number flows*, Computer Physics Communications **224** (2018) 63 – 80.

[106] D. Shepard, *A two-dimensional interpolation function for irregularly-spaced data*, in *Proceedings of the 1968 23rd ACM national conference*, pp. 517–524, ACM, 1968.

[107] E. M. Lifshitz, L. Pitaevskii, and V. Berestetskii, *Landau and lifshitz course of theoretical physics*, Statistical physics **5** (1980).

[108] M. Ferrand, D. R. Laurence, B. D. Rogers, D. Violeau, and C. Kassiotis, *Unified semi-analytical wall boundary conditions for inviscid, laminar or turbulent flows in the meshless SPH method*, International Journal for Numerical Methods in

Fluids **71** (2013), no. 4 446–472,
[https://onlinelibrary.wiley.com/doi/pdf/10.1002/fld.3666].

[109] H. Wendland, *Piecewise polynomial, positive definite and compactly supported radial functions of minimal degree*, Advances in computational Mathematics **4** (1995), no. 1 389–396.

[110] J. H. Ferziger and M. Perić, *Computational methods for fluid dynamics*, vol. 3. Springer, 2002.

[111] U. Ghia, K. Ghia, and C. Shin, *High-re solutions for incompressible flow using the navier-stokes equations and a multigrid method*, Journal of Computational Physics **48** (1982), no. 3 387 – 411.

[112] D. D. Gray and A. Giorgini, *The validity of the boussinesq approximation for liquids and gases*, International Journal of Heat and Mass Transfer **19** (1976), no. 5 545 – 551.

[113] F. Moukalled and S. Acharya, *Natural convection in the annulus between concentric horizontal circular and square cylinders*, Journal of Thermophysics and Heat Transfer **10** (Jul, 1996) 524–531.

[114] C. Shu and Y. D. Zhu, *Efficient computation of natural convection in a concentric annulus between an outer square cylinder and an inner circular cylinder*, International Journal for Numerical Methods in Fluids **38** (2002), no. 5 429–445.

[115] Y. Peng, Y. T. Chew, and C. Shu, *Numerical simulation of natural convection in a concentric annulus between a square outer cylinder and a circular inner cylinder using the taylor-series-expansion and least-squares-based lattice boltzmann method*, Phys. Rev. E **67** (Feb, 2003) 026701.

[116] D. Angeli, P. Levoni, and G. S. Barozzi, *Numerical predictions for stable buoyant regimes within a square cavity containing a heated horizontal cylinder*, International Journal of Heat and Mass Transfer **51** (2008), no. 3 553 – 565.

[117] A. K. De and A. Dalal, *A numerical study of natural convection around a square, horizontal, heated cylinder placed in an enclosure*, International Journal of Heat and Mass Transfer **49** (2006), no. 23 4608 – 4623.

[118] C. Butler, D. Newport, and M. Geron, *Natural convection experiments on a heated horizontal cylinder in a differentially heated square cavity*, Experimental Thermal and Fluid Science **44** (2013) 199 – 208.

[119] G. Cesini, M. Paroncini, G. Cortella, and M. Manzan, *Natural convection from a horizontal cylinder in a rectangular cavity*, International Journal of Heat and Mass Transfer **42** (1999), no. 10 1801 – 1811.

[120] B. Drawert, B. Jacob, Z. Li, T.-M. Yi, and L. Petzold, *Validation data for a hybrid smoothed dissipative particle dynamics (SDPD) spatial stochastic simulation algorithm (sSSA) method*, Data in Brief **22** (2019) 11 – 15.

[121] P. Van Liedekerke, P. Ghysels, E. Tijskens, G. Samaey, B. Smeedts, D. Roose, and H. Ramon, *A particle-based model to simulate the micromechanics of single-plant parenchyma cells and aggregates*, Physical biology **7** (2010), no. 2 026006.

[122] P. Van Liedekerke, E. Tijskens, H. Ramon, P. Ghysels, G. Samaey, and D. Roose, *Particle-based model to simulate the micromechanics of biological cells*, Physical Review E **81** (2010), no. 6 061906.

[123] C. G. Alvaro and J. Thorner, *Heterotrimeric G Protein-coupled Receptor Signaling in Yeast Mating Pheromone Response*, The Journal of Biological Chemistry **291** (Apr., 2016) 7788–7795.

[124] D. E. Levin, *Regulation of cell wall biogenesis in Saccharomyces cerevisiae: the cell wall integrity signaling pathway*, Genetics **189** (Dec., 2011) 1145–1175.

[125] S. P. Banavar, C. Gomez, M. Trogdon, L. R. Petzold, T.-M. Yi, and O. Campàs, *Mechanical feedback coordinates cell wall expansion and assembly in yeast mating morphogenesis*, PLoS computational biology **14** (2018), no. 1 e1005940.

[126] T. I. Moore, H. Tanaka, H. J. Kim, N. L. Jeon, and T.-M. Yi, *Yeast G-proteins mediate directional sensing and polarization behaviors in response to changes in pheromone gradient direction*, Molecular Biology of the Cell **24** (Feb., 2013) 521–534.

[127] A. W. McClure, M. Minakova, J. M. Dyer, T. R. Zyla, T. C. Elston, and D. J. Lew, *Role of Polarized G Protein Signaling in Tracking Pheromone Gradients*, Developmental Cell **35** (Nov., 2015) 471–482.

[128] B. Errede, L. Vered, E. Ford, M. I. Pena, and T. C. Elston, *Pheromone-induced morphogenesis and gradient tracking are dependent on the MAPK Fus3 binding to Gα*, Molecular Biology of the Cell **26** (Sept., 2015) 3343–3358.

[129] M. Renardy, T.-M. Yi, D. Xiu, and C.-S. Chou, *Parameter uncertainty quantification using surrogate models applied to a spatial model of yeast mating polarization*, PLoS computational biology **14** (2018), no. 5 e1006181.

[130] M. Trogdon, B. Drawert, C. Gomez, S. P. Banavar, T.-M. Yi, O. Campàs, and L. R. Petzold, *The effect of cell geometry on polarization in budding yeast*, PLoS Computational Biology **14** (June, 2018).

[131] M. J. Lawson, B. Drawert, M. Khammash, L. Petzold, and T.-M. Yi, *Spatial Stochastic Dynamics Enable Robust Cell Polarization*, PLoS Computational Biology **9** (July, 2013).

[132] E. Barnhart, K.-C. Lee, G. M. Allen, J. A. Theriot, and A. Mogilner, *Balance between cell-substrate adhesion and myosin contraction determines the frequency of motility initiation in fish keratocytes*, Proceedings of the National Academy of Sciences **112** (2015), no. 16 5045–5050, [https://www.pnas.org/content/112/16/5045.full.pdf].

[133] J. Hu, S. Jafari, Y. Han, A. J. Grodzinsky, S. Cai, and M. Guo, *Size- and speed-dependent mechanical behavior in living mammalian cytoplasm*, Proceedings of the National Academy of Sciences **114** (2017), no. 36 9529–9534, [https://www.pnas.org/content/114/36/9529.full.pdf].

[134] R. M. Barfield, J. C. Fromme, and R. Schekman, *The exomer coat complex transports Fus1p to the plasma membrane via a novel plasma membrane sorting signal in yeast*, Molecular Biology of the Cell **20** (Dec., 2009) 4985–4996.

[135] L. Fu and Z. Ji, *An optimal particle setup method with Centroidal Voronoi Particle dynamics*, Computer Physics Communications **234** (2019) 72–92.

[136] S. Rosswog, *Boosting the accuracy of SPH techniques: Newtonian and special-relativistic tests*, Monthly Notices of the Royal Astronomical Society **448** (2015), no. 4 3628–3664.

[137] P. Mocz and S. Succi, *Numerical solution of the nonlinear schrödinger equation using smoothed-particle hydrodynamics*, Phys. Rev. E **91** (May, 2015) 053304.

[138] A. Hellander, M. J. Lawson, B. Drawert, and L. Petzold, *Local error estimates for adaptive simulation of the reaction–diffusion master equation via operator splitting*, Journal of computational physics **266** (2014) 89–100.

[139] T. Jahnke and C. Lubich, *Error bounds for exponential operator splittings*, BIT Numerical Mathematics **40** (2000), no. 4 735–744.

[140] S. Plimpton, *Fast parallel algorithms for short-range molecular dynamics*, Journal of Computational Physics **117** (1995), no. 1 1 – 19.

[141] A. Nasar, B. D. Rogers, A. Revell, and P. Stansby, *Flexible slender body fluid interaction: vector-based discrete element method with Eulerian smoothed particle hydrodynamics*, Computers & Fluids **179** (2019) 563–578.

[142] A. Nasar, B. D. Rogers, A. Revell, P. Stansby, and S. Lind, *Eulerian weakly compressible smoothed particle hydrodynamics (sph) with the immersed boundary method for thin slender bodies*, Journal of Fluids and Structures **84** (2019) 263–282.